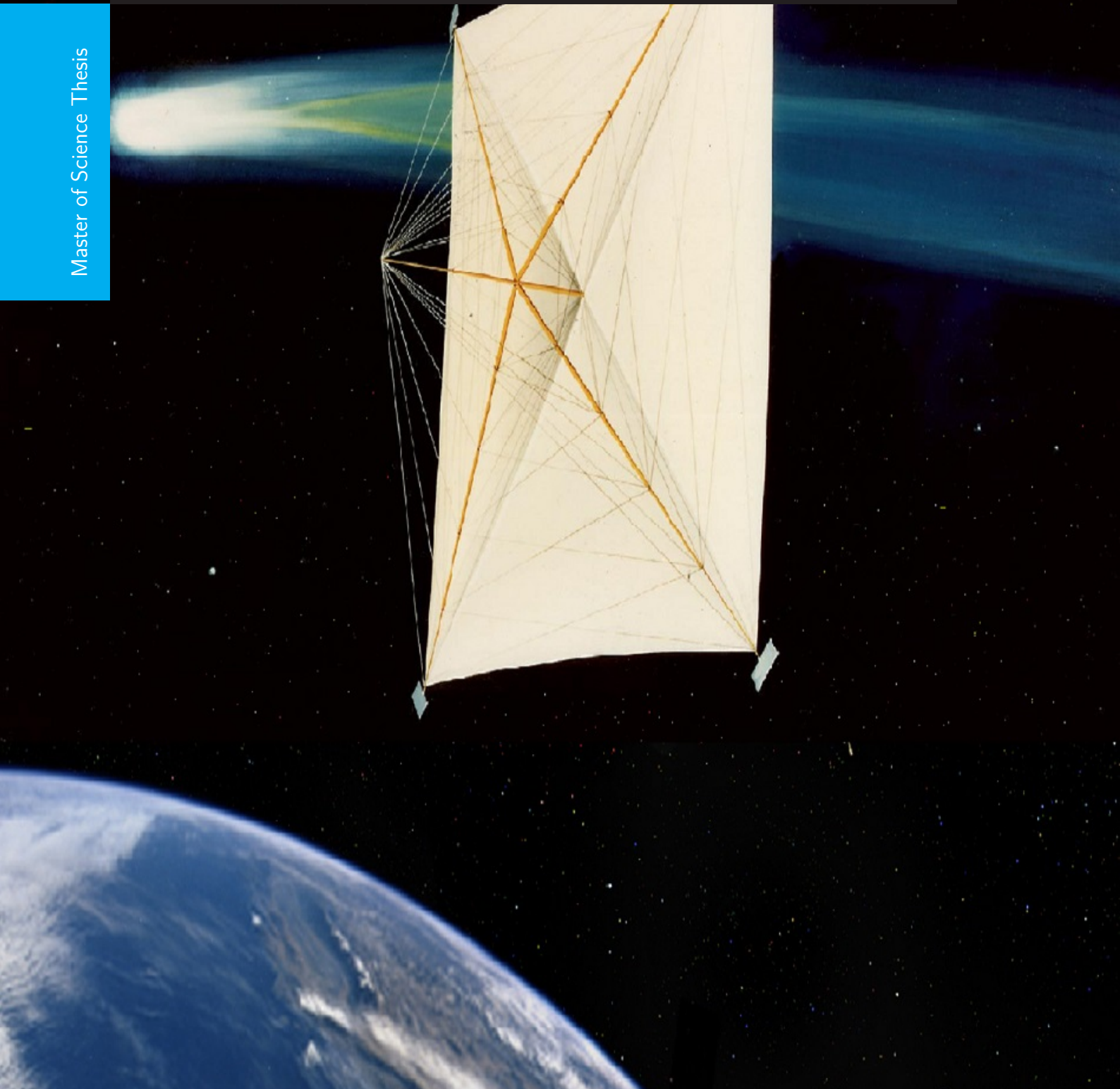


Optimization of Solar Sailcraft Trajectory for a Comet Sample Return Mission

Ananthakrishnan Krishnan

Master of Science Thesis



OPTIMIZATION OF SOLAR SAILCRAFT TRAJECTORY FOR A COMET SAMPLE RETURN MISSION

by

Ananthkrishnan Krishnan

in partial fulfillment of the requirements for the degree of

Master of Science
in Aerospace Engineering

at the Delft University of Technology,
to be defended publicly on Monday December 17, 2018 at 9:00 AM.

Student number:	4518934	
Thesis committee:	Prof. Dr. E. Schrama,	Chairholder
	Prof. Ir. R. Noomen,	Supervisor
	Prof. Ir. B. T. C. Zandbergen,	External

This thesis is confidential and cannot be made public until June 16, 2019.

An electronic version of this thesis is available at <http://repository.tudelft.nl/>.

ACKNOWLEDGEMENTS

Writing this report marks almost the end of my Masters in Aerospace Engineering at TU Delft. My masters journey, which started as a passion for space exploration, has been a thoroughly exciting and challenging experience, and to reach this point would not have been possible without all the wonderful people who supported me during this period.

First of all, I would like to thank my supervisor Prof. Ron Noomen, for giving me the opportunity to work with him on this topic. I am really grateful for his help, guidance and support throughout the thesis, which were instrumental for completing it. I would also like to thank him for all the discussions and conversations during the countless weekly meetings, which kept me motivated during the course of the thesis.

I would like to express my gratitude to Dr. Dominic Dirx for his help and support with the development of the solar sail model in Tudat. His timely guidance were crucial for solving the coding related issues that occurred during the thesis. I am also thankful for the invaluable help and suggestions given by Dr. Jeannette Heiligers during the critical phases of my thesis.

My time at Delft would not have been complete without my friends. I thank all my friends for sharing all the amazing and wonderful moments during these three years, the memories of which I will remember forever. In addition to the fun times, I thank them for helping me through the challenging phases of my masters as well.

Lastly and most importantly, I am forever grateful to my parents, who are my source of motivation and strength. I would like to thank them for their unconditional love, constant belief, continuous support and encouragement during this period.

*Ananthkrishnan Krishnan
Delft, December 2018*

ABSTRACT

Comets, the sporadic visitors from the outer edges of the Solar System, are considered to hold the key for understanding the formation of planets and the origin of life on Earth. Having spent the majority of time away from the radiative environment of the inner Solar System, the chemistry of the comets has remained unaltered, making them the pristine samples of the matter from the ancient Solar nebula. A mission to bring cometary particles back to Earth enables the examination of the materials in well equipped laboratories and saves the mass of the instruments to be carried on board. To this end, a comet sample return mission has been a priority in the Solar System exploration plans of space agencies. However, due to the highly inclined and highly eccentric nature of comets' orbits, it is challenging to reach them. As conventional propulsion methods require a large quantity of propellant for this type of mission, the feasibility of using the novel propulsion technique of solar sailing is explored in this thesis. The solar sailcraft is propelled by the reflection of the incident solar radiation on a large, lightweight sail. In order to return the comet samples to Earth within a reasonable time period, the orbit transfer is considered as an optimal control problem with constraints placed on the sailcraft's position and velocity.

The comet 103P/Hartley 2 was selected as the target for the mission and the total mission (to the comet and back to Earth) is aimed to be completed within the ten year period between 2020-2030. A perfectly reflecting (ideal) square sail with a lightness number β of 0.05 (moderate performance) was considered for the analysis. The sailcraft was to depart from a heliocentric Earth orbit and the sail orientation was considered to change at a fixed number of nodal points along the trajectory. The Differential Evolution (DE) algorithm was used to search for time-optimal trajectories that minimize the approach distance to the comet and the relative velocity with respect to the comet during sample collection. Grid Search method was used to narrow in on the optimal departure date and time-of-flight based on the optimization result. The optimal trajectory obtained predicts the solar sailcraft to reach the comet, collect the samples and return back to Earth in 6.77 years. The time of arrival at the comet was found to match with the comet's perihelion passage, enabling effective sample collection. The outcome of the trajectory analysis, thus successfully demonstrates the applicability of solar sailing to comet sample return missions in the near future.

CONTENTS

Abstract	v
List of Abbreviations	ix
List of Symbols	xii
1 Introduction	1
2 Background	5
2.1 Heritage of Solar Sailing	5
2.2 Missions to Comets	8
2.3 Mission Objectives	12
2.4 Mission Target	13
3 Theory	15
3.1 Reference Frames	15
3.1.1 Heliocentric Reference Frame	16
3.1.2 Spacecraft orbital reference frame	16
3.1.3 Reference Frame Transformation	17
3.2 Coordinate Systems	18
3.2.1 Cartesian Coordinates	18
3.2.2 Keplerian Elements	19
3.2.3 Modified Equinoctial Elements	19
3.3 Dynamics Model	20
3.4 Perturbations	20
3.5 Solar Sailing	22
3.5.1 Performance metrics	22
3.5.2 Ideal Sail Force Model	23
3.5.3 Optical Sail Force Model	25
3.5.4 Choice of SRP Force Model	26
3.6 Equations of motion	27
3.6.1 Vector Form	27
3.6.2 Gauss' form of Lagrange's Planetary Equations	27
4 Numerical Tools	29
4.1 Integrator	29
4.2 Integrator Choice	31
4.3 Optimization	31
4.3.1 LTOM and GTOM	33
4.3.2 Choice of Optimization Method	34
4.4 Differential Evolution	35
4.5 Grid Search	37

5	Validation and Parameter Tuning	39
5.1	SRP Acceleration Model Validation	39
5.2	Sailcraft Dynamics Validation	40
5.3	Integrator Tuning.	42
5.4	Integrator validation	45
5.5	DE Tuning.	46
5.5.1	Objective function	47
5.5.2	Node Vs Population Size	48
5.5.3	F and CR combination	49
5.6	DE Validation	50
6	Results	53
6.1	Outbound Trajectory to 103P/Hartley 2	53
6.2	Sample Return Trajectory to 103P/Hartley 2	58
7	Conclusions and Recommendations	63
7.1	Conclusions.	63
7.2	Recommendations	64
A	Optimization of three-dimensional solar sailcraft trajectory	67
B	Trajectory to 103P/Hartley 2 using a High Performance Sail	69
C	Two-dimensional Grid Search Results for the Outbound Trajectory	71
	Bibliography	73

LIST OF ABBREVIATIONS

AU	Astronomical Unit
CCRSR	Comet Coma Rendezvous Sample Return
CPU	Central Processing Unit
CSSR	Comet Surface Sample Return Mission
DE	Differential Evolution
DLR	Deutsches Zentrum für Luft- und Raumfahrt
EA	Evolutionary Algorithm
ESA	European Space Agency
GA	Genetic Algorithm
GNC	Guidance, Navigation and Control
GTOM	Global Trajectory Optimization Method
HIF	Heliocentric Inertial Frame
IKAROS	Interplanetary Kite-craft Accelerated by Radiation of the Sun
JAXA	Japan Aerospace Exploration Agency
JPL	Jet Propulsion Laboratory
LPE	Lagrange Planetary Equations
LTOM	Local Trajectory Optimization Method
MEE	Modified Equinoctial Elements
NAIF	Navigation and Ancillary Information Facility
NASA	National Aeronautics and Space Administration
NEA	Near-Earth Asteroid
NLP	Nonlinear Programming
PAGMO	Parallel Global Multiobjective Optimizer
PSO	Particle Swarm Optimization
RK	Runge-Kutta
RK87DP	Variable Step-size Runge-Kutta 8(7) Dormand-Prince method
SA	Simulated Annealing
SOF	Spacecraft Orbital Reference Frame
SQP	Sequential Quadratic Programming
SRP	Solar Radiation Pressure
SSB	Solar System Barycenter
TOF	Time-of-Flight
TPBVP	Two-Point Boundary Value Problem
Tudat	TU Delft Astrodynamics Toolbox

LIST OF SYMBOLS

LATIN SYMBOLS

a	Semi-major axis	[m]
a_c	Characteristic Acceleration	[mm/m ²]
A	Sail Surface Area	[m ²]
B_f, B_b	Front and back Lambertian coefficients	[-]
c	Speed of light	[m/s]
CR	DE Crossover factor	[-]
D	Number of parameters in the decision vector	[-]
e	Eccentricity	[-]
E	Eccentric anomaly	[deg]
F, F_i, F_r	Force acting on an ideal sail	[N]
f_R, f_S, f_W	Components of perturbing SRP acceleration	[ms ⁻²]
F	DE Weight factor	[-]
G	Universal Gravitational Constant	[m ³ kg ⁻¹ s ⁻²]
h	Integration time step	[s]
i	Inclination	[deg]
J	Objective Function	[-]
L_s	Solar Luminosity	[W]
m	Mass	[kg]
M	Mean anomaly	[deg]
n	Orbital Mean Motion	[s ⁻¹]
\hat{n}	Sail normal vector	[-]
\hat{n}_{HIF}	Sail Normal in HIF	[-]
\hat{n}_{SOF}	Sail Normal in SOF	[-]
NP	Population size	[-]
p, f, g, h, k, L	Modified Equinoctial Elements	[-]
p_w	Solar Wind Pressure	[N/m ²]
P	Solar Radiation Pressure	[N/m ²]
$P_{x,g}$	Population of vectors	[-]
q	Perihelion Distance	[m]
Q	Apohelion Distance	[m]
r	Radial distance	[m]
\vec{r}	Position vector	[m]
r_p, r_{sail}	Position of perturbing body and sailcraft	[m]
R	Perturbing potential	[J/kg]
R	Frame Transformation Matrix	[-]
R_E	Sun-Earth Distance	[m]
$\hat{r}, \hat{d}, \hat{h}$	Sailcraft Body Centered Reference Axes	[-]
t_p	Time of Perihelion passage	[s]

t_0	Time of departure	[s]
v	Velocity	[m/s]
$v_{i,g}, u_{i,g}$	Mutation and Trial vector	[-]
v_w	Solar Wind Speed	[m/s]
v_∞	Hyperbolic excess velocity	[m/s]
W	Energy flux from Sun	[W/m ²]
$x_{i,g}$	Target vector	[-]
x_i, x_{i+1}	Sailcraft state at given timestep	[-]
X, Y, Z	Cartesian Coordinate Axes	[-]
x, y, z	Cartesian Coordinates	[m]

GREEK SYMBOLS

α	Sail Cone Angle	[deg]
β	Sail Lightness Number	[-]
δ	Sail Clock Angle	[deg]
Δ	Finite Difference or Increment	[-]
η	Sail efficiency	[-]
λ	Centerline Angle	[-]
μ	Standard Gravitational Parameter	[m ³ s ⁻²]
$\tilde{\mu}$	Effective gravitational parameter	[m ³ s ⁻²]
ν	True anomaly	[deg]
σ	Sail loading	[g/m ²]
σ_{SA}	Sail assembly loading	[g/m ²]
τ	Time interval between nodes	[s]
ω	Argument of Perigee	[deg]
Ω	Right Ascension of the Ascending Node	[deg]

1

INTRODUCTION

For centuries, we as mankind have been interested in understanding our origin and answering the fundamental question about the formation of life on Earth. In this quest to understand the early Solar System formation, a key attribute is about determining the physical and chemical properties of the primordial mixture, which contained the building blocks for planets and other bodies in the Solar System. The problem in deducing the composition of this mixture is that over the last 4.5 billion years since their formation, the planets and their moons have undergone further processing [1]. As a consequence of changes inflicted by high speed impacts between the bodies and due to gravitational compression and internal heating, the surface composition of these bodies have evolved over time and thus, do not offer much insight about early Solar System.

However, some of the other bodies like comets and asteroids, which are considered to have been formed earlier than the planets, have remained essentially unchanged since their accretion [2]. Comets, especially, orbiting near the outer edges of the Solar System - far from the heat and radiation of the Sun, have remained almost unaltered. Only occasionally, few of the comets pass through the inner Solar System pulled by gravity, which is witnessed on Earth as the flashy trails across the night sky. Due to their long orbital periods and minimal interaction with Sun, the chemistry of the comets has been preserved over time. Thus, comets are considered as the pristine examples of matter formed from the ancient Solar nebula.

Studying and investigating cometary material could provide information about the primordial mixture from which the planets formed. Such an investigation will also shed some light on cometary nuclei, exploring the chemistry and physics behind the comet's activity. Our current knowledge on comets has been gained through a combination of surface observations and missions to comets. The presence of ice, ammonia and more importantly, organic compounds like methane and the amino acid glycine in comets have been confirmed by the past missions to these bodies [3]. These findings strengthen the theory that water and life on Earth might have been seeded by comets impacting the newly formed Earth. Hence, exploring comets can help in improving our understanding of planet formation and the origin of life on Earth.

To this end, a science mission to study these bodies is imperative. Though the past flyby or orbiter missions to comets have provided crucial observations regarding the comet's physical and chemical characteristics, the scientific benefits of bringing samples of cometary material back to Earth are far superior. A sample return mission would provide an unique perspective by enabling the examination of the material returned from the comet in well equipped laboratories [4]. Using the plethora of instruments and measuring techniques available on ground, higher levels of precision

can be obtained and the methods can be updated as the technology evolves. This is in contrast to orbiter/lander missions taking in-situ measurements at the comet, which are limited by the number and capability of instruments carried on board the spacecraft. While for a sample return mission, the only specialized equipment needed on board is a simple sample collection and storage device. Additionally, the results inferred from analyzing the returned samples could enhance the value of orbiter/lander observations by validating their findings [4].

The scientific implications of comet sample return missions have made them a prime candidate in Solar System exploration roadmaps of space agencies [5]. Thus, it is essential to analyze the prospect of performing such a mission in the near future. The orbits of comets are, however, challenging to reach due to their high inclination and high eccentricity. Missions to these high energy orbits require a huge amount of ΔV . For conventional propulsion methods which traditionally operate by converting the chemical energy stored in molecules to kinetic energy, this translates to carrying large quantities of propellant on board the spacecraft. As an example, the Rosetta mission (which is just a one-way mission) to comet 67P/Churyumov-Gerasimenko required close to 60% of the orbiter mass as propellant to deliver a payload of 265 kg [6]. This is a major limitation in employing conventional propulsion techniques for comet sample return missions.

To overcome this limitation, novel propulsion technique known as solar sailing, is considered for the comet sample return mission in this research. In solar sailing, a large, lightweight sail is used for reflecting the incident radiation from the Sun. The unique advantage of solar sailing is that by using the Sun as the energy source, it does not require propellants as conventional propulsion methods. It is based on the principle of momentum transferred during the impact of a stream of photons (travelling at speed of light) onto the sail and thus, the sailcraft [7]. Though, the propulsive force resulting from the momentum transfer to the sail is in the order of few mN, in the frictionless environment of space, this constant energy input can build up to significant proportions over time, enabling the sailcraft to reach great distances in the Solar System. Thus, solar sailing has been considered over the years to possess the potential for interplanetary orbit transfers.

The main issues to consider in applying solar sailing is that, firstly, the thrust magnitude decreases as the square of the distance from the Sun. Secondly, unlike other low thrust propulsion systems, the direction of thrust cannot take up any arbitrary vector alignment and is limited by the orientation of the sail. Further since the acceleration attained from solar sailing is very small, the time-of-flight (including the return leg) becomes crucial in accomplishing the mission as well as to prevent the degradation of the sail and other components. In view of the above factors, the trajectory of the solar sailcraft needs to be optimized to complete the sample return mission within a reasonable time period. Therefore, the research presented in this thesis report will focus on studying the dynamical aspects of the solar sailcraft trajectory to (and back from) the comet. The comet sample return mission will be considered as a time-optimal problem with orbital constraints and the optimal trajectory will be determined by employing an optimization algorithm (differential evolution). The outcome of the research will aim to provide more insight into dynamics of the problem, assess the results based on current sailcraft performance level and ultimately, answer the following research question:

Is it possible to effectively return cometary samples back to Earth using solar sailing within a reasonable time frame?

In order to address the above question, the report begins with the background information on past missions and moves onto discuss mission critical details like target selection and orbital require-

ments in Chapter 2. This is followed by Chapter 3, which lays the theoretical foundation of work done in this thesis, by presenting the choices made regarding the dynamics model used in the simulation. To determine the optimal trajectory, a number of numerical tools were utilized. Chapter 4 explains the choice of the tools and describes their operation, while Chapter 5 elaborates the process of tuning the parameters of these tools and validating their settings. The results of optimization of the solar sailcraft trajectory for a comet sample return mission are provided in Chapter 6. Finally, the conclusions derived from this thesis work, along with the recommendations for future research are presented in Chapter 7.

2

BACKGROUND

The current chapter is used to provide the necessary background to the research topic dealt in this thesis report. The chapter begins with the history of solar sailing and proceeds to present its advancement over the years. The various solar sailing missions attempted over the years are briefly described, along with the breakthrough mission - IKAROS. The presentation of this heritage will provide the current level of solar sail performance.

A description of the past missions to comets is provided in Section 2.2. The information gained from these missions was used to decide critical design aspects of the sample return mission. Based on the design considerations, the mission objectives and the trajectory requirements were derived and mentioned in Section 2.3. Finally, the possible targets for the comet sample return mission are listed in Section 2.4 and the choice of the target is also explained.

2.1. HERITAGE OF SOLAR SAILING

Solar sailing is a novel idea of utilizing the naturally available radiation from the Sun for spacecraft propulsion. The propulsive force, in case of solar sailing, is obtained through the momentum gained from the impact of photons on the sail. Though the force resulting from the momentum exchange is small, the sailcraft is slowly and continuously accelerated, making solar sailing a form of very-low-thrust propulsion.

The concept of solar sailing as a practical means of spacecraft propulsion was conceived as early as 1924 by the German engineer Fridrickh Tsander [7]. Following this, there were brief studies in the 1950s discussing the advantages of using solar sailing for interplanetary travel. But it was not until 1976 when solar sailing was formally considered for a rendezvous mission to comet Halley by the National Aeronautics and Space Administration (NASA).

The initial proposal consisted of a 800 x 800 m three-axis stabilized square solar sail [7]. However, the design was changed to a heliogyro (rotating) configuration with twelve 7.5 km long blades, owing to the high risk associated with the deployment of the large square sail. Following the preliminary concept analysis phase, the competing concept of Solar Electric Propulsion (SEP) was selected by NASA upon its merit of having lower risks for the mission. Ultimately, due to the rising cost estimate, the comet rendezvous mission was dropped. The analysis and design developments achieved during this period sparked the interest in manufacturing and testing key technologies related to solar sailing for future projects.



Figure 2.1: Solar Sail deployment test on ground at DLR [9].

In 1999, the Deutsches Zentrum für Luft- und Raumfahrt (DLR) in a joint effort with the European Space Agency (ESA) successfully tested the first full-scale deployment of a solar sail on ground at their centre in Cologne. A picture of the deployed sail is given in Figure 2.1. The 20x20 m sail consisted of four segments made of Kapton having a thickness of $7.5 \mu\text{m}$, and the sail segments were deployed with the help of ultra-light weight carbon fiber reinforced plastic (CFRP) booms [8].

Apart from national space agencies, solar sailing also attracted interest from organizations like the Planetary Society and Cosmos Studios, to set up a private project to test suborbital prototypes. In 2005, the Cosmos 1 sailcraft (outcome of the collaborative project) marked the first attempt in demonstrating the solar sail technology on orbit. The 600 m^2 sail was made of $5 \mu\text{m}$ thick aluminised reinforced mylar [10]. But due to the malfunctioning of the Volna launcher, the sailcraft was lost in an explosion just 82 seconds after launch.

Following the above attempts on testing solar sailing technology, the first spacecraft to successfully demonstrate solar sailing as the main propulsion system in interplanetary space was the Interplanetary Kite-craft Accelerated by Radiation Of the Sun (IKAROS), developed by the Japan Aerospace Exploration Agency (JAXA). The spacecraft comprised of a $14 \times 14 \text{ m}$ square sail with a thickness of $7.5 \mu\text{m}$ [11]. The sail was made of thermoplastic polyimide and had 0.5 kg tip masses at the corners for stability. Further, thin-film solar cells were embedded on the sail, generating a power of 300 W and the blocks of LCD (Liquid Crystal Display) panels attached along the edges were used to control the sail attitude.

IKAROS was launched aboard the H-IIA rocket from Tanegashima Space Center on 21 May 2010 [11]. With the sail successfully deployed in June 2010, the sailcraft was set on an interplanetary trajectory to Venus. Figure 2.2 shows the picture of IKAROS taken using a Deployable Camera (DCAM) after sail deployment. During the course of the sailcraft's trajectory, thrust (and the resulting acceleration) due to SRP and the performance of sail's attitude control system were measured. IKAROS

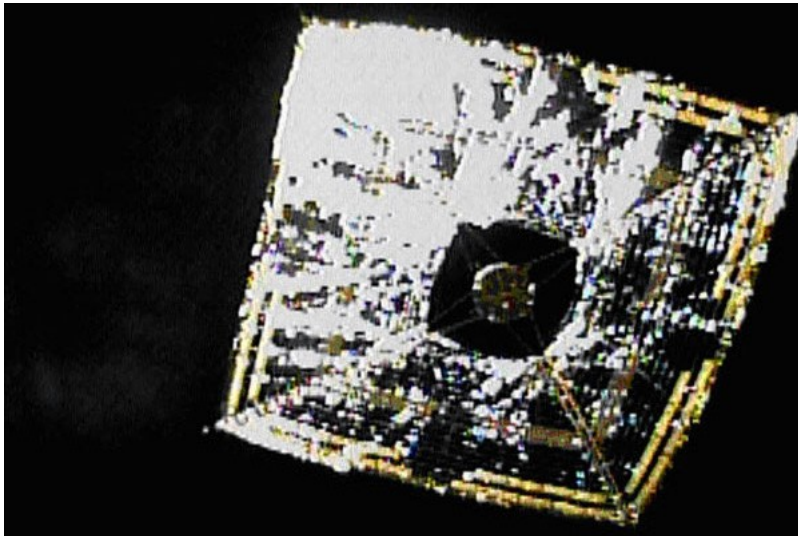


Figure 2.2: IKAROS in interplanetary space after sail deployment [12].

accomplished its primary goals of deploying the sail, measuring acceleration (and velocity) gained from SRP and controlling the orientation of the sail. In addition, IKAROS also completed its scientific objectives of detecting and measuring gamma-ray bursts and cosmic dust. Thus, IKAROS proved to be a landmark in the advancement of solar sail technology and a precursor for making solar sailing a promising option for space exploration.

With the success of IKAROS, the utilization of solar sailing in space missions increased and expanded to a multitude of applications. NASA's NanoSail-D2 sailcraft (launched in November 2010) [13], following a successful sail deployment, remained in the Low Earth Orbit (LEO) for 240 days and produced large amounts of data on the use of solar sails as passive ways of de-orbiting space debris and dead satellites. NASA had also planned a solar sailing demonstrator mission called Sunjammer in 2013 to test sail deployment and sail attitude control, while guiding the sailcraft to the Earth-Sun L1 Lagrange point. The sail was made of Kapton, having a surface area of 1200 m², making it the largest solar sail built till date [14]. With a large surface area and a thickness of just 5 μm, the sail was capable of producing thrust in the order of 10⁻² N. In spite of Sunjammer being cancelled before its launch, the design and deployment tests (on ground) were valuable for the research on manufacture and control of large solar sails.

The Planetary Society after their attempt in 2005 with Cosmos 1, re-initiated their plans with the LightSail series of sailcraft. The new design was based on NanoSail-D, consisting of a 32 m² Mylar sail stacked in a 3U CubeSat format [15]. LightSail-1 was launched as a test mission in May 2015 and was declared a success following the sail deployment on 7 June 2015. The main mission, LightSail-2, is scheduled for launch in 2019 and will aim to demonstrate controlled raising of orbit apogee using solar sail as main propulsion.

In view of the results achieved and progress made in solar sailing technology, more missions have been planned for the forthcoming future. Among the recently proposed missions is the ESA/DLR collaborative project - Gossamer Roadmap - which would send series of demonstrator sailcraft called Gossamer-1,-2 and -3 to space [16]. The objective of the project is to demonstrate the deployment and full attitude and orbit control of 5x5 m, 10x10 m and 50x50 m sails, that can be used to deorbit small satellites from LEO. Another important mission is NASA's Near Earth Asteroid (NEA) Scout mission, which will demonstrate the ability of low-cost sailcraft to perform NEAs reconnais-

sance. The sailcraft will be in a 6U cubesat formation, weighing just 12 kg and propelled by a 83 m² sail [17]. Notably, NEA Scout will be one of several payloads aboard the maiden flight of NASA's Space Launch System (SLS), scheduled to be launched in 2019.

Finally, OKEANOS (Outsized Kite-craft for Exploration and Astronautics in the Outer Solar System) is a proposed solar sail mission by JAXA to Jupiter's Trojan asteroids [18]. The spacecraft will be propelled by a hybrid solar sail, containing thin solar panels embedded on the sail to power an ion engine. As a supplementary part of the mission, lander and sample return options are considered and if selected, the mission will be launched in late 2020s.

From the time when solar sailing was considered a concept for novels, it has made giant strides in becoming a reality, through the efforts of scientists and engineers over the years. Especially in the last decade, missions like IKAROS and NanoSail-D2 have demonstrated the capabilities and the wide range of applications that the technology possesses, some of which are unique to solar sailing. The current research focuses on further reducing the mass per unit area of the sail (called the sail loading parameter), to enable ambitious mission concepts to outer Solar System or to place satellites in non-Keplerian orbits. Additionally, performing further flight tests on sail deployment and attitude control would make the technology more robust and reliable. Therefore, with the rising opportunities for solar sailing and future advancements in place, solar sailing has the potential to become a viable option for space exploration.

2.2. MISSIONS TO COMETS

Comets are small bodies made of ice and dust, and are known to originate from the outer regions of the Solar System. The core of the comets called the nucleus consists of a combination of dust, rock, ice and frozen oxides of carbon [20]. Due to the heat from solar radiation, the ice and frozen oxides sublime from the nucleus forming a thin atmosphere called the coma. The presence of these gases and ions in the coma is responsible for the comet's brightness, which lead to the detection of numerous comets. During the comet's passage close to the Sun, the force exerted by solar wind on the coma creates a plasma tail pointing away from the Sun. The sublimation of ice from the nucleus drags along the dust particles as the gases release from the surface, forming an additional dust tail (shaped by solar radiation pressure) as depicted in Figure 2.3. These tails can be generally observed



Figure 2.3: Depiction of the plasma (blue) and dust (white) tails of a comet [19].

to extend to great lengths (in the order of 10^7 km) from the comet, but the density of particles reduces rapidly with the distance from the comet.

The comets, along with the planets and asteroids, are considered to have been formed from the collapse of a dense, molecular cloud made of dust, gas and ice [21]. However, the planets have all been subjected to significant reprocessing since their formation and do not provide much information about the material from which they formed. Whereas, comets having spent only a small fraction of their orbital period in the inner Solar System, remain pristine, free from reprocessing of their material or structure. The comets are also considered to be of high astrobiological value due to the possibility that comets might have contributed to the presence of life and volatile compounds found on Earth [22]. Thus, observing and exploring comets has been one of the important priorities for the space agencies around the world, to further the understanding of the solar System.

In the past, there have been space missions to study the comets at a close range, including flyby, rendezvous, orbiter or sample return missions. Amongst the previous missions to comets, Deep Impact, Rosetta and Stardust were unique and their observations were pivotal for the current knowledge about these bodies. In the Deep Impact mission, NASA released an impactor into the comet, to study the interior composition of the comet 9P/Tempel by observing the collision. The spacecraft was launched on a Delta-II rocket from Cape Canaveral on January 12, 2005 [23]. Following the 60 days cruise phase, the spacecraft began its approach towards the comet, while also observing the comet's position, activity, rotation and dust environment. The 372 kg impactor was detached from the flyby spacecraft on June 29, 2005 and was positioned in front of the comet for an impact on July 4, 2005.

The Deep Impact spacecraft took images of the event and its outcome from a safe distance of about 500 km from the comet. The crater formed due to the impact was measured to be around 150 m in diameter and 30 m in depth [24]. The image analysis of the impact revealed that the material ejected consisted of more dust particles (finer than sand) and fewer ice than presumed. More detailed information could not be recognized from the images due to the bright dust cloud over the crater. Another mission named Stardust was used as a follow-up to obtain better images of the crater. The data from these missions indicated the presence of materials containing carbon as well as water ice on the comet 9P/Tempel 1 [24]. Based on the results, Tempel 1 was envisaged to have originated in the Uranus and Neptune Oort Cloud region of the Solar System. The Deep Impact mission was extended to observe other comets including 103P/Hartley 2, before ending the mission in September 2013. The observations made at the Hartley 2 revealed a crucial detail that the comet was made of dry ice and not water ice as anticipated earlier.

ESA's Rosetta mission features as an important milestone in the study of comets and for demonstrating the technological advancement achieved in the field of space exploration. The objective of the mission was to orbit comet 67P/Churyumov Gerasimenko and conduct an extensive investigation of the comet [6]. Towards this aim, the spacecraft was designed to consist of two parts, viz., an orbiter and a lander (Philae). The orbiter was used to observe the comet's activities and the lander was employed to make in-situ measurements of its composition. On March 2, 2004, the spacecraft was launched on an Ariane 5 rocket from the Guiana Space Centre [6]. The main propulsion system of the spacecraft consisted of 24 paired bipropellant (monomethylhydrazine-dinitrogen tetroxide) 10 N thrusters, which were used for orbit maneuvers and attitude control. Rosetta's trajectory to the comet included gravity assist maneuvers and flybys, with the first Earth flyby on March 4, 2005 [26]. To correct its trajectory, the spacecraft made a low-altitude flyby of Mars in February 2007, which was followed by two more Earth flybys in November 2007 and November 2009 respectively. After

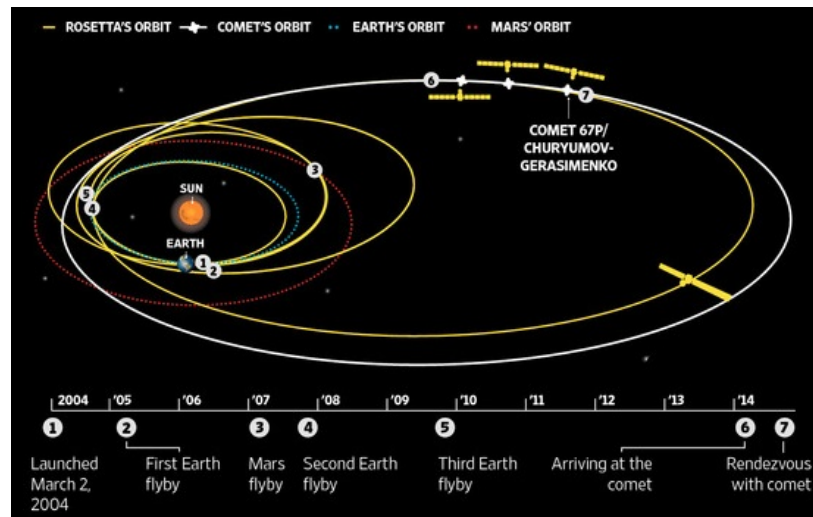


Figure 2.4: Illustration of the trajectory followed by Rosetta to Comet 67P/Churyumov-Gerashimenko [25].

ten years long journey, Rosetta entered into the orbit around the comet on August 6, 2014, after performing a series of rendezvous maneuvers.

Immediately after getting into the orbit around the comet, the orbiter surveyed the comet's surface for potential sites for deploying the lander. On November 12, 2014, the Philae lander detached from the orbiter and landed on the comet [26]. After a brief hiatus, the lander completed most of planned measurements and transmitted the obtained data back to Earth via the orbiter. Due to the decrease in sunlight received by the spacecraft as the comet travelled through the outer Solar System and as the communication with the orbiter/lander did not look optimistic, the mission was concluded by guiding the orbiter to the comet's surface. Being a recent mission, interpretation of data sent by the spacecraft are still ongoing. From the initial analysis, the isotopic signature of water vapour on the comet was found to be different to that on Earth [28]. The measurements made by Philae indicate the presence of carbon and hydrogen molecules in the coma. Further, the material displaced at Philae's landing site revealed traces of organic compounds, few of which were observed for the first time on a comet.

Till date, Stardust is the first and only mission to have achieved the feat of bringing back samples from the coma of a comet back to Earth. In 1995, NASA set up Stardust as a dedicated mission to

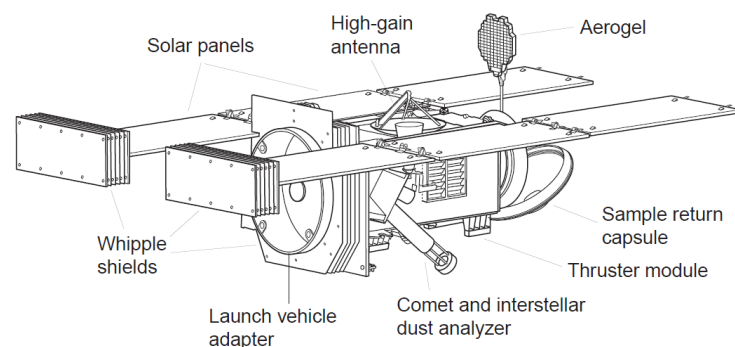


Figure 2.5: Illustration of the Stardust spacecraft [27].

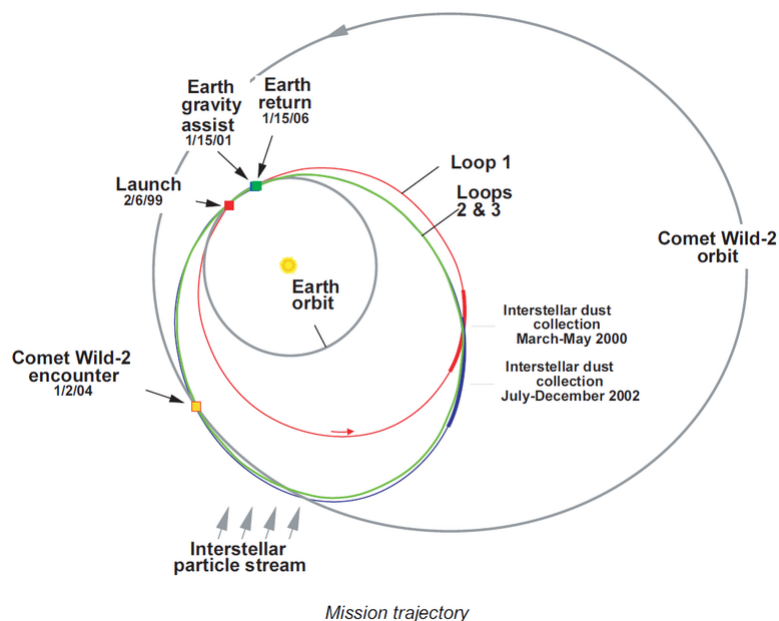


Figure 2.6: Stardust mission trajectory [27].

study Comet Wild 2, a long-period comet believed to hold pristine samples of materials from its formation. The spacecraft was launched aboard a Delta-II rocket from Cape Canaveral on February 7, 1999 [29]. The main objective of the mission was to make a non-destructive capture of particles from the comet's coma and return the samples safely back to Earth. The spacecraft followed a heliocentric orbit (Figure 2.6) that took it around the Sun and approached the Earth for a gravity assist maneuver in 2001. After around 5 years en route to the comet, Stardust performs a close flyby at a distance of 240 km to the comet, with the sample collector deployed to collect particles.

To prevent damage during particle collection, the sample collector was designed in the shape of a tennis racket as shown in Figure 2.5, containing blocks of ultra-low density aerogel in silicon-based porous structures [29]. Five other scientific payloads (Imaging Camera, Dust Flux Monitor, Dust Analyzer, Sample Collection Instrument and Telecommunication Unit) were carried on-board to capture images of the comet and perform real-time analysis to determine the composition, mass and size of the collected dust particles. On January 15, 2006 after around two years on its return trajectory, Stardust reached Earth and released the Sample Return Capsule, which re-entered the Earth's atmosphere and landed safely in the Utah desert.

The comet's samples were examined in the clean room at NASA's Johnson Space Center in Houston. More than a million microscopic dust particles were embedded in the aerogel, along with few particles in the size range of 0.1 mm [30]. The preliminary analysis of the samples indicated the presence of a large number of organic compounds, with some of the compounds containing biologically usable nitrogen. The existence of iron and copper sulfide in the samples suggested the heating of comet's core during the early Solar System, since the formation of these molecules require the presence of water [31]. Additionally, for the first time, glycine (an amino acid) was detected in the particles ejected from Wild 2, supporting the theory that life in the Universe could be common and not rare.

2.3. MISSION OBJECTIVES

The current knowledge on comets is based on the information gained from optical remote sensing, computer simulations, study of meteoritic materials found on Earth, flyby missions to comets and examination of samples returned from Comet Wild 2 [21]. The space missions, especially, were crucial for expanding our understanding of the comets as well as for verifying some of the existing theories on comets. The samples retrieved by Stardust spacecraft appears to be composed of a heterogeneous mixture of organics and minerals. Intermingled in these mixtures, a collection of highly refractory and highly volatile components were also found. Few of these components show clear isotopic evidence of pre-solar materials [21]. Thus, the study on cometary samples has successfully shown that comets possess materials originating from a wide range of environments, making them a repository of primordial Solar System materials.

Although the samples brought back by Stardust were vital in arriving at the above insights, the particle collection had its drawback as well. The particles from comet Wild 2's coma was collected in the aerogel collector at a relative velocity of around 6.1 km/s with respect to the comet [21]. Due to this high impact velocity, only some of the particles survived unaltered, while others were either altered or destroyed. This in turn affects the interpretation of particle characteristics and determination of their elemental composition, as there is a possibility for some components to be selectively altered or lost over others. Hence, these samples do not yet provide answers to some of the key questions regarding - (i) the presence of volatile organics and nebular condensate amorphous silicates, (ii) relative concentration of minerals/organics, and (iii) the radiometric chronology of comets and the early Solar System [21].

Based on the lessons learnt from the Stardust mission, certain points for improved results were suggested in the concept study on Comet Coma Rendezvous Sample Return mission (CCRSR) [21]. Primarily, as the Stardust spacecraft returned with less than 1000 particles with size greater than 15 μm , it would be beneficial for statistical analysis if close to hundred times more particles were collected by flying closer to the comet and/or allowing longer collection times. Such an increase in the sample size of particles collected will enhance the chance of identifying the particle types, finding particular organic molecules, collecting rare minerals and establishing the isotopic chronologies of the materials. It was also suggested that the particles should be collected using high-purity metallic meshes, in order to avoid organic contaminants, extraneous materials and the ubiquitous components (Si and O) of the aerogel.

Secondly, the study also recommended that the samples need to be collected at relative velocities less than 0.1 km/s, so that the particles do not suffer any alteration during collection, thus yielding unbiased, pristine samples of the cometary material [21]. Apart from the constraints placed on sample collection, the overall time period of the mission - from launch till return of samples to Earth - needs to be set. The mission duration is one of the driving factors which influences the reliability requirements of various spacecraft subsystems. Obviously, the longer is the mission, the more reliable, withstanding and long lasting should be components, which is extremely challenging due to the harsh environment in space. In a comet sample return concept study by NASA [32], a maximum time limit of 10 years was set for the overall mission duration considering the safety of the samples as well during the transit. Further, since in this thesis, solar sailing will be used as the main propulsion, the degradation of the sail material from constant exposure to solar radiation should be considered as well when deciding the mission duration. In this regard, the study on Near-Earth Asteroid (NEA) sample return using solar sailcraft [33] also employed a 10 year time period for maximum mission duration. Due to the similar nature of the missions in the above mentioned concept studies and the

one considered in this thesis, the total mission duration was constrained to be within 10 years.

Based on the discussion on past missions and sample return mission concept studies, the following scientific outcomes are expected as a result of the solar sailcraft comet sample return mission:

- To determine the relative concentrations of minerals and organics.
- To establish a radiometric chronology for comets.
- To check for materials of interstellar origin (like amorphous silicate condensate).
- To understand the nature of evolution and extinction of cometary ice.
- To check for the presence of simple biomolecules.

To achieve the above objectives, certain requirements are placed on the sailcraft trajectory for the mission considered in this thesis. These are:

- The sailcraft shall collect samples from the comet's coma at a distance less than 250 km.
- Sample collection shall take place at a relative velocity of less than 0.1 km/s with respect to the comet.
- The overall mission duration shall be less than 10 years.
- For effective sample collection, the sailcraft shall collect the samples during the comet's perihelion passage.

2.4. MISSION TARGET

Comets have been observed by mankind for many centuries but it was not until 1759 that a comet's orbital characteristics were studied and catalogued. This was done for the first time for the comet 1P/Halley. Following that, numerous comets have been identified and added to the catalogue. Presently, over 5882 comets have been identified, with around 3958 comets having an official designation [34].

Given such an extensive list of comets, it is challenging to narrow it down to a comet as the target for our comet sample return mission. Hence, few selection criteria were established to filter through the number of comets suitable for the mission. Possible mission targets are short-listed based on the scientific interest to study the comet, and the practical viability of reaching the comet and returning samples to Earth. Since, solar sailing trajectory evolves slowly, the target's perihelion distance is desired to be within 0.5 AU from the Earth's orbit and considering the overall mission duration, the target comet's orbit shall be close to the ecliptic plane. The list of criteria used to filter the potential targets for the mission are:

- Comets perihelion distance (q) should be close to Earth's orbit (≤ 0.5 AU).
- Comets' orbit should be prograde and close to the ecliptic plane ($i < 20^\circ$)
- Comets next perihelion passage must occur within 2020 and 2030, to have a realistic launch window.
- Comets whose basic physical characteristics like size, mass and shape have already been studied are preferred, to minimize the mission risk.

The final condition on the list is to prevent designing a mission to a target whose physical and orbital parameters are not yet known accurately due to very few observational sitings. However, at the same time, comets that have been studied extensively in the past like the Halley's comet are also not preferred for the mission, in order to avoid redundancy and explore new frontiers.

Based on NASA's list of priority comet targets of high scientific importance [35] and targets short-listed in the concept study for the Comet Surface Sample Return (CSSR) mission [32], a list of potential targets was obtained as shown in Table 2.1. The data on the comet's orbit were taken from JPL's Small Bodies Database [34].

Table 2.1: Potential targets for comet sample return mission using a solar sailcraft (data obtained from [34]).

Comet	e	q (AU)	i (deg)	ω (deg)	Ω (deg)	Q (AU)	Period (yrs)	Classification
2P/Encke	0.8483	0.3360	11.7801	186.5420	334.5686	4.0942	3.30	NEO
6P/d'Arrest	0.6114	1.3615	19.4810	178.1152	138.9337	5.6459	6.56	Jupiter-family
8P/Tuttle	0.8198	1.0271	54.9832	207.5092	270.3417	10.3726	13.61	Jupiter-family (NEO)
9P/Tempel 1	0.5175	1.5066	10.5305	178.8771	68.9334	4.7383	5.52	Jupiter-family
15P/Finlay	0.7205	0.9746	6.8036	347.5656	347.5656	13.8006	6.51	Jupiter-family (NEO)
19P/Borrelly	0.6232	1.3598	30.3130	353.3507	75.4359	5.8595	6.86	Jupiter-family
21P/Giacobini-Zinner	0.7068	1.0307	31.9081	172.5844	195.3970	6.0004	6.59	Jupiter-family (NEO)
41P/Tuttle-Giacobini-Kresák	0.6612	1.0450	9.2293	62.1566	141.0677	5.1248	5.42	Jupiter-family (NEO)
55P/Tempel-Tuttle	0.9055	0.9764	162.4865	172.5003	235.2701	19.7002	33.24	Halley-type (NEO)
67P/Churyumov-Gerasimenko	0.6406	1.2453	7.0437	12.6944	50.1800	5.6842	6.45	Jupiter-family
79P/du Toit-Hartley	0.6185	1.1238	3.1456	281.6893	280.6403	4.7679	5.06	Jupiter-family (NEO)
81P/Wild 2	0.5370	1.5979	3.2372	41.7596	136.0977	5.3060	6.41	Jupiter-family
103P/Hartley 2	0.6938	1.0642	13.6043	181.3223	219.7487	5.8863	6.48	Jupiter-family (NEO)

Out of the 13 potential targets, four comets (8P, 19P, 21P and 55P) have inclination greater than the specified criterion of 20° and another four comets (2P, 9P, 6P and 81P) do not have their perihelion distance close to the Earth's orbit. Among the remaining comets, only comets 67P and 103P have been visited by spacecraft previously. However, comet 67P/Churyumov-Gerasimenko was the target of the recently concluded Rosetta mission, during which the comet was studied in detail using a combination of orbiter and lander. Whereas, comet 103P/Hartley 2 was briefly observed by the Deep Impact spacecraft as part of its extended mission. Using the data from Deep Impact mission, the comet's physical properties were determined. But, being a flyby mission, the comet was not studied comprehensively, making it an ideal target for a sample return mission. A follow-up sample return mission could (i) provide better insight about the comet's composition, (ii) confirm the existing observational data, and (iii) obtain chronological information regarding its origin and evolution. Therefore, the comet 103P/Hartley 2 was selected as the target for the comet sample return mission using a solar sailcraft.

3

THEORY

This chapter lays the foundation of the theoretical concepts used in this thesis for simulating the sailcraft trajectory. First, the basic astrodynamics concepts of reference frames and coordinate systems are introduced. This is followed by a discussion on the forces and dynamics model considered to describe the motion of the solar sailcraft. In Section 3.5, the principles and dynamics of solar sailing are explained, along with the sail design parameters. Finally, the equations of motion representing the sailcraft's trajectory are presented in Section 3.6.

3.1. REFERENCE FRAMES

In astrodynamics, to describe/simulate the motion of a spacecraft, it is vital to know (at least) the position and mass of the celestial bodies involved. As position and velocity are relative quantities, they are defined with respect to a reference system. The reference system completely describes the formation of a celestial coordinate system, in terms of origin and orientation of fundamental planes and axes [36]. Using a reference system, any point in space can be specified by a unique set of coordinates.

From Newtonian mechanics, two classes of reference frames can be defined [36]. Reference frames which are at rest or moving at constant velocity in a straight line are considered as *inertial reference frames*. Whereas, non-inertial reference frames are either in a rotational or accelerated motion. Newton's laws of motion are valid only in inertial reference frames, while apparent (or pseudo) forces have to be included when applying Newtonian mechanics in non-inertial reference frames.

There are applications that demand motion to be described about a rotating or accelerating body. For example, specifying the location of a launch site on the surface of Earth or the orientation of an instrument with respect to the satellite. In such cases, non-inertial reference frames are considered along with their associated pseudo forces like centrifugal, Coriolis or Euler forces [36]. Therefore, with the help of the above force models, a transformation matrix can be defined to convert between inertial and non-inertial frames.

As no additional force terms are required in inertial reference frames, the mathematical complexity of equations describing the motion of a body are significantly reduced. Hence, these frames are preferred for representing the motion of spacecraft, in orbit around a body or on a transfer trajectory to a target. In this section, the reference frames which were used in this thesis work, to describe the orbital dynamics and to model the sail force, are discussed.

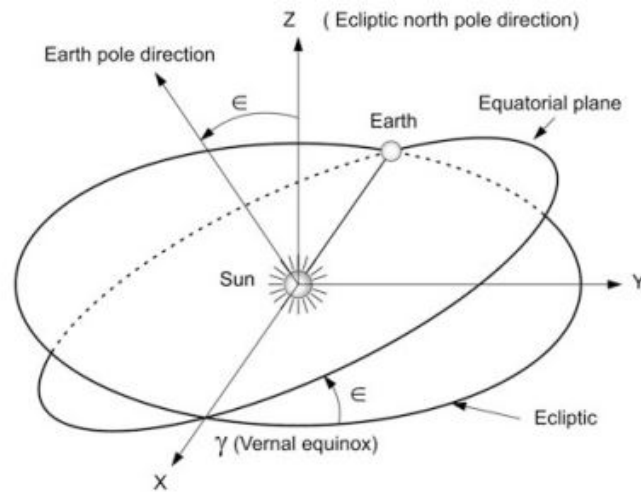


Figure 3.1: Heliocentric Reference Frame [37].

3.1.1. HELIOCENTRIC REFERENCE FRAME

Heliocentric reference frames are centered at the Sun or at the barycenter (center of mass) of the Solar System. As the bodies in the Solar System revolve around the Sun, these frames are commonly used for describing interplanetary trajectories. Although the Sun itself is orbiting the center of the Milky Way galaxy, considering the time scale of the rotation and the influence of Sun's gravitational field within the Solar System, the origin of the heliocentric reference frame can be considered to be fixed.

The fundamental plane of the heliocentric reference frame is taken to be Earth's orbital plane (ecliptic) around the Sun, since the orbits of other planets have small inclinations with respect to the ecliptic. The +Z-axis of this frame is along the ecliptic north pole direction, with the +X-axis lying in the ecliptic plane and pointing towards the Vernal equinox (the First point of Aries) [37]. The +Y-axis completes the right-handed system as given in Figure 3.1. Due to the effect of precession and nutation, the direction of the Vernal equinox shifts slowly over the centuries with respect to extragalactic sources like quasars [36]. Therefore, in order to define the reference axes direction, the orientation of the heliocentric ecliptic reference frame on 1 January 2000 at 12:00 terrestrial time is typically taken as the reference. The resulting heliocentric ecliptic inertial frame of reference is referred as *ECLIPJ2000*.

The ECLIPJ2000 frame is widely used in many astrodynamics tools and software due to its temporal reference and compatibility. Furthermore, the Solar System ephemeris information system (called SPICE), maintained by the Navigation and Ancillary Information Facility (NAIF) under NASA's Planetary Science division, is available in the ECLIPJ2000 frame [38]. This means the ephemeris data from SPICE can be directly used in the astrodynamics tool (Tudat) for trajectory simulation. The ECLIPJ2000 reference frame will thus be the fundamental reference frame for simulating the trajectory of the solar sailcraft in this thesis work, due to its inertial, space-fixed nature and availability of ephemeris data with respect to this frame.

3.1.2. SPACECRAFT ORBITAL REFERENCE FRAME

A spacecraft orbital reference frame has its origin at the center of mass (CM) of the spacecraft. It is used for describing the relative dynamical motion of various systems or components of a spacecraft

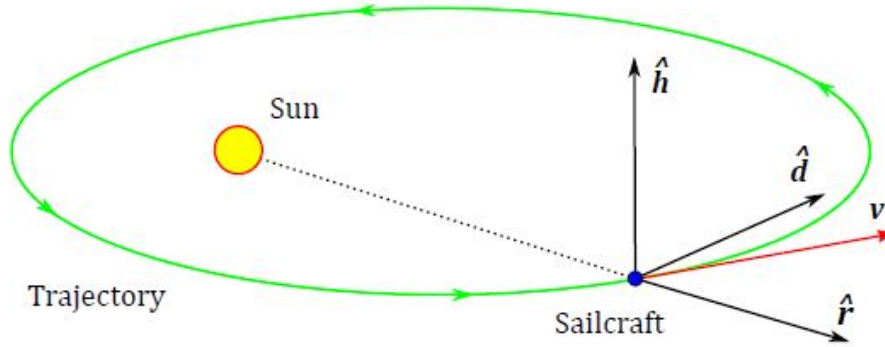


Figure 3.2: Spacecraft orbital reference frame [39].

like solar arrays, antennas or - in case of sailcraft - the sail itself. In solar sailing, the sail orientation determines both the direction and magnitude of the thrust force resulting from the SRP acting on the sail. The definition of the spacecraft reference frame thus plays an important role in expressing the orientation of the sail.

The axes of the frame are defined based on three unit vectors as shown in Figure 3.2. The radial unit vector \hat{r} points in the direction of the Sun-sail line, unit vector \hat{h} points along the sailcraft's orbital angular momentum vector and finally, the transversal unit vector \hat{d} completes the right-handed reference frame [39]. The velocity vector (v) of the sailcraft, therefore, lies in the plane formed by unit vectors \hat{r} and \hat{d} .

As the frame is centered at the CM of the spacecraft, it rotates as the spacecraft moves in its orbit around the Sun. Thus, the frame is non-inertial and if equations of motion were to be solved in this frame apparent forces should be included. To avoid this complication, the sail orientation is transformed from the spacecraft reference frame to the heliocentric reference frame and the equations are solved in the heliocentric frame.

3.1.3. REFERENCE FRAME TRANSFORMATION

From the previous subsections, it can be seen that two reference frames are to be used to describe the motion of the sailcraft. The ECLIPJ2000 frame is utilized for specifying the position and velocity of the sailcraft with respect to the Solar System barycenter (SSB). While the spacecraft orbital reference frame (SOF) is used for representing the sail attitude and calculating the acceleration due to SRP. Therefore, the sail normal vector in SOF needs to be transferred to the ECLIPJ2000 for force calculation and trajectory propagation, at every integration timestep.

The sail normal vector in SOF (\vec{n}_{SOF}) is defined as

$$\vec{n}_{SOF} = \begin{bmatrix} \cos \alpha \\ \sin \alpha \sin \delta \\ \sin \alpha \cos \delta \end{bmatrix} \quad (3.1)$$

where α and δ are the cone and clock angles respectively that unequivocally define the sail attitude in SOF. The cone angle α is defined as the angle between the sail normal vector (\hat{n}) and Sun-sail line (\hat{r}) in radial direction [7]. Whereas the clock angle δ is measured between the transverse unit vector (\hat{d}) and the projection of \hat{n} on the plane perpendicular to the Sun-sail line as depicted in Figure 3.3.

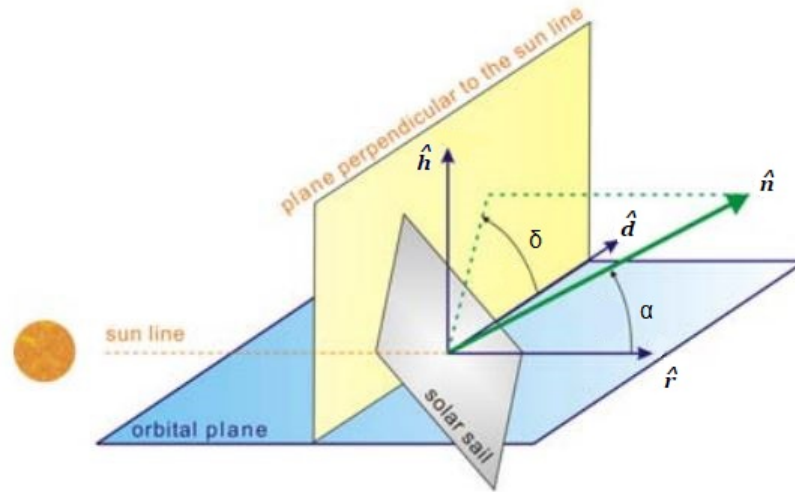


Figure 3.3: Representation of sail cone and clock angles (modified from [40]).

The unit vectors of the three axes of SOF are given by [41]

$$\hat{r} = \frac{\vec{r}}{|\vec{r}|}, \quad \hat{h} = \frac{\vec{r} \times \vec{v}}{|\vec{r} \times \vec{v}|}, \quad \hat{d} = \hat{r} \times \hat{h} \quad (3.2)$$

where \vec{r} and \vec{v} are the position and velocity vectors of the sailcraft respectively. The frame transformation matrix R from SOF to ECLIPJ2000 is [41]:

$$R = (\hat{r} \quad \hat{d} \quad \hat{h}) \quad (3.3)$$

Thus, the sail normal vector in the heliocentric inertial frame is

$$\hat{n}_{HIF} = R \hat{n}_{SOF} \quad (3.4)$$

3.2. COORDINATE SYSTEMS

A coordinate system provides the method for locating a point within the reference frame. The coordinate systems thus play an essential role in expressing the position, velocity or the complete state of celestial bodies and spacecraft along their trajectory. The coordinate systems used to characterize the solar sail trajectories in this thesis work are discussed in this section. Finally, the choice of the coordinate system which was employed to write the equations of motion is also explained in Section 3.2.3.

3.2.1. CARTESIAN COORDINATES

The Cartesian coordinate system is one of the most commonly used coordinate systems in the fields of mathematics, science and engineering. The position of a point is specified by three spatial coordinates (x, y, z) which represent the signed distance of its projection on the three frame axes from the frame origin O . The state of a body in Cartesian coordinates $(x, y, z, \dot{x}, \dot{y}, \dot{z})$ is represented as a combination of position and velocity components [36].

3.2.2. KEPLERIAN ELEMENTS

The set of six Keplerian orbital elements $(a, e, i, \Omega, \omega, \nu)$, in addition to specifying the position of a body, provides information about the dimension, shape and orientation of its orbit. The elements describe the orbit in terms of the conic section traced by the body. The semi-major axis a , which is the average of pericenter and apocenter distances, gives indication about the dimension of the orbits [36]. Eccentricity e describes the shape of the orbit in relation to a circle (circle: $e = 0$; ellipse: $e < 1$; parabola: $e = 1$; hyperbola: $e > 1$). The angular orientation of the orbit with respect to the reference plane is given by inclination angle i . The angular distance of the point (ascending node), where the body crosses the reference plane during its ascending path, from the reference direction is represented by the Right Ascension of the Ascending Node Ω ; in heliocentric problems, this is called the Longitude of the Ascending Node. The argument of periapsis ω provides the orientation of the orbit in the orbital plane of the body, by an angle measured from the ascending node to the pericenter. The final orbital element completes the set by pinpointing the angular position of the body in the orbit.

Different options are available for representing the final element. One of which is true anomaly ν - the angle swept by the body from the pericenter [36]. A mathematically more convenient option is to use the Mean Anomaly M as it varies linearly with time - mean motion n times $(t - \tau)$ where t is current time and τ is the time of last pericenter passage. Another option is the Eccentric anomaly E which is the angle subtended at the center of the ellipse by the projection of the body on a circle circumscribing the ellipse. These anomalies can be converted between them at a given epoch and are used depending on the application. Finally, the six Keplerian elements can be converted into Cartesian coordinates (position and velocity) and vice versa.

3.2.3. MODIFIED EQUINOCTIAL ELEMENTS

The coordinate systems discussed in the above subsections carry their merits and demerits. Cartesian coordinates are simple and straightforward to implement but demand high computational time for trajectory propagation. Also, the Cartesian coordinates provide limited insight into the actual trajectory behaviour. Whereas with Keplerian elements, the characteristics of orbits are more clearly represented and trajectory propagation is quicker as well. The orbit representation using these elements is also simplified in cases without any perturbations, as five (a six, depending on choice of the anomaly) of the Keplerian elements remain constant. However, due to the nature of their definition singularities tend to occur for zero eccentricity and 0° inclination orbits. In order to overcome these drawbacks, non-singular orbital elements (equinoctial elements) were introduced and modified over the years. In this thesis work, the set of Modified Equinoctial Elements (MEE) - $[p, f, g, L, h, k]$ - introduced by Walker et al. [42] were used. The definition of the elements in terms of classical Keplerian elements is provided in Equation 3.5.

$$p = a(1 - e^2) \quad (3.5a)$$

$$f = e \cos(\Omega + \omega) \quad (3.5b)$$

$$g = e \sin(\Omega + \omega) \quad (3.5c)$$

$$h = \tan\left(\frac{i}{2}\right) \cos(\Omega) \quad (3.5d)$$

$$k = \tan\left(\frac{i}{2}\right) \sin(\Omega) \quad (3.5e)$$

$$L = M + \Omega + \omega \quad (3.5f)$$

Based on the conclusions drawn from a comparative study of coordinate systems in [43], the performance of MEE's in trajectory propagation was observed to closely follow the direct numerical integration using Cartesian coordinates. Additionally, with the benefit of having lower computation time and no singularity issues, MEE's were opted for formulating the equations of motion of the sailcraft. Other coordinate systems are utilized for their respective advantages whenever required in this thesis work.

3.3. DYNAMICS MODEL

With the basic astrodynamics framework (reference frames and coordinate systems) set, it is important to discuss the dynamics model and forces acting on the sailcraft before moving on to the equations of motion. Different dynamics models for a two-body, three-body to n-body problem formulation (with increasing complexity) can be adopted to describe the motion of the sailcraft. The choice is made based on the mission and the number of bodies whose gravitational attraction influences the sailcraft's motion significantly.

For the comet sample return mission, complex formulations like three-body problem or higher can be neglected, since the mass of the bodies involved (mass of Hartley 2 $\approx 10^{12}$ kg; mass of Earth $\approx 6 \times 10^{24}$ kg) are multiple orders lower than that of the Sun (mass of Sun $\approx 2 \times 10^{30}$ kg). Additionally, the sailcraft throughout its transfer trajectory lies outside of the Sphere of Influence (SOI) of both the bodies. In this case, the only predominant gravitational force acting on the sailcraft is due to the Sun. Therefore, a perturbed two-body problem formulation, with the Sun as the primary body and forces from other bodies (if significant) as perturbations, was considered for trajectory simulation.

In the perturbed two-body system, consisting of a sailcraft and the Sun, the motion of the sailcraft can be represented as [36]:

$$\frac{d^2 \vec{r}}{dt^2} + \frac{\mu_s}{r^3} \vec{r} = \nabla R \quad (3.6)$$

where $\mu_s = GM_{sun}$ is the gravitational parameter of the Sun and R is the perturbing potential due to all the perturbing forces acting on the sailcraft. For the situation in which $R = 0$, the solution of this equation is a Kepler orbit (conic section) for the sailcraft. However, such an ideal two-body system is extremely rare to occur. Although the gravitational force from other bodies are weaker compared to the primary body, these forces do perturb the orbit of the sailcraft, causing a deviation from the Keplerian conic sections. Thus, the perturbations are included in the equations of motion and the assessment of various perturbing forces acting on the sailcraft is carried out in the next section.

3.4. PERTURBATIONS

The main perturbing forces affecting a sailcraft in a heliocentric trajectory are the third-body gravitational forces of bodies besides the Sun and solar radiation pressure. Other perturbations like atmospheric drag and non-spherical gravitational potential of celestial bodies can be neglected, since the sailcraft moves through the vacuum of space without making close approaches to the celestial bodies within their SOI.

In order to evaluate which among the above listed perturbations have to be considered in the equations of motion, it is essential to compare the accelerations in terms of their magnitude while acting on the sailcraft. From orbital mechanics, the third-body gravitational perturbation due to the celestial bodies p acting on the sailcraft with respect to an inertial reference frame centered at SSB is:

$$a_p = \mu_p \left(\frac{\vec{r}_p - \vec{r}_{sail}}{\|\vec{r}_p - \vec{r}_{sail}\|^3} - \frac{\vec{r}_p}{\|\vec{r}_p\|^3} \right) \quad (3.7)$$

where μ_p is the gravitational parameter of the perturbing body, \vec{r}_p and \vec{r}_{sail} are the position vectors of the perturbing body and the sailcraft respectively.

Using Equation 3.7, the acceleration experienced by the sailcraft due to other celestial bodies can be estimated. These accelerations become significant for missions approaching the perturbing body within its SOI, like rendezvous or flyby missions. In this thesis work, a sample return trajectory to comet Hartley 2 will be analyzed. The starting point for this trajectory would be considered just outside the SOI of Earth and inserted into the interplanetary trajectory at 0 km/s hyperbolic excess velocity. On return to Earth, the trajectory is considered only until the point of closest approach outside of its SOI. Hence, the maximum perturbing acceleration due to Earth was calculated near its SOI. Whereas for other celestial bodies, since the sailcraft moves outside their SOI and considering the fact that comet's perihelion distance is 1.05 AU, the perturbing accelerations were estimated for a sailcraft positioned at a distance between 0.8-1.2 AU. The orders of magnitude of the third-body perturbing accelerations are listed in Table 3.1, along with the acceleration due to SRP and Sun's gravity at 1 AU for comparison.

Table 3.1: Orders of magnitude of the perturbing accelerations acting on the sailcraft.

Perturbation	Acceleration (m/s ²)
Two body - Sun	10 ⁻³
Solar Radiation Pressure	10 ⁻⁴
Third body - Venus	10 ⁻⁶
Third body - Earth	10 ⁻⁴ to 10 ⁻⁶
Third body - Mars	10 ⁻⁹
Third body - Jupiter	10 ⁻⁷
Third body - Saturn	10 ⁻⁹
Third body - Uranus	10 ⁻¹¹
Comet (103P/Hartley 2)	10 ⁻¹⁰

From Table 3.1, it is clear that the perturbations caused by other planets - Venus, Mars, Jupiter, Saturn and Uranus - are negligible compared to the acceleration due to solar gravity and SRP. In case of Earth, the acceleration magnitude resembles that of SRP very close to its SOI. But, since the sailcraft spends relatively a fleeting moment near Earth, it does not suffice to include the third-body perturbations due to Earth at the expense of increased complexity and higher computation time. Therefore, none of the perturbations due to the planets alter the sailcraft's motion considerably and hence were neglected for the simulation.

Another possible perturbation can be caused by the prevalent solar wind in the Solar System. Pressure is exerted on the solar sail due to the momentum carried by solar wind protons. The solar wind pressure P_w can be mathematically represented as [7]

$$P_w = m_p \rho v_w^2 \quad (3.8)$$

with m_p being the mass of a proton, ρ the mean proton number density and v_w the solar wind speed. The variation in solar activity affects the proton number density and wind velocity. Consid-

ering periods of high solar activity, the wind velocity can be as high as 700 km/s at 1 AU, with mean proton number density of $4 \times 10^6 \text{ m}^{-3}$ [7]. This results in a solar wind pressure of $3 \times 10^{-9} \text{ N/m}^2$, which is negligible compared to the SRP (equal to $9.12 \times 10^{-6} \text{ N/m}^2$) on the sail at 1 AU. Hence, owing to the weak and unpredictable nature of solar wind pressure, it was not considered among the perturbations for trajectory propagation in this thesis work.

In Table 3.1, the acceleration due to the comet has also been mentioned. This was calculated at close distances (250-1000 km) to the comet. Since the acceleration due to SRP is 4 to 5 orders of magnitude higher than the gravitational pull from the comet, the sailcraft can potentially hover at artificial equilibrium points [40] near the comet by adjusting the sail orientation and can closely tag the comet in its orbit. This is a feature unique to solar sailing but analyzing such orbits is beyond the scope of this thesis.

The most important perturbing force which alters the sailcraft trajectory is the solar radiation pressure. The energy continuously imparted by the solar photons on the sail produces the thrust to propel the sailcraft. Thus, the SRP which essentially provides the thrust force is modelled as the only perturbing force and included on the right-hand side of Equation 3.6. A detailed discourse on sail performance parameters and solar sailing force models is covered in the subsequent sections.

3.5. SOLAR SAILING

Solar sailing works on the principle of momentum imparted by the solar photons on the highly reflective sail film facing the Sun. The impact of photons on the sail causes the solar radiation pressure P on the sail surface area A [7],

$$P = \frac{W}{c} = \frac{L_s}{4\pi r^2 c} \quad (3.9)$$

where c is the speed of light (299,792,458 m/s) and W is the energy flux ($W = \frac{L_s}{4\pi r^2}$) at a distance r from the Sun, with L_s being the solar luminosity ($3.828 \times 10^{26} \text{ W}$) [7].

The incidence of solar radiation (pressure) on the sail area A produces the force and the reflection of photons gives another force of similar magnitude. The resultant force is thus

$$F = 2PA \quad (3.10)$$

This force can be modelled differently based on the phenomena considered. The choice of the model influences to a certain degree the direction and magnitude of the SRP force acting on the sailcraft. Two of these models - ideal sail and optical sail force models - are presented in this section. The first model is based on a perfectly reflective sail, while the latter includes optical phenomena like absorption, emission, diffuse and specular reflection of the photons by the sail. In both the models, the sail is assumed to be flat, rigid and not degrading over time. Before describing the sail force models, important parameters that indicate the performance capabilities of solar sails are defined in the next subsection.

3.5.1. PERFORMANCE METRICS

For the sail to be able to reflect the incoming radiation, it needs to be rigid and stiff. The presence of wrinkles in the sail not only affects the sail efficiency but also creates local hot spots which can damage the sail if the temperature at these points exceed the sail film's temperature limit. Hence,

the sail film is held flat with the help of structures like spars, booms and connected to the rest of the sailcraft (payload, instruments, subsystems) via a hub [7]. These structures form a part of the solar sail assembly mass (m_{SA}), and the metric which indicates the structural efficiency of a solar sail design is called the sail assembly loading (σ_{SA}).

$$\sigma_{SA} = \frac{m_{SA}}{A} \quad (3.11)$$

The sail assembly loading σ_{SA} does not depict the overall performance or efficiency of the sail as it does not include the payload mass (m_{PL}). The ratio of the total mass of the sailcraft m and the sail area A gives the sail loading σ parameter which is independent of sailcraft design and serves as a metric for evaluating sailcraft's overall performance [7].

$$\sigma = \frac{m}{A} = \frac{m_{SA} + m_{PL}}{A} = \sigma_{SA} + \frac{m_{PL}}{A} \quad (3.12)$$

Another parameter, characteristic acceleration a_c , is defined as the acceleration experienced by the sail at the Sun-sail distance of 1 AU with the sail surface oriented normal to the solar radiation. It is calculated based on the SRP at 1 AU (P_0) acting on a sail area A and having a mass m [7]:

$$a_c = \frac{2P_0A}{m} = \frac{2P_0}{\sigma} \quad (3.13)$$

The final design parameter is the lightness number β . It is a dimensionless parameter defined as the ratio of SRP acceleration and solar gravitational acceleration [7]. Since both accelerations are proportional to the inverse square of distance from the Sun, the lightness number is independent of Sun-sail distance. For a sail facing normal to the Sun's radiation, the lightness number is given by

$$\beta = \frac{a_{SRP}}{a_S} = \frac{a_c \left(\frac{r_0}{r}\right)^2}{\frac{\mu_s}{r^2}} = \frac{a_c}{\frac{\mu_s}{r_0^2}} = \frac{a_c}{a_0} \quad (3.14)$$

Considering a_0 to be the solar gravitational acceleration at 1 AU, Equation 3.14 becomes $\beta = a_c/5.93$ (a_c in mm/s^2), providing a direct relation between both the design parameters. The lightness number can also be related to the sail loading parameter as follows [7]:

$$\beta = \frac{\sigma^*}{\sigma} ; \quad \sigma^* = \frac{L_s}{2\pi\mu_s c} \quad (3.15)$$

The critical sail loading parameter σ^* is a function of solar luminosity and mass. Substituting the values for the terms, it is found to be 1.53 g/m^2 . For a sail to have high performance/acceleration capabilities, the sail loading parameter has to be low which in turn would result in high values for the characteristic acceleration and the lightness number.

Any of the above defined parameters can be used to model the sail force, since all the parameters are directly related.

3.5.2. IDEAL SAIL FORCE MODEL

In the ideal sail force (IR) model, the sail is considered to be perfectly reflective and thus, there is no momentum loss due to absorption, transmission or emission of solar radiation. The SRP force, therefore, results from two perfect momentum transfers between the photons and the sail film. As shown in Figure 3.4, the first force component F_i due to photons impinging on the sail surface is in the direction of the solar radiation [7].

$$F_i = PA(\hat{r} \cdot \hat{n}) \hat{r} = PA \cos \alpha \hat{r} \quad (3.16)$$

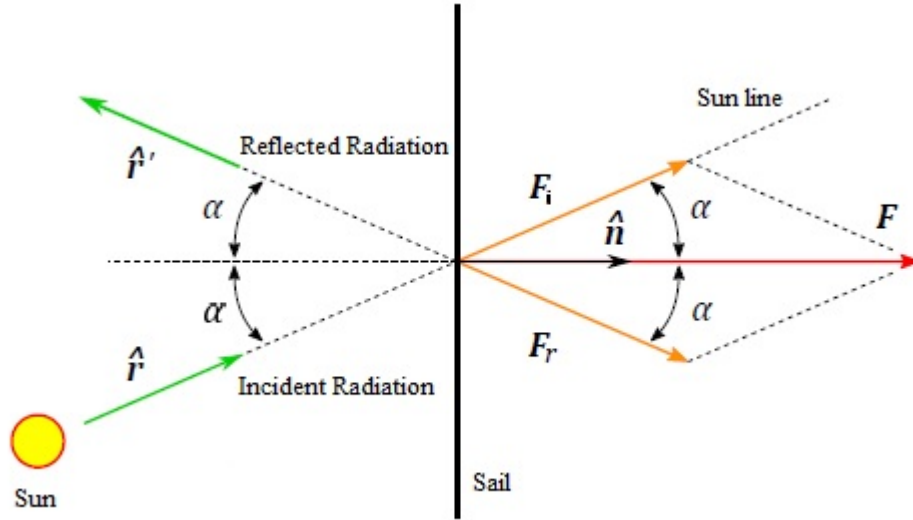


Figure 3.4: SRP Force components in an Ideal sail force model [39].

The second force component F_r from reflection of photons in the \hat{r}' direction is [7]:

$$F_r = -PA(\hat{r} \cdot \hat{n})\hat{r}' = -PA\cos\alpha\hat{r}' \quad (3.17)$$

The resultant force F is the vector addition of these two components,

$$F = F_i + F_r = PA(\hat{r} \cdot \hat{n})(\hat{r} - \hat{r}') \quad (3.18)$$

where the vector difference $(\hat{r} - \hat{r}') = 2(\hat{r} \cdot \hat{n})\hat{n}$. Hence, the total SRP force can be written as [7]

$$F = 2PA(\hat{r} \cdot \hat{n})^2\hat{n} = 2PA\cos^2\alpha\hat{n} \quad (3.19)$$

The acceleration of the sailcraft can be represented in terms of the design parameters by using their definitions from Subsection 3.5.1.

$$F = 2P_0\left(\frac{r_0}{r}\right)^2 A\cos^2\alpha\hat{n} \quad (3.20)$$

$$a = 2\frac{P_0}{m}\left(\frac{r_0}{r}\right)^2 A\cos^2\alpha\hat{n} = 2\frac{P_0}{\sigma}\left(\frac{r_0}{r}\right)^2 \cos^2\alpha\hat{n} \quad (3.21)$$

Using Equations 3.13 and 3.14, the solar sailcraft acceleration becomes [7]:

$$a = a_c\left(\frac{r_0}{r}\right)^2 \cos^2\alpha\hat{n} \quad (3.22)$$

$$a = \beta\left(\frac{\mu_s}{r^2}\right) \cos^2\alpha\hat{n} \quad (3.23)$$

A slight variation of this model exists where the non-ideal effects like wrinkles and billowing are approximated with an overall sail efficiency parameter η . Efficiency values are usually considered in the range of 0.85 to 0.9.

$$a = \eta\beta\left(\frac{\mu_s}{r^2}\right) \cos^2\alpha\hat{n} \quad (3.24)$$

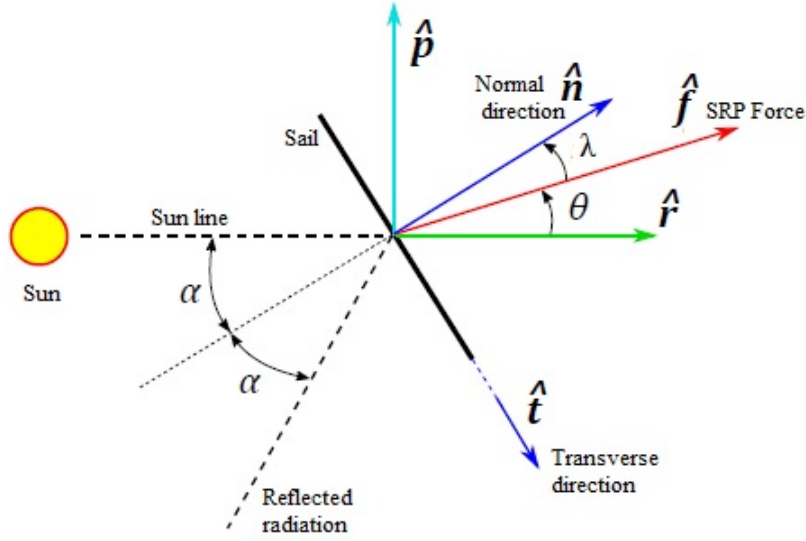


Figure 3.5: Orientation of SRP force in Optical sail force model [39].

3.5.3. OPTICAL SAIL FORCE MODEL

In the real world, losses due to absorption and transmission of solar radiation are present. The Optical sail force (OR) model aims to utilize the sail material's optical properties to determine the SRP force more accurately. A set of six parameters are used to uniquely define the sail optical properties [7], namely

- Reflection coefficient ρ - Fraction of incoming radiation which is reflected
- Specular reflection coefficient s - Fraction of the reflected photons that is specularly reflected
- Sail's front and back surface emission coefficients ϵ_f, ϵ_b
- Front and back surface non-Lambertian coefficients B_f, B_b - Provides the angular distribution of radiation emitted and diffusely reflected by the surfaces

Due to these optical properties, the SRP force is no longer coincident with the sail normal vector. The thrust has components along the sail normal and transverse (in-plane) directions (as shown in Figure 3.5) given by [7]:

$$F_n = PA \left\{ (1 + \rho s) \cos^2 \alpha + B_f \rho (1 - s) \cos \alpha + (1 - \rho) \frac{\epsilon_f B_f - \epsilon_b B_b}{\epsilon_f + \epsilon_b} \cos \alpha \right\} \hat{n} \quad (3.25)$$

$$F_t = PA [(1 - \rho s) \cos \alpha \sin \alpha] \hat{t} \quad (3.26)$$

and the magnitude of the SRP force is:

$$F = \sqrt{F_n^2 + F_t^2} \quad (3.27)$$

Naturally, due to the optical losses, the magnitude of the SRP force is lower than the ideal sail force model. The angle λ represented in Figure 3.5 is known as the centerline angle [39]. It indicates the

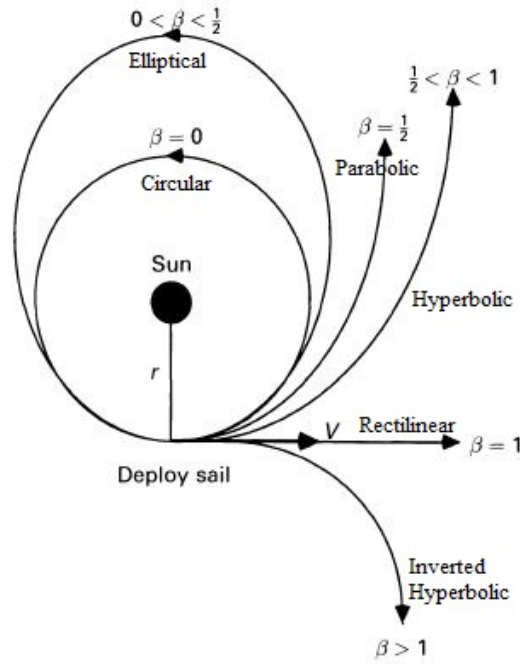


Figure 3.6: Orbit classification based on sail lightness number for $\alpha = 0$ (adapted from [7]).

measure by which the force magnitude of an OR model differs from that of an IR model. The center-line angle is found to increase with the cone angle and hence the difference in thrust magnitude is more pronounced for highly tilted sail orientations. Additionally, among the sail optical properties, only the variations in ρ and s strongly influence the deviation of thrust direction from sail normal.

3.5.4. CHOICE OF SRP FORCE MODEL

Having presented the SRP force models in this section, it is imperative to make a choice regarding the model to be used in formulating the equations of motion. The models can be assessed based on their mathematical complexity and the accuracy of their force description. Using the optical sail force model will provide accurate and more realistic results but the complexity of integrating the equations of motion increases and with it the computational effort needed. As the solar sail model was developed from scratch in the astrodynamics software tool Tudat, a significant amount of time was dedicated to programming, testing the model and integrating it with the existing framework. Although as per the initial thesis planning, optical sail force model was viewed as the second step of the mission analysis, it was not practical to proceed with the complex model due to the time limit on the thesis study. Moreover, since this is a preliminary study exploring the feasibility and benefits of employing solar sails for a comet sample return mission, the need to use complex SRP force models was not rightly justified. Though ideal solar sails do not exist in reality today, the sail materials and coating available are capable of providing 90% reflectivity [11]. In such a case, the difference in time-of-flight (TOF) between IR and OR models are around 5-15% as concluded in [44, 45]. So, by considering an ideal sail force model valuable insights on the mission trajectory can still be obtained. Hence, based on the above considerations, the ideal sail force model with an efficiency factor $\eta = 1$ was adopted for describing the SRP force in this thesis work.

3.6. EQUATIONS OF MOTION

3.6.1. VECTOR FORM

The vector form of the sailcraft's equations of motion (EoM) was introduced in Section 3.3 with the motion described by Equation 3.6. Based on the discussions and choices made regarding perturbations (Section 3.4) and the SRP force model (Section 3.5), the EoM in vector form is rewritten as:

$$\frac{d^2\vec{r}}{dt^2} + \frac{\mu_s}{r^3}\vec{r} = \beta \frac{\mu_s}{r^2} \cos^2 \alpha \hat{n} \quad (3.28)$$

This equation results in a system of three scalar second-order differential equations in Cartesian coordinates which in turn can be written as six first-order differential equations. For a sail normal directed along the Sun-line, i.e. the radial direction ($\hat{n} = \hat{r}$; $\alpha = 0$), the above equation can be simplified to:

$$\frac{d^2\vec{r}}{dt^2} + (1 - \beta) \frac{\mu_s}{r^3} \vec{r} = 0 \quad (3.29)$$

This results in the familiar classical two-body problem equation, with $(1 - \beta)\mu_s$ being the effective solar gravitational parameter. Thus, based on the value of the lightness number β , different conic sections are obtained as the solution for Equation 3.29 as seen in Figure 3.6.

A second class of solutions for Equation 3.28 is obtained for sails which are oriented at a fixed angle with $\alpha \neq 0$. In this case, a family of logarithmic spiral trajectories are obtained instead, as derived in [7]. But for most mission applications, the sail attitude is not fixed at a particular orientation. It has to be steered based on certain strategies in order to reach the mission target. However, the above Keplerian orbit/logarithmic spiral trajectory solutions can be used as a criterion to validate newly implemented solar sail models in software tools.

3.6.2. GAUSS' FORM OF LAGRANGE'S PLANETARY EQUATIONS

Representing the EoM in vector form using Cartesian coordinates is one way of representing the sailcraft's motion. But, as explained in Section 3.2.3, using MEE's expedites the integration of the trajectory and is free from running into singularities. The rate of change of these elements in the presence of a perturbing force is given by the Lagrange's Planetary Equations (LPEs) [36]. LPEs are advantageous for modelling minute variations as they isolate the position movement in orbit through a single fast variable (phase angle). Hence, LPEs capture the motion of the sailcraft, under the influence of continuous, low-thrust propulsion like solar sailing, more precisely. Due to the way in which LPEs are defined, it works only for perturbing forces that can be expressed as a perturbing potential. Therefore, the Gauss form of LPEs are more suitable for representing the EoM, since the perturbations can be expressed as accelerations components.

The EoM of the sailcraft are [46]:

$$\begin{aligned}
\frac{dp}{dt} &= \frac{2p}{w} \sqrt{\frac{p}{\mu_s}} f_S \\
\frac{df}{dt} &= \sqrt{\frac{p}{\mu_s}} \sin(L) f_R + \sqrt{\frac{p}{\mu_s}} \frac{[(w+1) \cos(L) + f]}{w} f_S - \sqrt{\frac{p}{\mu_s}} \frac{[g(h \sin(L) - k \cos(L))]}{w} f_W \\
\frac{dg}{dt} &= -\sqrt{\frac{p}{\mu_s}} \cos(L) f_R + \sqrt{\frac{p}{\mu_s}} \frac{[(w+1) \sin(L) + g]}{w} f_S + \sqrt{\frac{p}{\mu_s}} \frac{[f(h \sin(L) - k \cos(L))]}{w} f_W \\
\frac{dh}{dt} &= \sqrt{\frac{p}{\mu_s}} \frac{s^2}{2w} \cos(L) f_W \\
\frac{dk}{dt} &= \sqrt{\frac{p}{\mu_s}} \frac{s^2}{2w} \sin(L) f_W \\
\frac{dL}{dt} &= \sqrt{\frac{p}{\mu_s}} \frac{[h \sin(L) - k \cos(L)]}{w}
\end{aligned} \tag{3.30}$$

where f_R , f_S and f_W are the components of the perturbing acceleration along the radial, transversal and angular momentum direction respectively; and

$$\begin{aligned}
s^2 &= 1 + h^2 + k^2 \\
w &= \frac{p}{r} = 1 + f \cos(L) + g \sin(L)
\end{aligned} \tag{3.31}$$

Since SRP thrust is the perturbing force acting on the sailcraft, the expressions for acceleration components can be written using Equation 3.23 [7]:

$$\begin{aligned}
f_R &= \beta \frac{\mu_s}{r^2} \cos^3 \alpha \\
f_S &= \beta \frac{\mu_s}{r^2} \cos^2 \alpha \sin \alpha \sin \delta \\
f_W &= \beta \frac{\mu_s}{r^2} \cos^2 \alpha \sin \alpha \cos \delta
\end{aligned} \tag{3.32}$$

Solving this set of six first-order differential equations requires the implementation of numerical integration methods, which are covered in the next chapter.

4

NUMERICAL TOOLS

This chapter covers the numerical tools used in this research for optimizing the trajectory of the sailcraft. The initial part of the chapter focuses on integration method, followed by parts on optimization algorithms. Integrators provide the way for solving the equations of motion formulated in the previous chapter. Some of the widely used integration methods are briefly introduced and the choice of the integrator opted for trajectory propagation is also explained.

Once the integrator is set up, propagation of the sailcraft over time can be simulated. The trajectory, thus simulated will be based on the initial state and conditions. However, the aim of the research is to find the trajectory which fulfills the mission requirements best. In order to find the best possible trajectory, optimization algorithms are used. The performance of an algorithm depends on the particular problem as well as the settings of the respective algorithm. Therefore, after covering some basic aspects of optimization, the choice of the algorithm best adapted for the problem dealt in this thesis work is discussed in detail.

4.1. INTEGRATOR

The equations of motion of the sailcraft need to be solved to propagate the sailcraft in time and obtain the state history of the sailcraft. A closed-form analytical solution cannot be obtained for the Equations 3.30, due to the presence of perturbing acceleration terms. Alternately, numerical integration techniques need to be used to estimate how the state and other parameters of the sailcraft vary with time. The integration process is repeated at small discrete time steps covering the entire propagation period and the state of the sailcraft is determined at each of these time steps.

Numerous integration methods exist having different properties and possessing problem-specific advantages. Below, a set of the commonly used integration methods, ranging from single-step, fixed stepsize integrator (RK4) to multi-stage, variable stepsize integrator (DOPRI8(7)) are provided. This set of integrators were short-listed considering their availability in the astrodynamics software tool (Tudat) used for trajectory simulation in this research.

- The Euler Integrator is based on first-order Taylor series expansion, requiring only the first derivative. The state at the next epoch is given by a linear relation of the constant step size (h), thus resulting in a truncation error of the order $\mathcal{O}(h^2)$. The Euler method is computationally inexpensive but does not produce accurate results for astrodynamics problems. It is typically suited for functions with linear variation.

- Runge-Kutta (RK) fixed step-size methods are also derived from Taylor series, but instead of having to derive application-specific higher-order terms, an approximation is used by calculating the slope at different points within each integration step. The RK4 integrator uses four function evaluations to compute the state at the next epoch and the increment function Φ is the result of their weighted mean [47]. Thus, an RK4 integrator is more accurate than an Euler method having a truncation error of the order of $\mathcal{O}(h^5)$.

$$\Phi = \frac{1}{6}(k_1 + 2k_2 + 2k_3 + k_4) \quad (4.1)$$

Higher-order RK methods can be formulated by including more terms for intermediate function evaluations and their corresponding coefficients. But determining the coefficients becomes increasingly difficult with more function evaluations.

- Variable step-size RK methods offer improvement over the standard RK methods. For the various phases of the trajectory different step-sizes are utilized to achieve uniform accuracy. In variable step-size RK methods, the function y approximation at next epoch $t_0 + h$ is formulated as [47]:

$$y(t_0 + h) = y_0 + h\Phi \quad (4.2)$$

with the increment function Φ given by

$$\Phi = \sum_{i=1}^s b_i k_i \quad (4.3)$$

where s is the number of function evaluations.

$$\begin{aligned} k_1 &= f(t_0 + c_1 h, y_0) \\ k_i &= f(t_0 + c_i h, y_0 + h \sum_{j=1}^{i-1} a_{ij} k_j) \quad (i = 2 \dots s) \end{aligned} \quad (4.4)$$

The coefficients a_{ij} , b_i and c_i are selected such that the order p of the local truncation error (LTE) is as high as possible. The coefficients are also set to follow the conditions in Equation 4.5. The values of the coefficients are represented in a *Butcher's Table* [47].

$$\sum_{i=1}^s b_i = 1 \quad c_1 = 0 \quad c_i = \sum_{j=1}^{i-1} a_{ij} \quad (i > 1) \quad (4.5)$$

For efficient step-size control, an RK method of neighbouring order (with the same number of function evaluations) is embedded to yield two independent approximations of order p and $p - 1$. Using the two approximations, an estimate ϵ of LTE of the lower-order integrator is obtained. Based on the error tolerance ϵ_{req} specified, the time step is rescaled accordingly.

$$h_{req} \approx h \left(\frac{\epsilon_{req}}{\epsilon} \right)^{\frac{1}{p-1}} \quad (4.6)$$

After the time step modification, there are two approaches for proceeding with the integration step - (i) to use the lower-order method or (ii) to use the higher-order method. Methods that use the lower-order approach for integration are Runge-Kutta-Fehlberg RKF4(5), RKF5(6) and RKF7(8). Dormand and Prince formulated the DOPRI8(7) method which uses the higher-order approach for integration.

- Multi-step methods use the integration results from previous steps for estimating the function value at the current time step. These methods work by storing results and using them for further calculations, which makes it advantageous for certain applications.

$$y(t_{i+1}) = y(t_i) + h \sum_{j=0}^s b_j f(t_{i-j}, y_{i-j}) \quad (4.7)$$

$$t_{i-j} = t_i - jh$$

An interpolating polynomial is set between previous s data points and the integral of the polynomial is used to extend the polynomial to the next epoch t_{i+1} . Examples of multi-step method are Adams-Moulton, Adams-Bashforth and Predictor-Corrector methods.

4.2. INTEGRATOR CHOICE

As discussed in the previous section, there are many options available for the choice of integrator. The integrator best suited for an application depends on the dynamics involved in the problem. For applications involving transfer trajectories, the integrator should be capable of modeling elliptical or near-parabolic motion precisely. This requires an adaptive and variable step-size integration as additional evaluations need to be performed when the spacecraft is moving faster (close to pericenter) in order to accurately capture the position and velocity changes. Furthermore, when there is no significant change in spacecraft's position/velocity (close to apocenter), the integrator should be able to take larger time steps to reduce the computation time. Since the transfer trajectory to and back from the comet using solar sailing will be elliptical (osculating) in nature, variable step-size RK methods are better suited for the problem than fixed step-size methods like Euler and RK4. Meanwhile multi-step methods provide very good precision for complex problems, but the complex mathematics involved and high computation time overcome the benefits.

Within the variable step-size integrators, two approaches have been distinguished in [47] - (i) lower-order integration methods like RKF4(5), RKF5(6) and RKF7(8) and (ii) higher-order integration methods like DOPRI8(7). That is, for example in DOPRI8(7), the 8th-order method is used for calculating the solution and the 7th-order method is applied for stepsize control. The application of the methods is inverse for lower-order integration methods. Thus, integration performed using DOPRI8(7) results in superior solutions when compared with lower-order methods like RKF7(8), though both are embedded methods of order 7 and 8. Due to the requirement of approaching the comet within a narrow distance margin of 250 km, higher importance was given for solution accuracy over robustness in integration step-size. Hence, DOPRI8(7) was found to be the suitable integrator for the problem considered in this thesis and was hence used for solving the equations of motion and propagating the sailcraft in time.

4.3. OPTIMIZATION

The objective of optimization is to find the control parameters which minimize (or maximize) an objective function, with constraints placed on the parameters. Mathematically, an optimization problem can be defined as

$$\min_{x \in \Sigma} f(x) \quad \text{subject to} \quad g(x) = 0 \quad \text{and} \quad h(x) \leq 0 \quad (4.8)$$

where f is the objective function, x is the decision vector based on which optimization is performed, and g and h are the equality and inequality constraints respectively.

In optimization problems pertaining to spacecraft trajectories, the aim is to determine the optimal spacecraft state history $\mathbf{x}[t]$, which fulfills the mission requirements in the best possible way. The motion of the spacecraft will be influenced by external forces, like gravitational attraction, or forces generated by propulsion systems. These external or internal variable parameters, along with the initial (t_0) and/or end epoch (t_f), form the control vector $\mathbf{u}(\mathbf{t})$ based on which the dynamics of the trajectory varies. Using this decision or control vector, attributes of the mission like ΔV , time-of-flight, mass of propellant etc. are to be minimized. One or more of these attributes define the cost function J . Hence, the optimal trajectory of the spacecraft must comply with the dynamic constraints $\dot{\mathbf{x}}(\mathbf{t}) = \mathbf{G}(\mathbf{x}(\mathbf{t}), \mathbf{u}(\mathbf{t}))$ (resulting from its equations of motion) and boundary constraints $\mathbf{x}(\mathbf{t}_f) = \mathbf{x}_T(\mathbf{t}_f)$, while minimizing the cost function \mathbf{J} .

For low-thrust propulsion systems like solar sailing, as dealt with in this thesis, a combination of factors namely initial state $\mathbf{x}(\mathbf{t}_0)$, gravitational force from bodies and thrust from the propulsion system determines the trajectory shape. The SRP thrust from the Sun is active throughout or for a major portion of the transfer time and the thrust vector can basically point in any direction opposite to the Sun (ideal sail). Thus, a steering strategy which provides the direction of the thrust acceleration vector throughout the transfer time, plays the major role in determining the trajectory of a solar sailcraft. The steering strategy given in terms of sail orientation can be a continuous varying parameter with a wide range of values. This makes solar sail trajectory optimization a challenging task.

The problem of finding the optimal state history $\mathbf{x}^*(\mathbf{t})$ is thus transformed to determining the optimal control $\mathbf{u}^*(\mathbf{t})$, which is equivalent to finding the two sail steering angles α and δ as a function of time t . As already seen in Section 2.3, for an effective sample collection from the comet's coma, the sailcraft should perform a close approach rendezvous or flyby at the comet. This means that the sailcraft's position and velocity (for a rendezvous) should match with that of the comet at the point of closest approach. Therefore, for the solar sailcraft to rendezvous with the comet, the goal is to find a control vector history $\mathbf{u}[t]$ which forces the sailcraft state $\mathbf{x}(\mathbf{t}) = (\mathbf{r}(\mathbf{t})^T, \dot{\mathbf{r}}(\mathbf{t})^T)^T$ from initial value $\mathbf{x}(\mathbf{t}_0)$ to the state of comet $\mathbf{x}_T(\mathbf{t})$ along a trajectory that minimizes a cost function \mathbf{J} for the transfer. Since solar sailing is a low-thrust, propellant-free propulsion technique, the actual optimization objective is to minimize the flight time Δt .

$$J = \int_{t_0}^{t_f} dt = t_f - t_0 = \Delta t \quad (4.9)$$

However, spacecraft trajectory optimization problems usually can have multiple objectives. Some of the objectives can be contradictory to other functions considered. So, a solution cannot generally fulfill all criteria to the best extent possible, i.e. if for one criterium its best value is obtained, it might not be the case for others. Tackling such multi-objective optimization demands high computational effort. So, in practice, multi-objective problems are transformed into a single-objective problem using one of the following approaches [48]:

- A priori method of considering a weighted sum of the different objective functions which are normalized to accommodate their different dynamic ranges. Determining the appropriate weight factors can be challenging and requires knowledge about potential solutions of the problem.
- The Interactive or progressive approach utilizes the knowledge gained while optimization is in progress. An expert will be able to effect changes to the weights by monitoring the process

periodically. Though this approach offers refinement in applying weights, the possibility of introducing a bias towards some objectives still exists.

- In a posteriori approach, a set of competing solutions are analyzed without biasing the result by imposing weights. From the set of equally compelling possibilities, a solution is selected through implicit application of weights. Algorithms employing a posteriori weight preference are based on the concept of Pareto-optimality. But, the major drawbacks of such algorithms is their lower speed and the uncertainty in find Pareto-optimal solutions.

Once the problem has been reduced to a single-objective optimization, various methods can be applied to determine the optimal solution for the above-mentioned rendezvous/flyby trajectory. The methods differ in their approach and/or execution, having their own merits and demerits. Analytical methods, based on Calculus of Variations (COV) and solving a Two Point Boundary Value Problem (TPBVP), are among the earliest methods developed. In these methods, the control vector $\mathbf{u}(t)$ is considered as a continuous function and has an infinite solution space. Apart from this, the mathematics gets complicated when constraints are placed on variables or function values. Hence, analytical solutions are possible only in very rare cases and for problems involving rendezvous or flyby, such solutions are in fact unknown.

Alternatively, numerical methods reduce the problem complexity by transforming it into a finite-dimensional problem. The discretization of time from being a continuous entity into τ finite intervals changes the control vector parameter space to $n_u\tau$ dimensions. As a result, computation is simplified and numerical optimization techniques are capable of accommodating multiple constraints and/or objective functions. The numerical optimization techniques can be broadly classified into - (i) local trajectory optimization methods (LTOMs) and (ii) global trajectory optimization methods (GTOMs). Information about both methods is provided in the next section, discussing their benefits and drawbacks.

4.3.1. LTOM AND GTOM

LTOMs are numerical methods employing mathematical concepts derived from calculus of variations and optimal control theory. LTOMs can be further categorized as direct and indirect methods, with Non-Linear Programming (NLP) and Hill Climbing being an example of the respective categories [49]. The common functional aspect of LTOMs is that an initial guess, in terms of either initial control vector history $\mathbf{u}[t]$ or starting adjoint vector of Lagrange multiplier $\lambda(\mathbf{t}_0)$, is needed. The initial guess is obtained by simulating the trajectory based on the transfer settings and the generation of the initial guess has to be repeated if the LTOM does not converge. The main benefits of LTOMs are [49]:

- As the methods have proven mathematical foundations, LTOMs are deterministic and their operations are well understood.
- The results of LTOMs are highly accurate and perfectly match the boundary conditions of the problem.

while drawbacks of LTOMs are:

- Convergence of LTOM for a given initial guess input is not guaranteed as similar initial guesses can give dissimilar results.
- The result of LTOM depend on the initial guess provided and generating the guesses requires expert level knowledge in optimization.

- If the initial guess is far from the global optimum, LTOMs have the tendency of resulting in a local optimum close to the initial guess in the solution space.
- The trajectory problem is transcribed into a system of linear equations in many LTOMs. Solving these equations demand a substantial computational effort in terms of storage and CPU time.

On the other hand, GTOMs operate by coding the problem into a black-box function which presents the functional relationship between decision vector and cost function. The optimization routine begins with an arbitrary initial candidate from the solution space and iteratively progresses towards the optimum based on the method. As GTOMs do not need an initial guess from the user, the optimization process remains unbiased and the need for expert level knowledge is no longer a requirement [49]. The search process generally continues until (i) the best possible solution is found, (ii) no improvement can be observed in the results after a certain number of iterations, (iii) the maximum process time is exceeded, or (iv) an internal parameter causes the algorithm to terminate. A large number of GTOMs have been developed over the years, some of which are inspired from nature or other fields of science. These methods differ in the way how - (i) new generation of candidate solutions is created, (ii) solutions are evaluated, and (iii) search parameters are used. The major advantages of GTOM are [49]:

- The search space of GTOM is not confined to the vicinity of the initial candidate solution.
- Most GTOMs start from a randomly initialized parameter set, i.e. the process is independent of any initial guess.
- Initial conditions like launch epoch t_0 and velocity v_0 can also be optimized along with the control vector.
- Convergence of GTOMs depend on the problem, its formulation and the values opted for the algorithm's control parameters.

GTOMs suffer from the following disadvantages [49]:

- The way in which the problem is formulated and coded plays a crucial role in algorithm's performance to find the global optimum.
- The results of GTOMs have lower accuracy than LTOMs results due to the algorithm's focus on finding the global optimum in the solution space.
- Since GTOMs are heuristic (and non-deterministic) in nature, multiple runs with the same initial conditions are needed to confirm a previously found optimum.

4.3.2. CHOICE OF OPTIMIZATION METHOD

In this subsection, the selection of the optimization method which will be used in this research is discussed. Firstly, the choice between LTOM and GTOM for the trajectory problem considered is analyzed. The drawback of LTOM as mentioned in the previous section is that LTOMs require an initial guess to start the optimization process. It is difficult to estimate an initial guess as it requires a good insight about the problem and the mathematics behind optimal control theory. Moreover, convergence of LTOMs is sensitive to the initial guess and if the solution does not converge, the complete process from generating a new initial guess has to be repeated. Furthermore, when convergence is achieved, solutions of LTOMs often turn out to be local optima close to the initial guess. The above

issues cause the optimization process using LTOMs to be time consuming, requires periodic monitoring and expert intervention. Due to the above reasons and ability of GTOMs to extensively scan the solution space for the global optimum, only GTOMs were considered for further selection.

Among GTOMs, many of the popular methods like Genetic Algorithm (GA), Differential Evolution (DE), Simulated Annealing (SA) and Particle Swarm Optimization (PSO) have been applied to trajectory optimization problems in the past. A study under ESA's Advanced Concepts Team [50], comparing the performance of these methods, found DE to be the most promising method for a low-thrust direct planet-to-planet transfer problem. The methods were compared on aspects like - (i) finding the Pareto-optimal solution, (ii) ability to locate the basin of attraction of optimal solutions, and (iii) number of function evaluations and runtime. The results obtained by DE were not only close to the best known solution but were also found after fewer function evaluations than other methods. Another comparative study performed by Spaans and Mooij [51], concluded that DE was best among the methods considered in terms of the fitness value obtained and population size used for determining the optimal trajectory for a solar polar sail mission.

Additionally, DE is available as part of the open source PAGMO (Parallel Global Multiobjective Optimizer) library [52] from ESA's Advanced Concepts Team. The tool is highly versatile and flexible in using the existing methods. The PAGMO library can be used in conjunction with the astrodynamics toolbox Tudat, which was developed at TU Delft and hence, had the advantage of major technical support. Therefore, considering the technical and practical aspects, DE was selected for optimizing the solar sailing trajectories in this thesis. The main operating principle and features of DE are presented in the next section.

4.4. DIFFERENTIAL EVOLUTION

DE is a heuristic global optimization technique developed by Storn and Prince in 1994. The method has a wide applicability and can be utilized for minimizing even non-linear and non-differentiable continuous functions. DE belongs to the family of evolutionary algorithms (EA) and thus, has its inspiration from biological evolution [53]. Like other EAs, DE follows the process of initiation, mutation, crossover and selection. The unique aspect of DE over other EAs is that a new generation is formed by taking the weighted difference between two members and adding it to a third member of the current generation. This makes the algorithm completely self-organizing and prevents the need for a separate probability distribution. The step-by-step operation of DE is described below.

Initiation

In DE, a population of vectors is defined as [53]

$$P_{x,g} = (x_{i,g}), \quad i = 0, 1, \dots, NP - 1, \quad g = 0, 1, \dots, g_{max} \quad (4.10)$$

$$x_{i,g} = (x_{j,i,g}), \quad j = 0, 1, \dots, D - 1 \quad (4.11)$$

where NP is the population size, index g represents the generation number and D is the number of parameters in the decision vector. Unlike GA which uses binary parameters, DE is a real parameter optimization with the elements $x_{j,i,g}$ of vectors represented as real numbers. Hence, DE searches for the global optimum in a D -dimensional real-parameter space \mathbb{R}^D . At the start of optimization, the D elements of NP decision vectors are randomly generated and initialized as

$$x_{j,i,0} = \text{rand}_j[0, 1] \cdot (b_{j,U} - b_{j,L}) + b_{j,L} \quad (4.12)$$

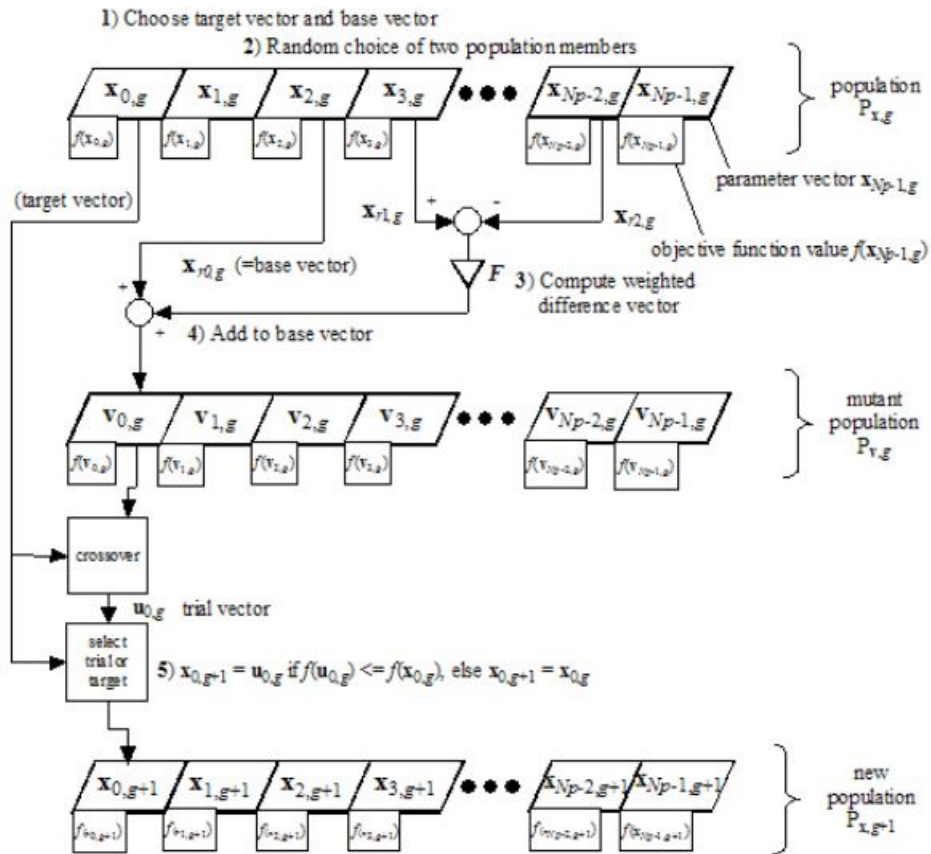


Figure 4.1: Schematic of differential evolution optimization routine [54].

with b_U and b_L being the upper and lower bounds of the parameters in the decision vector [53]. The term $\text{rand}_j[0,1]$ generates a uniformly distributed random number between 0 and 1.

Mutation

The mutant vector $v_{i,g}$ is formed by taking the vector difference of two randomly chosen vectors in the current generation and adding the scaled difference to a third vector $x_{r1,g}$ [53]

$$v_{i,g} = x_{r1,g} + F(x_{r2,g} - x_{r3,g}) \quad (4.13)$$

where F is the weight factor which controls the extent of deviation between the two vectors, and has a value between 0 (no mutation) and 1.

Crossover

Following mutation, the target vector and mutant vector are combined to form a trial vector $u_{i,g}$ and diversify the population. The extent of mixing between the vectors is determined by the crossover factor CR . Two types of crossover are possible - (i) exponential and (ii) binomial [55]. In exponential crossover, a random element among the D parameters is chosen. This element acts as a starting point in target vector from where the exchange of L integer elements with the mutant vector begins.

$$u_{j,i,g} = \begin{cases} v_{j,i,g} & \text{for } j = \langle n \rangle_D, \langle n+1 \rangle_D, \dots, \langle n+L-1 \rangle_D \\ x_{j,i,g} & \text{for all other } j \in [1, D] \end{cases} \quad (4.14)$$

whereas in a binomial crossover, for every element of the vector, a random value is generated in the range of $[0,1]$. If this value is lower than CR , crossover occurs and the original value of the target vector is replaced by the corresponding value from the mutant vector. For $CR = 0$, no crossover occurs and when $CR = 1$, the elements of trial vector are completely from the mutant vector.

$$u_{i,g} = u_{j,i,g} = \begin{cases} v_{j,i,g} & \text{if } (\text{rand}_j[0,1] \leq CR) \\ x_{j,i,g} & \text{otherwise} \end{cases} \quad (4.15)$$

Selection

The final step of the process is selection. In this step, each individual of the new generation is defined. The new generation is populated by comparing the trial $u_{j,i,g}$ and target $x_{j,i,g}$ vectors, and the one with a lower fitness value is selected for the next generation. This ensures that the fitness status of the population improves or remains the same but never deteriorates. A schematic of the optimization using DE is shown in Figure 4.1.

$$x_{i,g+1} = \begin{cases} u_{i,g} & \text{if } f(u_{i,g}) \leq f(x_{i,g}) \\ x_{i,g} & \text{otherwise} \end{cases} \quad (4.16)$$

DE Variants

Similar to the two types of crossover, there can be some variations in the mutation step. Therefore, based on the choices for mutation and crossover, DE can be classified according to the following convention: DE/x/y/z [55], where x denotes the option for base vector (*best* or *rand*), y is the number of vector differences considered for mutation (1 or 2) and z represents the type of crossover used (*bin* or *exp*). The variant described earlier for mutation uses one weighted difference and adds it to a random base vector $x_{r1,g}$. This along with a binomial crossover is denoted as: DE/*rand*/1/*bin*. Considering the various options as seen above, 10 DE variants were identified in [55] and have been defined in the PAGMO library. Among these variants, DE/*best*/1/*bin* was found to yield best performance in terms of both accuracy and robustness, irrespective of the characteristics of the problem to be solved. This is also confirmed by the study done in [51], where DE/*best*/1/*bin* outperformed other algorithms in finding the global optimum. Therefore, the DE/*best*/1/*bin* variant was selected for optimizing the solar sailing comet sample return trajectory in this research.

4.5. GRID SEARCH

DE provides an effective method of finding the global optimum. In cases with many parameter problems, sometimes DE is able to only reach the basin region of the optimal solution, as it handles a large search space. So, the solution obtained is close to global optimum but not having the required accuracy. In order to locate the global optimum from the solution of DE, a local search technique can be used.

Grid Search (GS) is one of the local search methods, and is simple to program and execute. GS was employed in this research to improve the trajectory results obtained from DE, as reported in Chapter 6. GS works by overlaying a uniform grid on the parameter space and evaluating the objective function at each of the grid points [56]. The resolution of the grid determines the accuracy of the results and also the computation time. Low-resolution grids are much faster to search but potential solutions within narrow portions of the parameter space could be missed. Whereas for high-resolution grids, the accuracy of results are improved but at the cost of high computation time. Therefore,

grid searches are conducted first over a broader parameter space and later focused onto the region around the best point obtained. The main drawback of GS is that it becomes computational intractable for problems with many parameters, resulting in a multi-dimension parameter space.

5

VALIDATION AND PARAMETER TUNING

With the theoretical foundations of the research established through the previous chapters, the next part of the report focuses on the application of those concepts in the software program to solve the research problem. Prior to the actual trajectory simulation, the astrodynamics models and numeric tools used in the program have to be verified and validated to confirm if their implementation is working as intended. This step is highly essential in any scientific research to ensure a sense of reliability and credibility to the results obtained. As the simulation consists of existing plus the new software modules, through verification the proper working of these modules is examined. By comparing the outcome of the simulations with previous research results from literature, the functioning and results of the program can be validated.

In addition to the validation of the astrodynamics models and numeric tools, the chapter also covers the tuning of integrator and optimizer. The integrator and optimizer contain important parameters in their set up whose value influence the performance of these numeric tools. Hence, to exact an optimal performance from the tools, the impact of these parameters was analyzed and the best settings were selected at the end of the tuning process. The same reference cases were considered for tuning and validation, to enable testing of the settings during tuning process.

In the first part of the chapter, the validation of the newly implemented solar sail acceleration model is presented. Following this, the tuning and validation of the integrator is explained in Section 5.3. The final part of the chapter is dedicated to describing the analysis performed to find the best combination of parameter settings for the optimizer. The reference case for tuning was also used for optimizer validation.

5.1. SRP ACCELERATION MODEL VALIDATION

The SRP acceleration existing in Tudat was a simple cannon-ball radiation model, which calculates the force exerted on an effective spacecraft area by assuming normal incidence for the solar radiation. This model is applicable for measuring the perturbation due to SRP on a satellite orbit around Earth. Further, this model does not accommodate any of the solar sail design parameters and sail orientation angles, which are crucial for describing a solar sailing trajectory. Therefore, a solar sail acceleration model was developed and implemented in Tudat for this research. The model estimates the acceleration due to SRP based on the sailcraft's position, sail's orientation (cone and clock angle) and lightness number as given by Equation 3.23. It was added to the existing acceleration models interface in Tudat.

This new feature addition to Tudat had to be tested and verified before applying it in simulations. The preliminary check that was carried out was to verify if the parts of the model performed correctly at the function level. So, the solar sail acceleration function, which provides the output in the orbital reference frame (Subsection 3.1.2), was tested on four test cases each with inputs covering different scenarios. The first case takes up the situation when the sail normal vector is perpendicular to the Sun-line which is like the thrust OFF mode for solar sailing, i.e. no radiation impacts the sail. In the second case, the solar sail acceleration model is compared with the existing cannon-ball radiation pressure acceleration model. Since the cannon-ball model assumes a normal incidence of solar radiation, the test case is formulated for a sail with $\beta = 0.0015312$ ($m = 1\text{kg}$ and $A = 1\text{m}^2$) and oriented at $\alpha = 0^\circ$, $\delta = 0^\circ$.

Test Case	β	α	δ	Tudat result	Reference value
OFF mode	0.05	90°	-	(0, 0, 0)	(0, 0, 0)
Cannonball model at distance of 1AU	0.0015312	0°	0°	$(9.080725 \times 10^{-6}, 0, 0)$	$(9.080725 \times 10^{-6}, 0, 0)$
Sail at Venus orbit	0.05	35.26°	10.8°	$(3.08524 \times 10^{-4}, 4.0872 \times 10^{-5}, 2.14260 \times 10^{-4})$	$(3.08524 \times 10^{-4}, 4.0872 \times 10^{-5}, 2.14260 \times 10^{-4})$
Sail at Mars orbit	0.05	65.83°	270°	$(8.76680 \times 10^{-6}, -1.953437 \times 10^{-5}, 0)$	$(8.76680 \times 10^{-6}, -1.953437 \times 10^{-5}, 0)$

Table 5.1: Static validation of solar sail acceleration model.

For the third and fourth cases, sails were given an arbitrary orientation and position in the orbits of Venus and Mars respectively, and were considered to confirm whether the orientation angles were processed correctly by the function. For these two cases, the results are compared with the evaluation of Equation 3.23 in MATLAB. This is done in order to verify the magnitude of the SRP acceleration obtained from the model and to note the difference in value (error) if any. All the four test cases are listed in Table 5.1, along with their corresponding inputs, reference values and the result obtained in Tudat. From the table, it can be seen that for all the four cases, the outcomes of the function in Tudat perfectly matches with the reference values. Additionally, a second test was performed to obtain the 'force bubble' [57], which is characteristic of the variation in solar sail force components for the range of possible cone angles $[-\pi/2, \pi/2]$. The Figure 5.1 indicates the envelope of possible radial and transverse component values with the maximum radial force obtained for $\alpha = 0^\circ$ as anticipated. In view of the above results, it can be confirmed that the sail acceleration function has been defined properly.

5.2. SAILCRAFT DYNAMICS VALIDATION

The test cases discussed above have validated the model for the static conditions, i.e. without considering the motion of the sailcraft. Additional features of the SRP acceleration model come into play when the dynamics of the sailcraft are considered. These include the transformation of the acceleration from the orbital reference frame to the ECLIPJ2000 and time (or node) based changes of sail orientation angles. Validation of these aspects of the model are done by simulating the sailcraft trajectory based on a reference case.

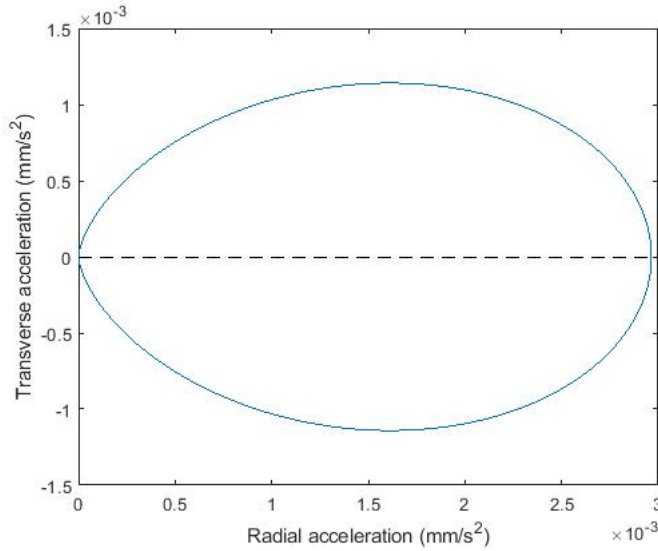


Figure 5.1: Force bubble computed for an ideal solar sail with $\beta=0.05$ at 1AU.

The solar sail trajectory optimization presented in [58], for an interplanetary Earth-Mars transfer mission, was selected as the reference case to conduct the verification tests. In the reference, the optimization problem is considered as a two-dimensional orbit-to-orbit transfer without employing the actual ephemeris of the planets. This simplifies the problem with the sail cone/pitch angle α being the only source of control as the clock angle $\delta = 0^\circ$. The steering of the sailcraft was provided by discretizing the trajectory into N segments, i.e. $N+1$ nodal points and using a piecewise constant function for the pitch angle. In the paper, a simplified optical sail force model was utilized for describing the sailcraft acceleration as given below [58]:

$$a = a_c \left(\frac{r_0}{r} \right)^2 \cos \alpha [b_1 \hat{r} + (b_2 \cos \alpha + b_3) \hat{n}] \quad (5.1)$$

with b_1 , b_2 , b_3 equal to 0.0864, 0.8277 and -5.45×10^{-3} respectively. The dynamics of the sailcraft were represented in polar coordinates (r, θ, u, v) . The minimum-time optimization problem was solved by converting it to a non-linear programming problem (NLP) and employing a successive quadratic algorithm (SQP) algorithm. The time-optimal trajectories and their corresponding pitch angle profiles were provided in the paper for characteristic accelerations (a_c) of 1 and 2 mm/s^2 .

Initial Position	$r(0)$	1.496×10^{11} m
	$\theta(0)$	0 rad
Initial Velocity	$u(0)$	0 km/s
	$v(0)$	29.78 km/s
Final position	$r(t_f)$	2.279×10^{11} m
Final velocity	$u(t_f)$	0 km/s
	$v(t_f)$	24.13 km/s
Time-of-flight	t_f	450 days

Table 5.2: Trajectory conditions for the Earth-Mars mission. [58]

This trajectory is replicated in Tudat using the cone angle profile as shown in Figure 5.2a. The trajectory constraints (Table 5.2) as considered in the original problem were implemented in the Tudat

simulation. Since the acceleration model in Tudat uses the sail lightness number as the design parameter, the corresponding value of $\beta = 0.168$ for $a_c = 1 \text{ mm/s}^2$ was applied. The Gauss modified equinoctial propagator (Section 3.6.2) and DOPRI8(7) integrator (Section 4.1) were used for the trajectory simulation. The resulting trajectory to the orbit of Mars is shown in Figure 5.3.

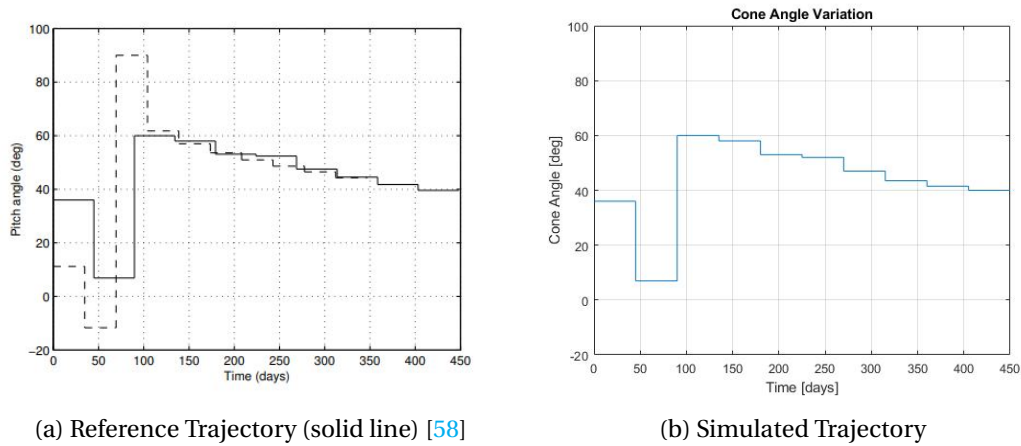


Figure 5.2: Cone Angle Profile.

Comparing the trajectory obtained from Tudat (right) with the reference trajectory (left), a very close match can be observed. This proves that the acceleration frame transformation and processing of input sail angles have been implemented and functioning properly.

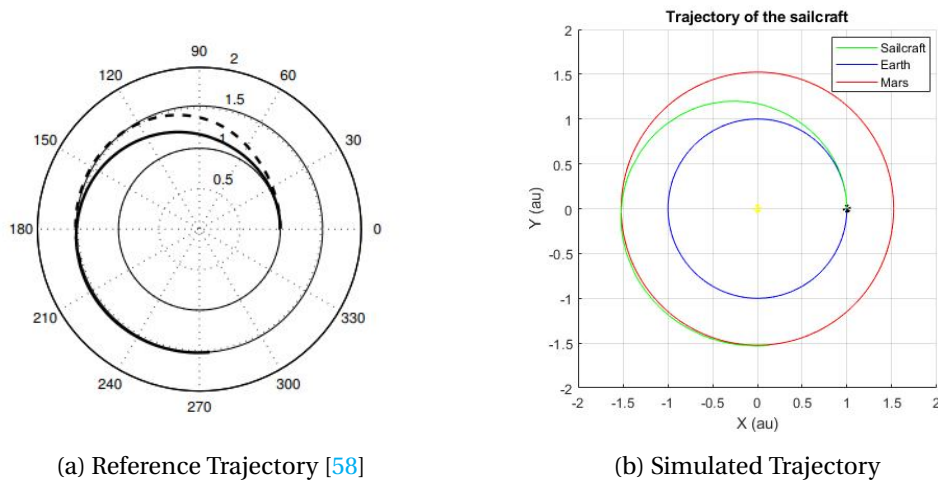


Figure 5.3: Representation of reference and simulated trajectories to Mars.

5.3. INTEGRATOR TUNING

The implementation of DOPRI8(7) in Tudat requires the specification of initial time step, minimum and maximum step size, and absolute and relative error tolerances. Values provided for these parameters can widely influence the performance of the integrator, affecting step size, truncation errors and number of evaluations. Therefore, the integrator needed to be tuned to have the appropriate settings for obtaining a precise sailcraft trajectory. Sailcraft trajectories were simulated for different values of the parameters mentioned before. The simulation results were evaluated based

on accuracy and computation time.

A simple trajectory to the outer Solar System was simulated for tuning the integrator. The initial position of the sailcraft was taken to be just outside the sphere of influence of Earth with no hyperbolic excess velocity. Throughout the simulation, the sailcraft was assumed to have a constant (arbitrary) orientation. The solar radiation pressure and gravitational force from the Sun were the only forces acting on the sailcraft. The trajectory was propagated using Gauss form of Lagrange Planetary Equations (Section 3.6.2). The simulations were carried out for a period of two years, considering it to be representative of the transfer time to our target comet Hartley 2. The simulation settings are summarized in Table 5.3.

Start Epoch	t_0	Jan 1, 2020
Initial State	$x(t_0)$	Earth's state at t_0
Excess Velocity	v_∞	0 km/s
Lightness Number	β	0.168 ($a_c=1\text{mm/s}^2$)
Cone Angle	α	18°
Clock Angle	δ	105°
Time-of-flight	t_f	2 years

Table 5.3: Trajectory simulation settings for integrator tuning.

Simulations were performed first to determine the values for minimum and maximum step sizes. Three set of values were tried, namely $(10^{-6}, 10^6)$, $(10^{-9}, 10^9)$ and $(10^{-12}, 10^{12})$, for the minimum and maximum step size combination. DOPRI8(7) being a variable step size integrator selects time steps based on the dynamics of the trajectory and within the limits specified. For the first combination, the maximum step size of 10^6 seconds was not adequate as the integration time steps turned out to be constant (10^6), irrespective of the tolerance value (except 10^{-15}) selected. Whereas in the second $(10^{-9}, 10^9)$ and third $(10^{-12}, 10^{12})$ combination, the variable integration time steps, on average in the order of 2 million seconds, were well within the provided limits. However, since the solar sailing trajectory is not a very fast evolving trajectory, $(10^{-12}, 10^{12})$ setting could be a bit computationally excessive, considering that $(10^{-9}, 10^9)$ combination works adequately. The reason for considering small values ($<10^{-6}$) for the minimum step size is due to the large number of minuscule integration steps taken by the integrator near the nodal points, in order to represent the sudden change in the dynamics of the sailcraft. The steps were of the order of 10^{-6} or lower in case of higher error tolerance. Therefore, the minimum and maximum step sizes of the DOPRI8(7) were fixed at 10^{-9} and 10^9 seconds, respectively.

The next two settings - relative and absolute tolerances - determine the step size control of the DOPRI8(7) integrator. The simulations were performed for tolerances (both absolute and relative) varying from 10^{-15} to 10^{-10} , increasing by a factor of 10 for the next simulation. The difference in position was calculated with respect to the simulation results for the tolerance of 10^{-15} , as it can be concluded as the most accurate among the tolerances considered. By using a variable step-size integrator, the various tolerances considered have different integration/propagation times. In order to calculate the error in position with respect to 10^{-15} tolerance, the state history data of other tolerances were interpolated using an 8th order Lagrange interpolator to the time values of 10^{-15} tolerance.

The error in sailcraft position determined for various tolerances is shown in Figure 5.4. From the plot, the error margins of the tolerance settings over the period of propagation can be observed.

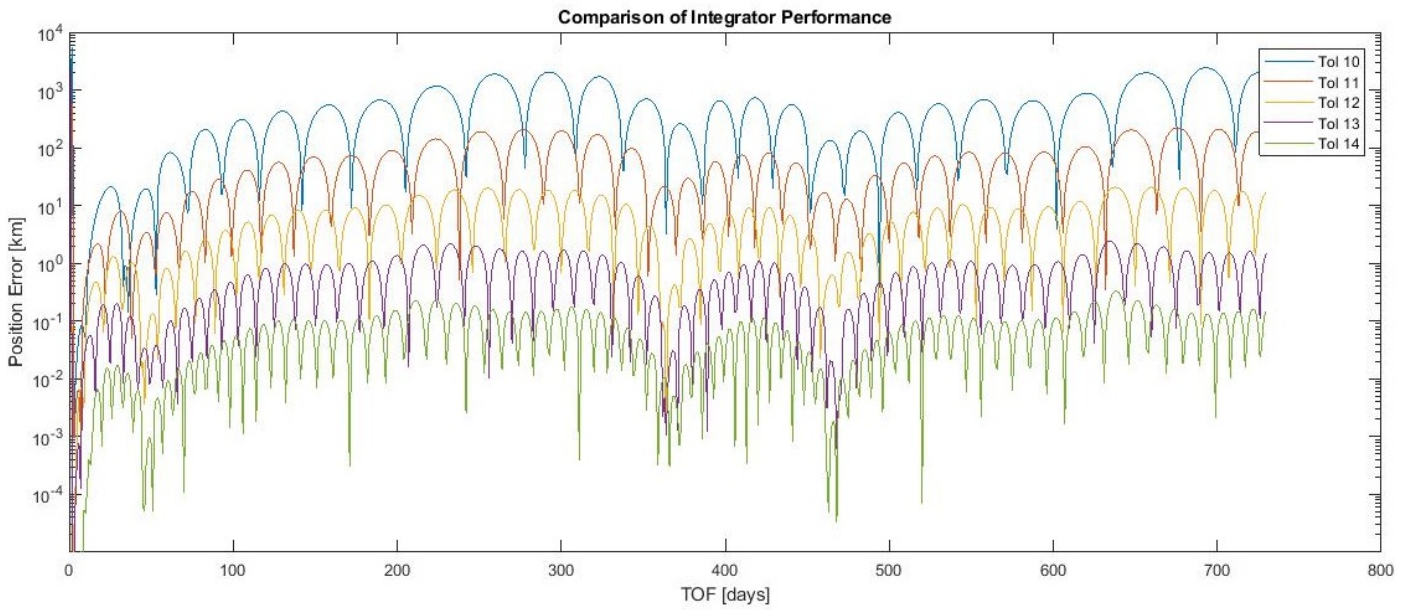


Figure 5.4: Comparison of Integrators based on position Error

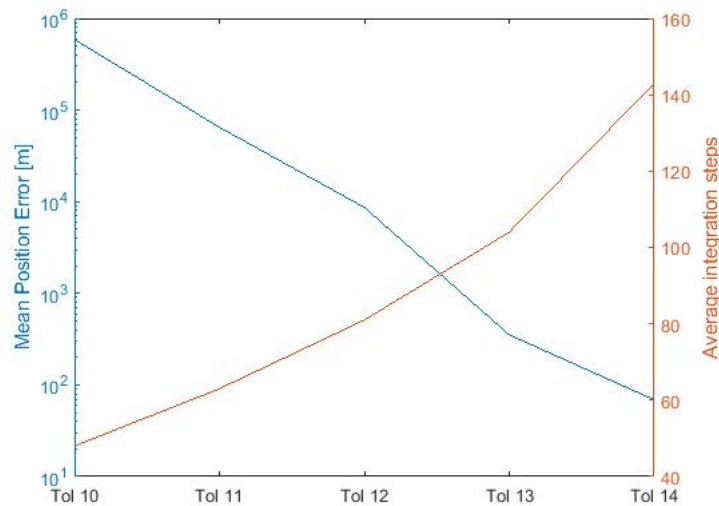


Figure 5.5: Integrator tolerance trade-off between accuracy and computation time.

Based on the range of the error in position, a tolerance value of 10^{-14} has the lowest error in order of 100 m, while a tolerance 10^{-10} has the largest error in order of 1000 km. But, selection of precise tolerance setting like 10^{-14} has the drawback of requiring high computation time. As optimization algorithms need to evaluate tens of thousands of trajectories, quick integration also plays a vital role along with accuracy. A trade-off between these two criteria has been plotted in Figure 5.5, comparing the mean position error and average integration steps taken for each of the tolerance settings. The CPU time is not used for the trade-off here as it varies with other background programs running simultaneously in the system.

Figure 5.5 clearly shows an increase in integration steps/time with lower tolerance values. The tolerance settings of 10^{-12} and 10^{-13} have the best outcomes from the trade-off with good accuracy and

moderate computation time. However, since in this research, the objective of the mission is to reach the comet within distances of hundreds of km, the error margin in the order of 10 km for tolerance setting 10^{-12} is still significant. Hence, the relative and absolute tolerances for the DOPRI8(7) integrator were set with a value of 10^{-13} . The integrator was thus tuned and the settings derived from the process have been applied for trajectory simulation in the rest of the thesis work.

5.4. INTEGRATOR VALIDATION

Similar to the model validation in Section 5.2, a reference study was considered from literature and the trajectory is recreated based on the given initial conditions but using the tuned integrator settings. Further, since in Section 5.2, the actual ephemeris was not considered for simulation, the current opportunity is used to verify the ephemeris settings in Tudat as well. The optimization of solar sailing Earth-Venus rendezvous trajectories, analyzed by G.Hughes in his PhD dissertation [59], is chosen for validating the integrator.

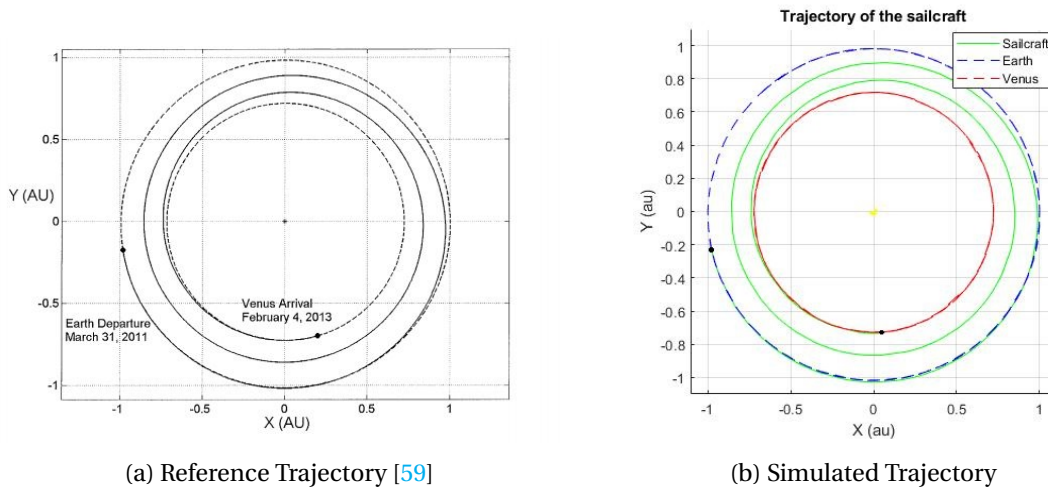


Figure 5.6: Representation of reference and simulated trajectories.

The optimal trajectory for the Earth-Venus rendezvous in [59] was determined for a solar sailcraft with a characteristic acceleration of 0.2 mm/s^2 . The corresponding lightness number value of 0.0337 was adopted for the simulation in Tudat. The sailcraft was again assumed to depart with zero hyperbolic excess velocity from Earth's position in its orbit around the Sun. In the study [59], the optimal departure date was searched in the period from 2010-2020 and was found to be March 31, 2011. The optimal trajectory departing on this date reached Venus in 676 days and is shown in Figure 5.6a.

Based on the above information, the Earth-Venus rendezvous trajectory was simulated in Tudat using the DOPRI8(7) integrator, having an error tolerance of 10^{-13} . The resulting trajectory is presented in Figure 5.6b. Comparing the reference and simulated trajectories, it can be observed that the motion of the sailcraft has been almost perfectly recreated. The slight phase difference in the final position of sailcraft between the two plots can be attributed to the way in which sail orientation angles were modelled in both the cases. The sail orientation angles for the reference trajectory were described as continuous, oscillatory curves in [59]. Since the SRP acceleration model in Tudat is based on piecewise nodal angle representation, a discrete approximation of the cone and clock angles, as shown in Figure 5.7, were utilized for the simulation. Even with this approximation, the obtained trajectory has confirmed the correct working of the integrator. Moreover, along with the

simulation result from Section 5.2, the performance of the SRP acceleration model has been successfully validated for both the two-dimensional case with no ephemeris and the three-dimensional case with ephemeris trajectory propagation.

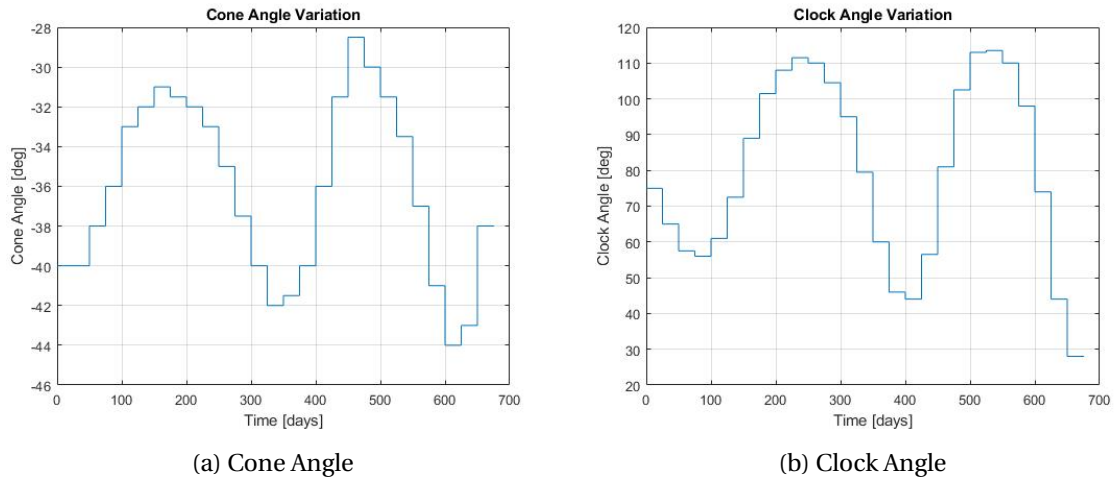


Figure 5.7: Sail orientation angle profiles for Earth-Venus trajectory.

5.5. DE TUNING

With the performance of the SRP acceleration model and the integrator successfully validated, the next most important numeric tool is the optimizer. As already introduced in Section 4.4, DE is a heuristic global optimization technique. It belongs to the class of evolutionary algorithms, and operates by modifying the population members and finding the improved solution over the generations. DE's performance is influenced by the values of the parameters - population size NP , mutation weight F and crossover factor CR . For the algorithm to perform well and determine near-global optimal solutions, the functional parameters have to be set to their optimal values, which may vary according to the optimization problem. Hence, the DE parameters were tuned in order to aid the optimization process. The parameters were analyzed based on the solutions obtained and the computational effort required.

For the Earth-Venus rendezvous used for tuning the optimization parameters, the sailcraft is assumed to depart from Earth's position (just outside SOI) with no hyperbolic excess velocity. A sailcraft with a sail lightness number of 0.05 is considered for the transfer. The trajectories are simulated considering the actual ephemeris of bodies. The decision vector consists of the sail orientation angle and departure epoch. The search for the optimal departure date is confined to the synodic period (584 days) of Venus, starting from January 1, 2011. Other integrator and propagator settings remain the same as the ones chosen for this thesis work.

The results of the tuning process are discussed in this section. A rendezvous trajectory to Venus was opted for tuning the DE parameters due to the proximity of Venus's orbit to Earth's, which is similar to the actual comet's perihelion passage, and availability of literature for this transfer. In the first part of the section, the formulation of the objective function which has to be minimized by the optimizer is presented. As will be seen in this section, the objective function is a weighted combination of multiple objectives. The sensitivity of the results to the variation in weights was

also analyzed and the best combination was selected. Following this, the population size and node distribution were analyzed and set. Finally, in the last part of the section, the DE optimizer settings are completed by deciding on the F and CR combination.

5.5.1. OBJECTIVE FUNCTION

The objective of time-optimal trajectories generally contains only the time-of-flight term in the objective function. Due to the requirements set on the mission trajectory, other terms related to the sailcraft's position and velocity were included as constraints in the objective function. This is also the case because of the way in which constraints are handled in PAGMO's implementation of DE. DE by its definition works on minimizing a single objective or fitness term. So, multiple objectives have to be combined into a single objective by following one of the methods mentioned in Section 4.3. A priori approach of combining the multiple functions as weighted sums was adopted due to its simple implementation. Although determining the set of non-dominated or Pareto-optimal solutions is more effective, considering the number of functions, dimensions of the problem and time limit for this thesis work, the simpler weighted sum approach was selected.

The choice for the objective function is made after pre-planning for the sample return mission to the comet Hartley 2. Since, for that mission, the sailcraft is required to make a rendezvous with the comet, the position and velocity of the sailcraft should match with that of the comet. This forms two of the objectives for minimizing the distance and velocity between sailcraft and the comet. As it is also desired for the sailcraft to tag the comet - observing and collecting samples - a possible match in the orbital elements of the sailcraft and comet (at the rendezvous point) is considered as well. In order to verify and test the above considerations, the same has been adopted for the Earth-Venus rendezvous (validation) mission. Therefore, the various components of the multi-objective cost/fitness function are:

- Time-of-flight (TOF) - The transfer time from Earth to the target. It is normalized by a factor of three years, since the optimal transfer time from reference was 676 days [59].
- Distance to target (Δr) - This is the distance of the closest approach to the target during the course of the trajectory. In order to make the distance parameter of order 10^0 , it was normalized by 10^9 m (a million km).
- Relative velocity (Δv) - The relative velocity between the sailcraft and the target at the point of closest approach. It has been normalized to km/s.
- Orbital elements (Δa , Δe , $\Delta \omega$, $\Delta \theta$) - The match in orbital elements can be considered like a penalty function. The difference in semi-major axis is normalized in the same way as Δr , while the angles $\Delta \omega$, $\Delta \theta$ are normalized with their range 2π and eccentricity (already in range 0-1) is left as such.

The normalization factors considered above are intended to bring all the terms of the objective function in the same magnitude range. So, the sum of these terms having equal weight factors of 1, forms the basic objective function around which the sensitivity of each term is tested

$$J = \Delta t' + \Delta r' + \Delta v' + \Delta a' + \Delta e + \Delta \omega' + \Delta \theta' \quad (5.2)$$

where the prime notation denotes normalized terms. The sensitivity of objective function J was studied by increasing the weight of terms (by a factor of 10) one-by-one. For each of those cases, the optimization algorithm was run for 50 seed numbers with a population size of 100 and a nominal

value of (0.5,0.5) for the (F,CR) combination. The outcome of this sensitivity study is shown in Figure 5.8 in which, each term on the X-axis implies a weight factor of 10 on that term with rest remaining same as the nominal formulation in Equation 5.2.

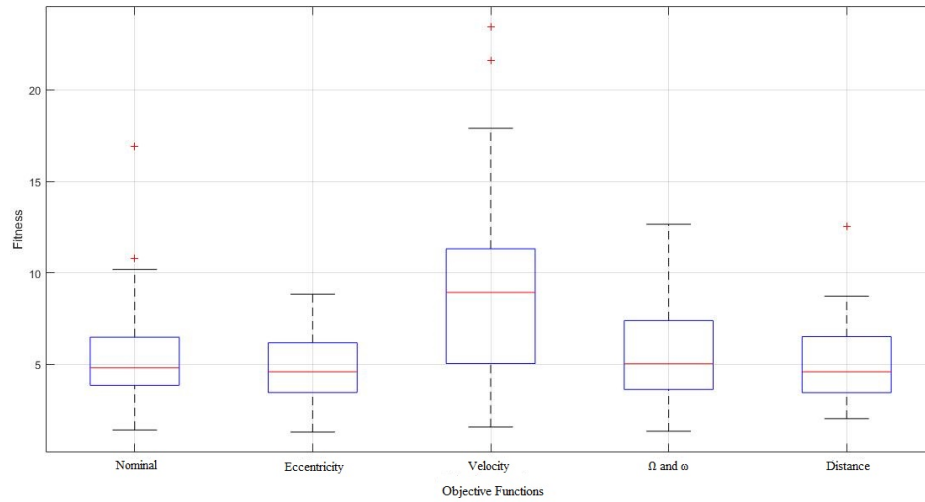


Figure 5.8: Comparison between various objective function formulation.

The figure shows the box plots, which indicate the range of the data within 25 and 75 percentile as the box with the whisker ends showing the minimum and maximum values. The red cross markers indicate potential outliers in the data. In the plot, the terms on the x-axis indicate the different objective function settings, with the mentioned term carrying additional weight factor over the rest of the terms in each case. From the figure, it can be noticed that the additional weight to the relative velocity does not improve the fitness compared to the nominal objective function (Equation 5.2). Only the optimization runs with more weight on eccentricity and distances show improvement from the nominal case. The minimum value for fitness among all the cases is obtained for the eccentricity case. Apart for achieving minimum fitness, it is important to attain it consistently. Even in terms of consistency, the objective function with weight on eccentricity performs better than all other functions, by having a smaller range for fitness values and no outliers. Hence, the objective function with additional weight factor on eccentricity was used for rest of the tuning process.

5.5.2. NODE VS POPULATION SIZE

The number of nodes considered for representing sail orientation also affects the performance of the DE optimizer. The dimension of the search space is determined predominantly by the number of nodes considered. So, an increase in the number of nodes, in turn increases the dimensionality of the problem, making it more difficult for DE to find the global optimum. Whereas if sail orientation is varied at very few nodes, the dynamics of the sailcraft will not be sufficiently represented. Thus, optimization runs with different nodal settings are done to determine the right combination along with the population size. The same simulation setting was used with the updated objective function containing additional weight on the $\Delta e'$ term. Four different population sizes of 50, 100, 200 and 300 were analyzed for the orientation angle setting with 4, 8 and 12 nodes. Overall 12 cases were compared based on 20 seeded optimization runs per case.

Figure 5.9 shows the box plots of the fitness values obtained for every case. The immediately noticeable observation is that the fitness values get better with an increase in population size, irrespective

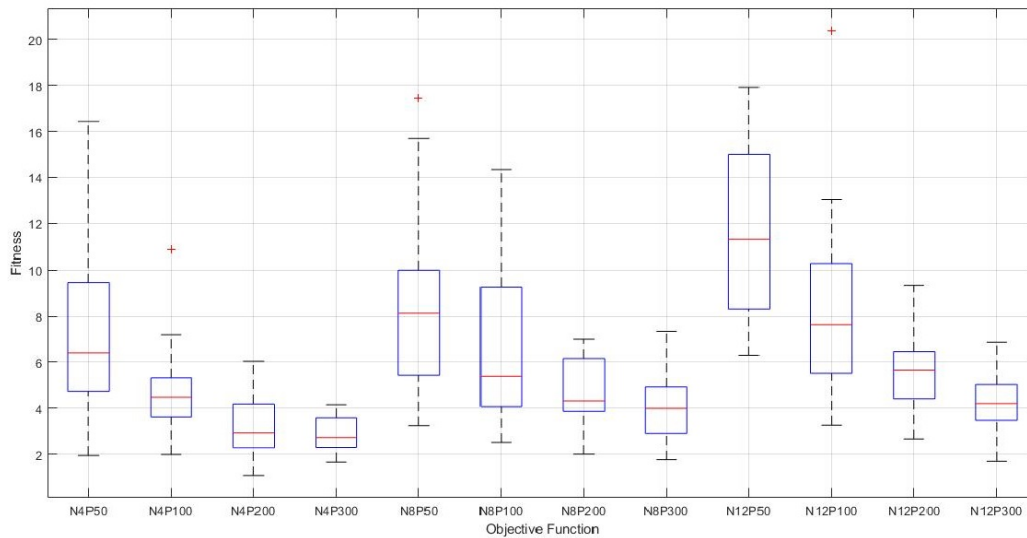


Figure 5.9: Comparison between different Node(N)-Population(P) combinations.

of the number of nodes assumed. Another interesting fact from the plot is that the fitness values are slightly better for lower number of nodes, with the N4P200 combination arriving at the lowest fitness among the 12 cases. However, N4P200 is not the best solution, as the fitness range of N4P300 is much smaller indicating that the setting provides very consistent and robust results at the end of optimization. The drawback of selecting the N4P300 combination is that the number of function evaluations to be done before converging at a solution is almost double the number of function evaluations needed for N4P200. This increases the computational effort significantly as the DE algorithm has to be run for multiple seed numbers. Therefore, in view of the computation time, the second-best N-P combination of 4 nodes and a population of 200 members was selected for the DE algorithm.

5.5.3. F AND CR COMBINATION

The combination of mutant and crossover factors introduce new members into the population and convergence of the algorithm. For low values of F - CR , the probability of introduction of new members into the population is less, so there is risk of pre-mature convergence, i.e. the algorithm would not have searched the parameter space sufficiently. While for higher values, the new members are given more preference and important characteristics of existing members may not be retained. In this case, it takes a longer time for the algorithm to converge. Hence, a right balance between these parameters is need for optimal functioning. For tuning the F - CR parameters, 16 combinations were considered with each parameter having the values from the set 0.2,0.4,0.6,0.8. Each combination was run for 20 seeded runs and the result is shown in Figure 5.10.

From the plot, the (0.2,0.8) and (0.4,0.8) combinations can be observed to have lowest average and minimum fitness values. The fitness range of the (0.2,0.8) combination is slightly larger compared to that of (0.4,0.8). So, the $F=0.4$ and $CR=0.8$ combination provides the best, consistent and robust results. Therefore, the (0.4,0.8) F-CR combination was incorporated in the DE algorithm settings.

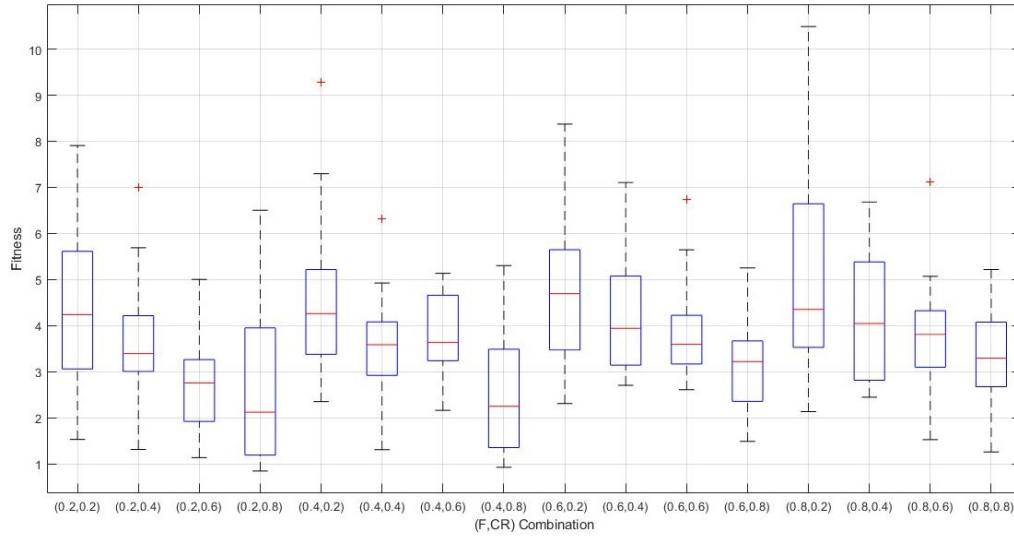


Figure 5.10: Comparison between different F - CR combinations.

5.6. DE VALIDATION

The parameters related to DE optimization have been tuned in the previous section, so as to make the algorithm optimally search for near-global minima. To verify that the tuned parameters work as intended, the algorithm was tested on the rendezvous mission to Venus, as executed in the reference [59]. As the same reference case was discussed in Section 5.4 on integrator validation, the best trajectory obtained after optimization was compared with the previously simulated trajectory.

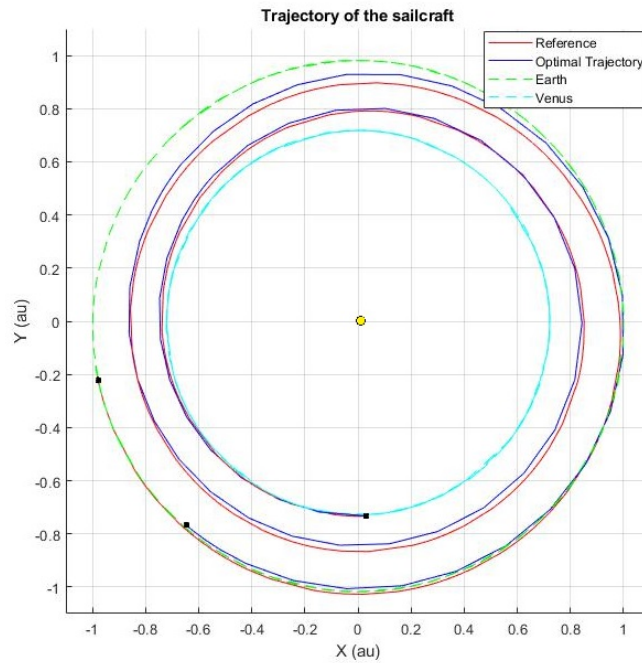


Figure 5.11: Optimal rendezvous trajectory to Venus used for DE validation.

Departure time	t_0	May 13, 2011
Arrival time	t_f	February 8, 2013
Time-of-flight	TOF	636.8 days
Approach distance	Δr	2.3×10^5 km
Relative velocity	Δv	67.4 m/s
Difference in semi-major axis	Δa	107 km
Difference in eccentricity	Δe	0.0019

Table 5.4: Results of the optimal trajectory for Earth-Venus validation case.

A solar sailcraft with a lightness number of 0.0337, equivalent to $a_c = 0.2 \text{ mm/s}^2$, was considered. As the optimal departure date was also to be determined, the search bounds were provided as starting from January 1, 2010 and having a timespan of 584 days (synodic period of Venus). The sailcraft was assumed to depart from Earth's heliocentric orbit around the Sun, without any excess velocity. Based on the node and population size setting, the decision vector consisted of four cone angles, apart from the departure time and time-of-flight. In order for the sailcraft to rendezvous with Venus, its final position should be within Venus's sphere of influence ($r_{SOI} \approx 6 \times 10^5$ km) and also match its velocity. Using the above conditions and the tuned settings for the optimizer, the DE algorithm was run. Since the initial population is formed by randomly generated chromosomes, different runs can produce different results. Therefore, the optimization was repeated for 20 seeded runs. The best trajectory resulting from DE was improved by performing a grid search to determine the departure epoch more accurately and consequently decrease the approach distance to the comet as well. The optimal trajectory thus obtained is plotted in Figure 5.11 along with the reference trajectory (from Figure 5.6b).

By comparing the optimal and reference trajectories, it can be seen that both trace similar paths to reach Venus, with the optimal trajectory starting 43 days after the reference departure date (March 31, 2011). This difference is however compensated as the time taken to arrive at Venus with the optimal trajectory is around 637 days, compared to 676 days with reference trajectory. As a result both the trajectories arrive at Venus within a span of just 4 days (t_f of reference trajectory is February 4, 2013). This proves that the DE algorithm with the tuned settings in place, is capable of providing competing results. Moreover, the additional terms in the objective function also seem to have been fulfilled as shown in Table 5.4. The sailcraft is able to approach Venus within its SOI and the relative velocity between them is merely 67 m/s, which is negligible when compared to Venus's orbital velocity of 35 km/s. Furthermore, the optimal trajectory has also closely matched the orbital elements of Venus at the rendezvous point. This makes it possible for the sailcraft to follow Venus (or a target body in general) in its orbit, which is a desirable result for sample return missions to small bodies like comets. With the success of verifying the DE settings and the advantageous results produced by the algorithm, the optimization procedure has been validated.

6

RESULTS

Having discussed the mission background, theory, numerical tools and program settings, this chapter is dedicated to present the results of the problem conceived as the research goal of this thesis work. All the theoretical studies, programming and validation exercises explained in the previous chapters, have laid the foundation for the results to be shown here.

The process of finding an optimal trajectory for a comet sample return mission is quite challenging, owing to the high-energy, highly eccentric nature of comet orbits. As thus far in the report, all the simulations and validation cases were done for coplanar transfers between bodies in circular orbits, the optimization of comet sample return trajectory was considered in two steps. In the first step, an outbound trajectory to the comet 103P/Hartley 2 from Earth- the first leg of the mission - was optimized. Following this, the optimization of the overall sample return trajectory was performed as the final step. For both cases, the optimal trajectory results were analyzed and the performance of the DE algorithm was evaluated. Modifications to the optimization settings/conditions were incorporated based on the solutions obtained. The conditions and settings for the outbound trajectory to the comet are explained, and the best result found is presented in Section 6.1. The implementation and results of grid search as a local search method is also described. In a similar manner, the analysis of comet sample return trajectory results are provided in Section 6.2.

6.1. OUTBOUND TRAJECTORY TO 103P/HARTLEY 2

The outbound trajectory to comet Hartley 2 has been realized as the initial analysis needed to optimize the sample return trajectory. The orbit of the comet is highly eccentric, inclined (as shown in Table 2.1) and different from the planetary orbits considered so far. This has an impact on the optimization settings. For instance, the departure date timespan can no longer be considered as the synodic period, due to the eccentricity of the comet orbit. As one of the mission requirements, the entire sample return mission is planned to be completed within a ten-year period between 2020-2030. Before this time period, the comet was at its perihelion on October 28, 2010. Based on its orbital period (6.46 years), the comet's next perihelion passage was found to occur in September 2023, which is around 1370 days after the start of the decadal time period. As the perihelion distance of the comet is 1.05 AU, the comet will also approach Earth at its closest distance during this perihelion passage. So, based on this time period and considering time needed for transfer, the departure date timespan was considered to be three years.

The sailcraft was assumed to depart from Earth's heliocentric orbit, just outside of its SOI and without any hyperbolic excess velocity. Thus, determining the optimal departure time would provide the

initial position and velocity of the sailcraft. Actual ephemeris of the bodies (Sun, Earth and Hartley 2) were used in the simulation. A sailcraft with a nominal performance sail, having a lightness number of 0.05 (corresponding to $a_c \approx 0.3 \text{ mm/s}^2$) was considered for the mission. An ideal sail force model was used for modelling the SRP force acting on the sail. The sailcraft moved under the influence of the solar gravitational force, with the SRP thrust force acting as a perturbation. The equations of motion of the sailcraft were represented in the Gauss form of Planetary Equations with modified equinoctial elements. The trajectory was propagated in Tudat using the DOPRI8(7) integrator with the tuned settings.

The trajectories were optimized using the settings derived from tuning the parameters as specified in the previous chapters. The DE/best/1/bin variant algorithm with a population of 200 members was utilized for optimization. The mutant and crossover weight factors were set at 0.4 and 0.8 respectively. The number of decision vectors is mainly affected by the consideration of sailcraft dynamics and node distribution. For a two-dimensional trajectory with four node points, only the sail cone/pitch angle contributes to steering the sailcraft, resulting in four angles in the decision vector. But when the transfer is considered in three dimensions, the number of angles needed for steering doubles. The DE algorithm does not have the same effectiveness for this increase in parameters, as can be seen from the preliminary results obtained for a three-dimensional transfer which are provided in the Appendix A. The larger the number of parameters D in the decision vector, the more difficult it will be for the DE algorithm to narrow in on the global optimum, due to the increase in the dimension of the solution space \mathbb{R}^D . This is especially relevant, when extending the three-dimensional transfer to the entire sample return mission. The number of angles to be determined by the optimizer increases to 16 and, along with the departure time and time-of-flight, the total number of decision variables becomes 18. Owing to the complexity of the low-thrust problem in itself and the multiple objectives in place, the probability of obtaining solutions that satisfy the mission requirements is not very compelling for a three-dimensional transfer. Therefore, the problem of optimization of solar sail trajectories to (and from) the comet was limited to two-dimensional transfers.

Another aspect of the mission which had to be modified from previous optimization runs was the objective function. For the optimization runs until now, the objective function expressed by Equation 5.2 was employed. The aim of the objective function is to find rendezvous trajectories that minimize the time-of-flight and also to match the orbital elements at the point of closest approach. Preliminary runs for an outbound trajectory to the comet indicated the difficulty in matching all of the constraints mentioned in the objective function. This can be primarily attributed to the vast contrast between the initial and target orbits. The sailcraft which is initially in a circular Earth orbit ($e = 0$, $r = 1 \text{ AU}$) has to meet the conditions at the comet which is in moving in an orbit with $a = 3.46 \text{ AU}$ (around 518 million km) and $e = 0.694$. Such a drastic change in a and e requires a strong propulsive force. Since solar sails with $\beta = 0.05$ results in a slowly evolving trajectory and given the time period of the mission, the demands on orbital elements are difficult to fulfill. This has been proven by performing optimization runs for high-performance solar sails with $\beta = 0.3$. The reader is referred to the Appendix B for more information about these runs. However, with the current level of technology such high-performance sails are still not practical. As an alternative approach, the sailcraft with $\beta = 0.05$ can be made to evolve in its orbit for many years in order for it to have gained enough energy to match the comet's orbit. But this would exceed the time period considered for the mission and could prove critical as the sail degrades with radiation impact. Hence, to have realistic sail performance and complete the mission within the span of 10 years, only time-of-flight, distance to the comet and relative velocity terms were considered in the objective function for the optimization runs presented in this chapter.

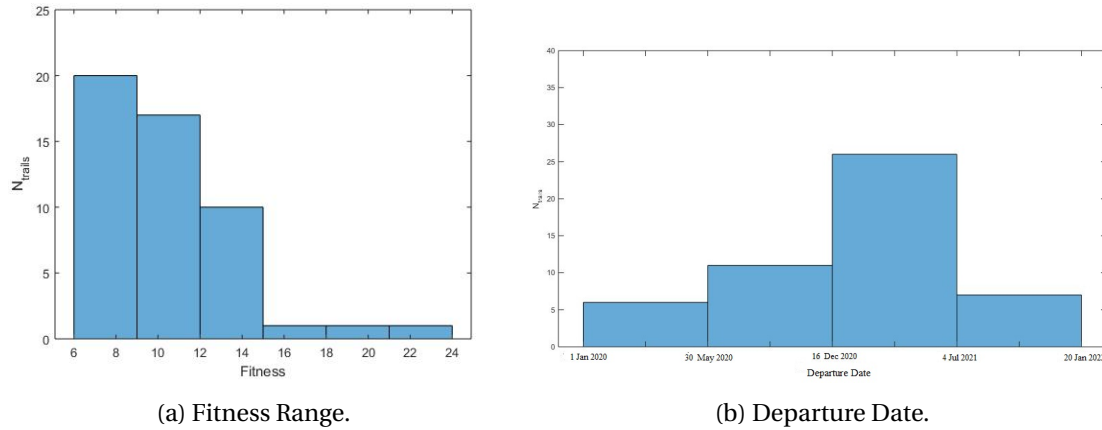


Figure 6.1: Histogram of the fitness and departure dates obtained for 50 runs to optimize the outbound trajectory to comet Hartley 2 (Y-axis indicates the N_{trials}).

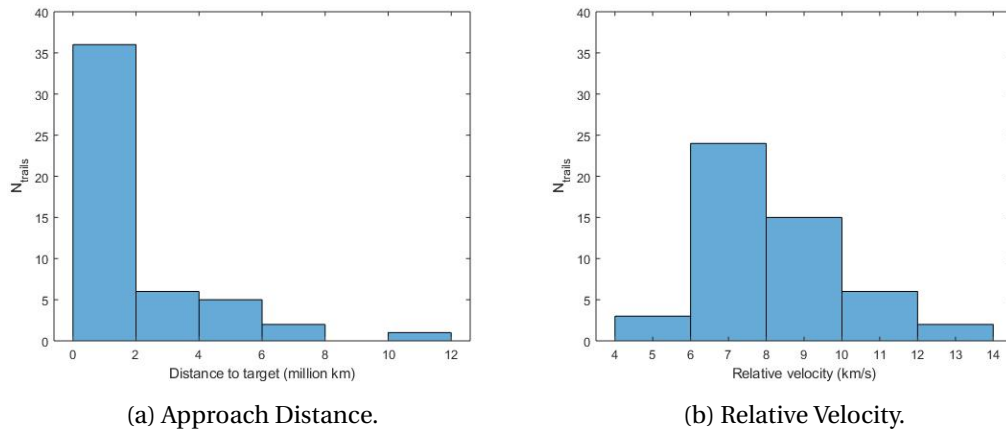


Figure 6.2: Histogram of approach distance and relative velocity obtained for 50 runs to optimize the outbound trajectory to comet Hartley 2 (Y-axis indicates the N_{trials}).

With the settings as discussed in this section, optimization runs for outbound trajectories to Hartley 2 were performed. Due to the heuristic nature of DE, optimization runs were repeated for 50 different seed numbers. The range of fitness/objective function values obtained is shown in the form of an histogram in Figure 6.1a. Similar plots are shown for the approach distance, relative velocity and departure date in Figures 6.1b, 6.2a and 6.2b. These plots indicate the performance of the DE algorithm. The fitness values are focused in the range between 6 and 14. This can also be seen from Table 6.1 providing data on the optimization run results. The main factor contributing to these fitness values is the relative velocity between the sailcraft and the comet. The reason for the high relative velocities is due to the inability of the solar sailcraft, with nominal performance sail, to gain this velocity in the short timespan available. For reference, IKAROS - the only interplanetary solar sailcraft to have flown till now - had gained only 0.4 km/s speed 3 years after its deployment.

Although from Figure 6.2a it can be noticed most optimization runs result in approach distances in the order of 0-2 million km with the minimum being around 100,000 km, these values are still significantly higher than what is desired (< 1000 km) for the mission. So, the approach distances have to be reduced further to enable effective sample collection. For this purpose, the grid search

	Average	Std. Deviation
Fitness	10.5358	3.2912
Departure time (JD)	2459248	170.225
Time-of-flight (days)	983.36	157.66
Approach distance (km)	1,734,320.65	1,353,609.84
Relative velocity (km/s)	8.128	1.741

Table 6.1: Results of optimization runs for the outbound trajectory to Hartley 2.

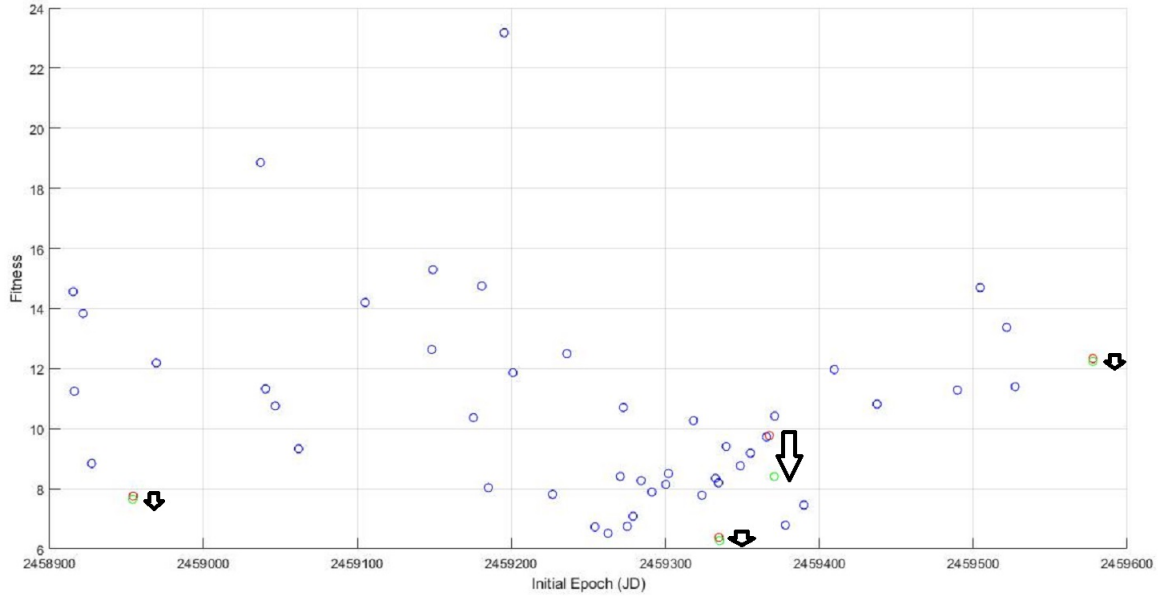


Figure 6.3: Fitness vs departure time plot showing the impact of grid search on four optimization runs.

(GS) method was utilized to search the solution space. Since a two-dimensional coplanar transfer was considered, performing a grid search based on departure time was observed to decrease the approach distance at the comet. This can be seen in Figure 6.3, where the fitness values found are plotted against their corresponding optimal departure dates. The figure shows the optimization results to be spread across a wide range (≈ 650 days) of departure dates with the majority falling in the region of the optimal point (2459334 JD). Even with this wide of departure times, the sailcraft is found to arrive at the comet within a span of 120 days (Sep-Dec 2023), which happens to be the period of the comet's perihelion passage and also the time of closest approach to Earth (Oct 2023). The departure times around the optimal point were searched using a progressively finer grid. The number of points in the grid was increased until the level of looking at departure dates every 10^{-5} days, i.e. in the order of 1 sec increments. The number of function evaluations becomes very large in this case. This is the reason for restricting the application of grid search to four optimization runs.

	Fitness	Δr (km)	Δv (km/s)	t_0 (JD)	TOF (days)
After DE	6.3823	112,537.3564	5.6686	2459334.5122	877.7700
GS (0.0004 days)	6.2792	1,013.3716	5.6774	2459334.9716	877.2486
GS (10^{-5} days)	6.2783	114.6370	5.6774	2459334.9716	877.2468

Table 6.2: Results of grid search obtained for the best optimization run from DE.

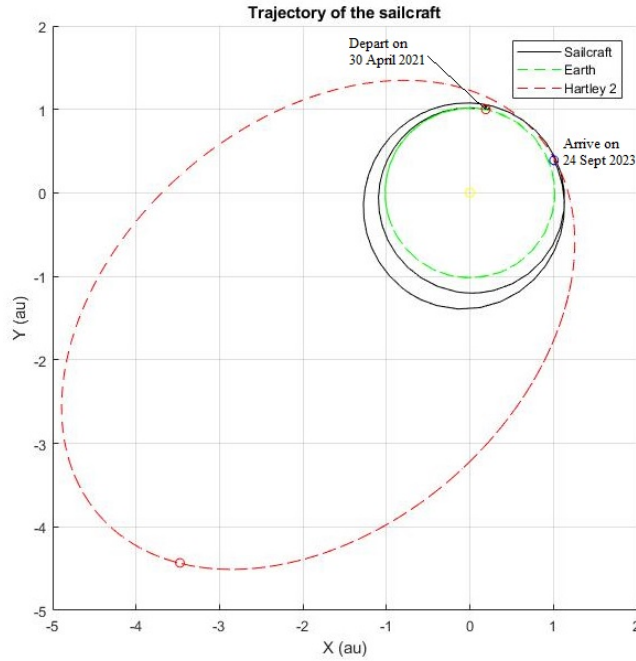


Figure 6.4: Representation of the optimal outbound trajectory.

Departure Date	30 April 2021
Time-of-Flight	877.2468 days
Arrival Date	24 Sept 2023
Approach Distance	114.637 km
Relative velocity	5.6774 km/s
Number of revolutions	≈ 2

Table 6.3: Attributes of the optimal outbound trajectory.

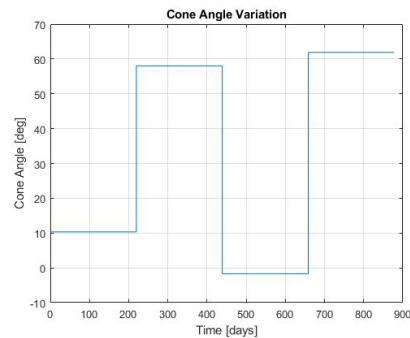


Figure 6.5: Cone Angle Profile for Outbound Trajectory.

As shown in Figure 6.3, the impact of grid search was not found to be uniform on all four of the arbitrarily chosen runs. For the case with the largest decrease in fitness, a reduction in approach distance from the order of a million km to less than a thousand km was observed. In other cases as well, a comparatively smaller decrease in approach distance was noted, but due to the normalization of distance, it is not so much reflected in the fitness value. This is seen in case of the optimization run with the lowest fitness value from Table 6.2. Furthermore a common aspect in all four GS cases is that GS does not affect the Δv , t_0 and TOF (as shown in Table 6.2), which is according to the expectation.

The trajectory of the optimal solution after the application of GS is presented in Figure 6.4 and various attributes of the trajectory are summarized in Table 6.3. The sailcraft following this trajectory would depart on April 30, 2021 and make a flyby at the comet Hartley 2 on September 24, 2023 after having flown for 877 days. The interesting attribute of this trajectory is that the sailcraft arrives at the comet exactly during its perihelion encounter with the Sun, and thus, will be able to witness

increased activity in the comet. Additionally, by flying close to the comet at a distance of 115 km, a larger quantity of dust and ice particles could be collected. The cone angle profile, shown in Figure 6.5, is oscillatory in nature, indicating an uniform solution for sail control function. Therefore, the optimal trajectory obtained for the outbound trajectory to Hartley 2 fulfills requirements of the mission.

6.2. SAMPLE RETURN TRAJECTORY TO 103P/HARTLEY 2

The majority of the settings that were implemented in the previous section were used for optimizing the solar sail sample return trajectory to comet Hartley 2. The only modifications were the increase in the number of decision variables by including an additional four angles for the return trajectory. These angles along with the departure time and overall time-of-flight form the 10 variables of the decision vector. A slight change was made in the objective function by normalizing the time-of-flight by one year (instead of four years) to bring all the terms of the objective function in the order of 1-10. The Earth return distance and velocity were also included in the objective function. The remainder of the conditions were maintained as such.

The sailcraft departing from the Earth heliocentric orbit is required to approach the comet at distances less than 250 km and collect samples from the comet's coma. The return trajectory should lead the sailcraft close to Earth's sphere of influence at a low relative velocity, in order to preserve the samples during re-entry. The aim of optimization is thus to find a trajectory which satisfies the above mission conditions. The DE algorithm is run in Tudat with a population size of 200 members. As mentioned in the previous sections, the initial populations are formed by randomly generated chromosomes. So, there is possibility for different optimization runs producing different optimal trajectories. Hence, 50 optimization runs were performed to determine the optimal trajectory and also evaluate the performance of DE.

The data from the results of the optimization runs is provided in Table 6.4. The histogram of the data is also shown in Figures 6.6a-6.8b. The fitness values found are not consistently on the lower range, unlike the outbound one-way trajectory optimization. The comet approach distances and sailcraft's relative velocities at the comet, have increased compared to what was observed for the one-way trajectory. Similarly, Earth return distance is also having a higher magnitude compared to the desired value close to Earth's SOI. Whereas the majority of the optimization runs resulted in an acceptable range for the Earth return velocity. The above results indicate that DE has not been as effective as for the outbound trajectory in finding near-optimal solutions. As mentioned in the previous section, this can be attributed to the increase (almost double) in the number of parameters in the decision vector. The corresponding increase in the real D-dimensional solution space might be the cause for the difficulty in finding the optimum. Moreover, the inclusion of Earth return distance and velocity terms in the objective function, does not simplify the problem. In fact, in most of the runs, contrasting results are observed for the terms evaluated at the comet and Earth. That is if one of them has low values, the other has high value terms.

In order to find better trajectory solutions, a grid search was applied using the results of DE as the base. But this time, the grid points cannot only be based on departure times. Searching around optimal departure times might reduce the comet approach distance as seen for the outbound trajectory. But this could in turn still result in a large Earth return distance. While performing grid search to reduce the fitness based on the eight angle variables is computationally inefficient. The alternative is to consider the overall TOF and departure time together and look for better solutions in this two-dimensional space. A grid search was performed based on these parameters on multiple

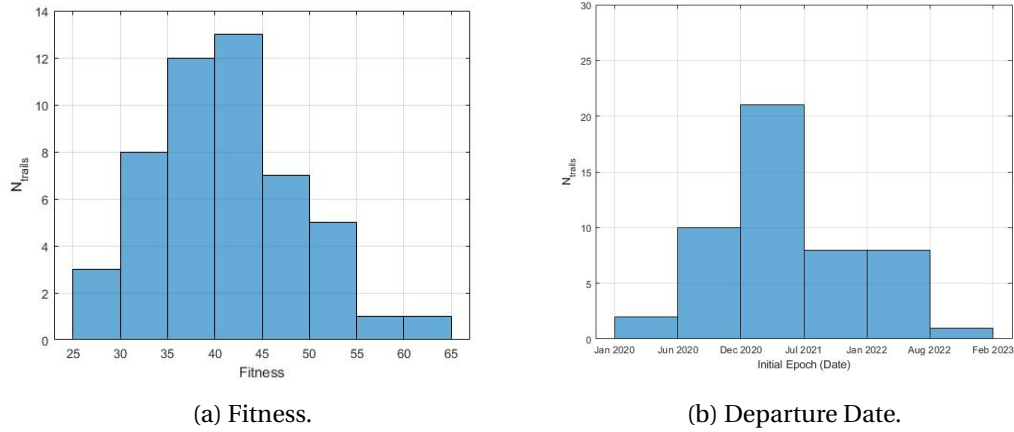


Figure 6.6: Histogram of fitness and departure date obtained for 50 runs to optimize the sample return trajectory to comet Hartley 2.

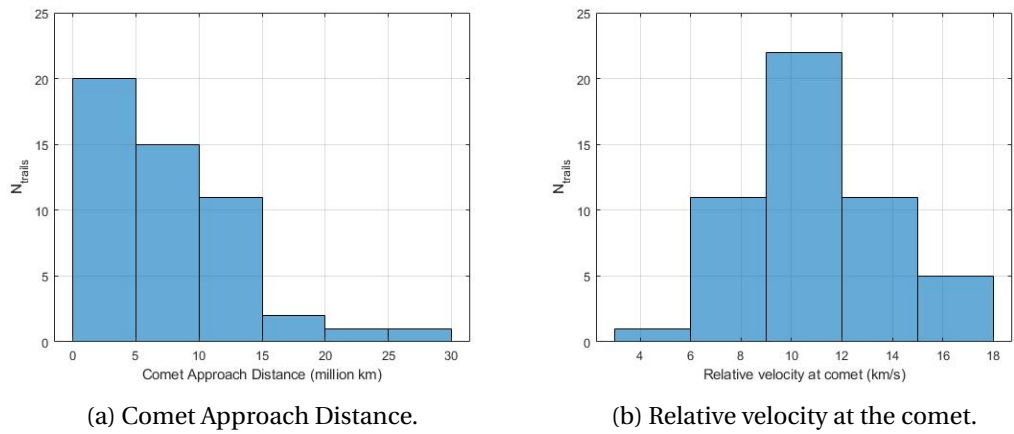


Figure 6.7: Histogram of comet approach distance and relative velocity obtained for 50 runs to optimize the sample return trajectory to comet Hartley 2.

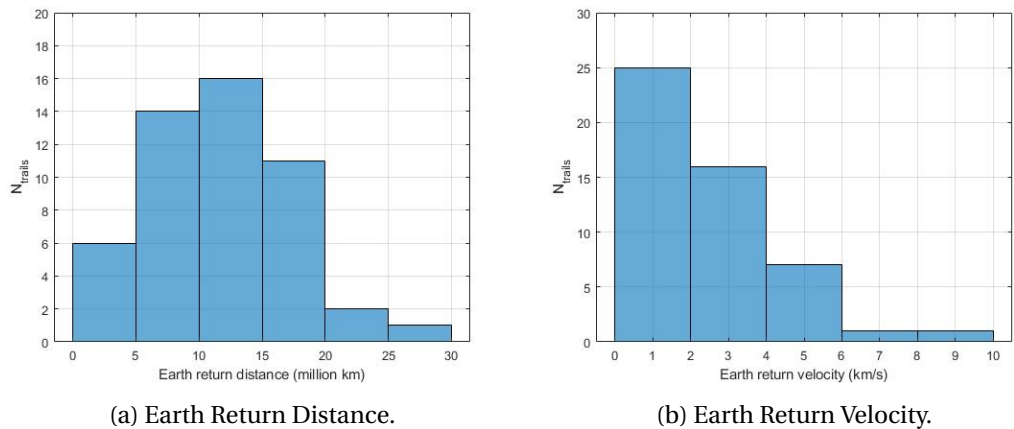


Figure 6.8: Histogram of Earth return distance and velocity obtained for 50 runs to optimize the sample return trajectory to comet Hartley 2.

	Average	Std. Deviation
Fitness	41.6201	7.6888
Departure time (JD)	2459351	231.535
TOF to Comet (days)	1448.39	842.17
Overall TOF (days)	3074.98	369.74
Δr_{Comet} (km)	8,028,609.13	5,352,236.91
Δr_{Earth} (km)	11,467,317.64	5,624,938.62
Δv at Comet (km/s)	11.125	2.767
Δv at Earth (km/s)	2.579	1.685

Table 6.4: Results of optimization runs for the sample return trajectory to Hartley 2.

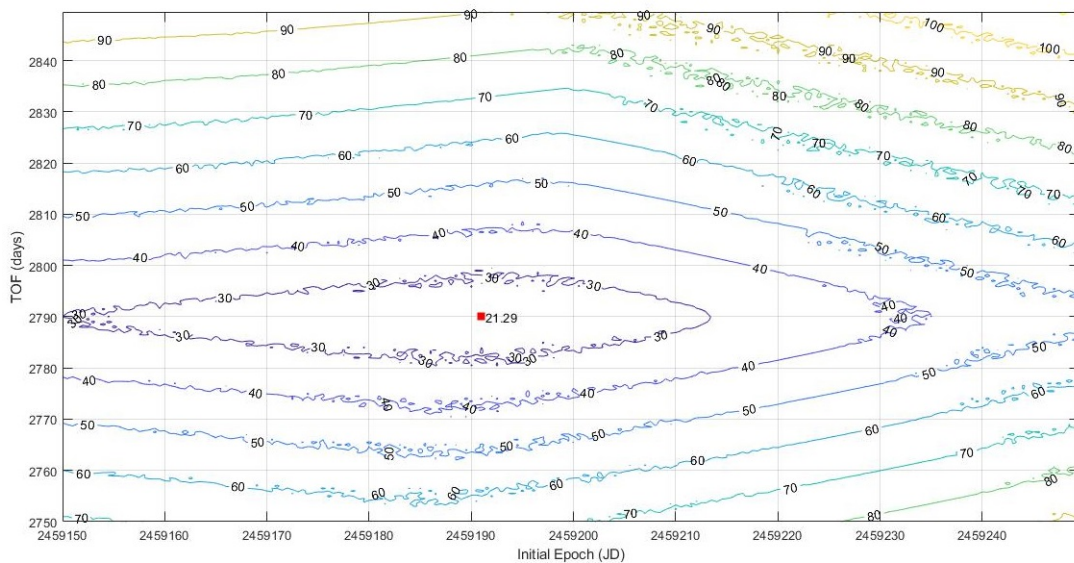


Figure 6.9: Contour plot of grid search results based on grid size of 1 day.

results obtained from DE. The contour plot for the initial grid search, with a grid size of 1 day, on one of these results is shown in Figure 6.9. When the contour plot is explored further by using a much finer grid close to the minima obtained, an interesting plot (Figure 6.10) is obtained.

Figure 6.10 shows the presence of numerous contour regions within the grid range considered. The yellowish regions have a slightly larger fitness values whereas the purple/violet regions depict the regions with low fitness. The regions with similar color codes tend to have similar fitness values as well. This implies the presence of many sub-optimal points which carry the same or similar fitness values. The reason as to the existence of such pocket regions in the contour plot has to do with the nature of the problem and the objective/fitness function used. The overall TOF determines the nodal points where the angle change occurs, thus influencing the dynamics of the sailcraft to a larger extent, as can be seen in Figure 6.9. Through Figure 6.10, the difference in fitness for neighboring regions can be noted. This could be due to the multiple term objective function, where every term is affected by the changes in departure date and/or overall TOF. This also causes the discontinuity in contour leading to the formation of small isolated regions. As opposed to the 2D grid search for the outbound trajectory, here the terms in objective function pertaining to the encounter with the comet are calculated at the point of minimum approach, which differs with both departure epoch as well as the overall TOF. This is in contrast to the one-way trajectory, where these terms were evaluated at the end of the TOF, while minimizing the TOF. Due to this reason, point of minimum

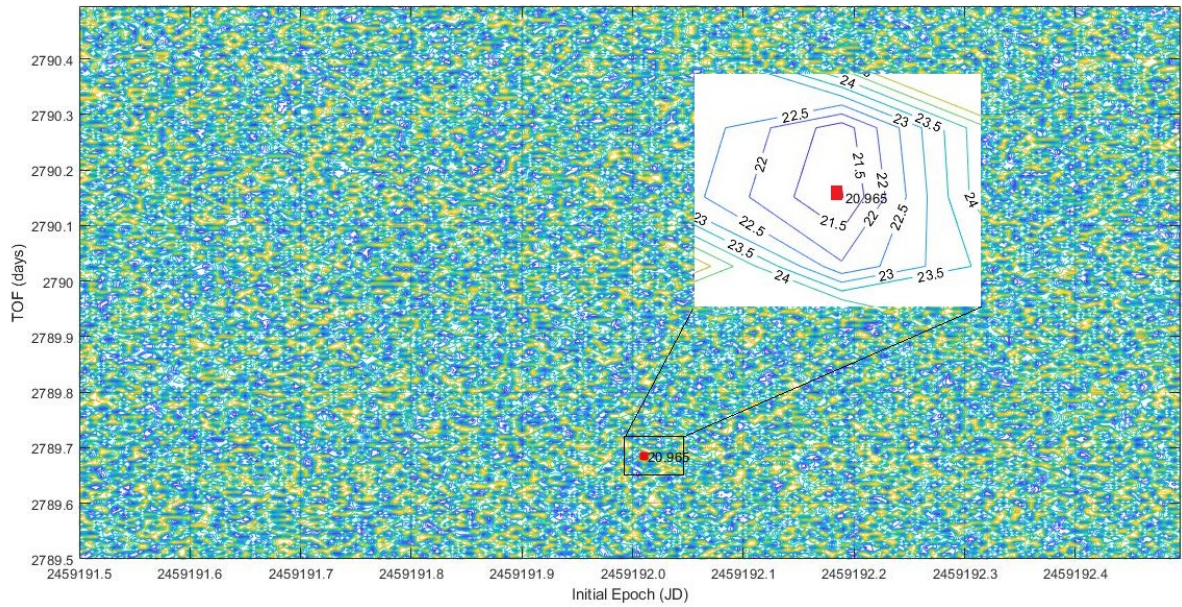


Figure 6.10: Contour plot of grid search results based on grid size of 0.01 day.

approach differs only with the TOF in case of the outbound trajectory analysis, thus producing continuous contour lines as shown in Appendix C.

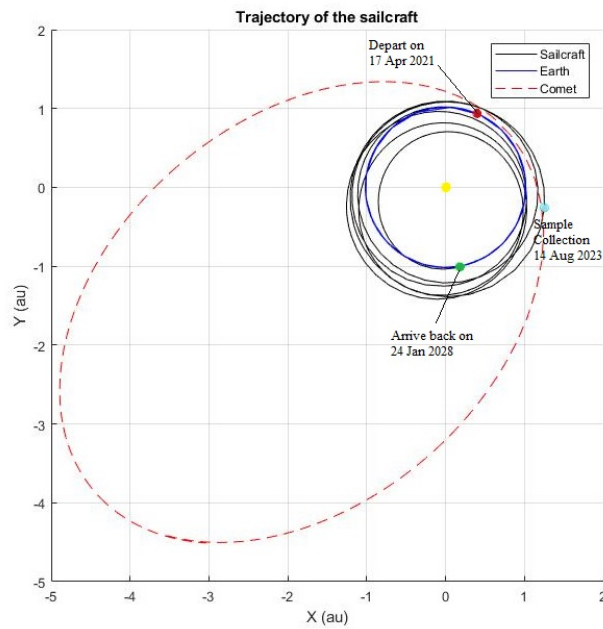


Figure 6.11: Representation of the optimal sample return trajectory.

The best trajectory obtained after GS is shown in Figure 6.11 and its attributes are listed in Table 6.5. Based on this trajectory, the sailcraft departs on April 17, 2021 which is two weeks earlier than the departure date found for the outbound trajectory in the previous section. The time of arrival at the

Departure Date	17 April 2021
TOF to comet	849.16 days
Arrival date at comet	14 Aug 2023
Comet Approach Distance	1019.598 km
Relative velocity at comet	8.426 km/s
Return date to Earth	24 Jan 2028
Earth return distance	821,958.213 km
Earth return relative velocity	4.942 km/s
Overall TOF	2473.3727 days
Number of revolutions	5

Table 6.5: Attributes of the optimal sample return trajectory.

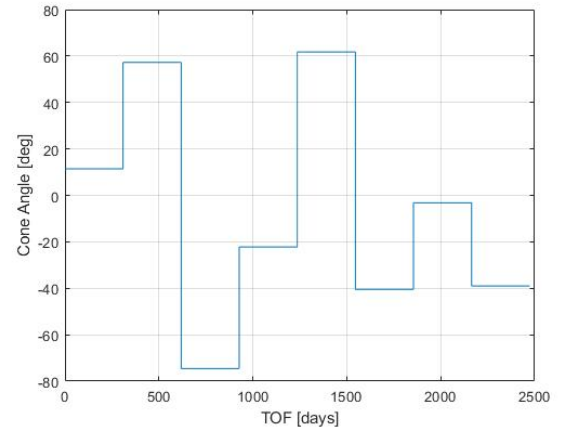


Figure 6.12: Cone angle profile for sample return trajectory.

comet and the time-of-flight to reach it were also similar to the results of the outbound trajectory. In fact, in this case, the sailcraft makes a flyby with the comet around a month earlier than the optimal outbound trajectory. The similarities between both the trajectories can be attributed to the identical initial angle variation from 10° to 58° , for the major portion (≈ 600 days) of the outbound trajectory to the comet. To counter the high velocity at the comet during sample collection, effective sample collection techniques (advanced than the collector in Stardust mission) could be employed to collect the particles at these speeds without damaging them. Also, in reality with the help of GNC (Guidance, Navigation and Control), the sailcraft can be maneuvered to approach the comet (after reaching its vicinity) at a closer distance and lower relative velocity. Furthermore, the return leg of the trajectory brings the sailcraft within the SOI of Earth and at a nominal relative velocity of 4.94 km/s. In view of the above results and considerations, the optimal solar sail trajectory was found to fulfill the distance and time-of-flight requirements of the sample return mission to comet 103P/Hartley 2. For the lightness number considered, various combinations of sailcraft mass and sail area can be used depending on the mass of the payload to be carried on board.

7

CONCLUSIONS AND RECOMMENDATIONS

7.1. CONCLUSIONS

The current thesis work focused on the optimization of solar sailcraft trajectory for a comet sample return mission. The study began by formulating the requirements for the sample return mission based on the knowledge from literature and past missions. From a list of potential target options, comet 103P/Hartley 2 was selected as the target for the mission based on various criteria.

The theoretical foundations for the mission were set by making choices on the dynamics model and solar sail design. The equations of motion were decided to be written in the Gauss form of Planetary Equations using modified equinoctial elements. The variable step-size integrator, DOPRI8(7) was used for the propagation of the trajectory in time. Differential Evolution was employed as the optimization algorithm and the simulations were carried out in the Tudat toolbox, with the PAGMO modules providing the algorithms for performing the optimization.

The solar sailing acceleration model developed and implemented in Tudat for this thesis, was tested and verified prior to running simulations. The sail orientation represented by the sail cone and clock angles were considered to change at discrete nodal points. With the help of a solar sail reference trajectory to Mars, the performance of the integrator was validated. Similarly, a Venus rendezvous trajectory was recreated in order to tune and validate the settings of the DE optimizer. The objective function considered for optimization was a weighted sum of multiple constraints on sailcraft's position, velocity and orbital elements, that need to be fulfilled by the trajectory. The results obtained for the validation case proved the algorithm to be capable of handling coplanar rendezvous transfers.

The optimization of the comet sample return mission was performed in two parts - (i) an outbound trajectory to the comet and (ii) the overall sample return trajectory to the comet. The simulations were performed for a sailcraft with a lightness number of 0.05. The decision vector consisted of the departure time, time-of-flight and the cone angles needed for steering the sailcraft. Due to the highly eccentric nature of the comet orbit and the use of a nominal performance sail, the orbital elements of sailcraft and the comet could not be matched using the given settings. Modifications were done to the objective function to just include the position and velocity constraints. The results obtained following this, were found to be sub-optimal in terms of the large approach distances to the comet. Hence, a grid search on the departure date was employed to reduce the approach distance and narrow in on the optimum solution. The optimal outbound trajectory found was able to

make the sailcraft reach the comet in 877 days and date of arrival matched with the comet's perihelion passage.

In the second part, the return leg of the mission was also included, thereby increasing the number of decision variables from 6 to 10. Furthermore, the objective function now included terms for the return conditions at Earth as well. With the same settings as for the outbound trajectory, 50 optimization runs were performed. The outcome of these runs produced results which were not optimal by far. The grid search method was again utilized for improving the results. Searching through the two-dimensional grid formed by departure time and time-of-flight, numerous sub-optimal points were found, with many of them not satisfying the mission requirements. The best result among those sub-optimal points was found to fulfill the time and distance requirements of the mission. The high relative velocity during sample collection can be countered by using a more advanced sample collection technique or with the help of GNC the sailcraft can be maneuvered towards the comet for collecting the particles.

Based on the optimization results obtained in both the cases, it can be seen that DE by itself was not sufficient to find the optimal trajectory. The performance of DE was influenced by the number of decision variables and by the presence of multiple constraint terms in the objective function. This is evident from the sample return trajectory analysis, where DE could not replicate the performance in determining the optimal trajectory as in the case of the outbound trajectory. The reduction in DE performance can be attributed to the increase in number of decision variables to be determined and additional penalty terms in the objective function. However, considering the nature of the comet's orbit, the fact that the sailcraft following the optimal trajectory will be able to reach the comet at a close distance, collect the particles and return back to Earth within 6.77 years, shows the success of the solution obtained in fulfilling the mission requirements. Therefore, the research has been able to successfully answer the question raised at the start of the thesis work, by demonstrating the effectiveness of using solar sailing for comet sample return mission.

7.2. RECOMMENDATIONS

Since this was a preliminary mission study, various straightforward assumptions were considered. But, for future research on this topic, it would be more effective if an optimizer capable of handling multiple objectives were to be used. Alternatively, using a Pareto-optimal approach can reduce the uncertainty surrounding the weight factors in the objective function and could aid in solving the problem as a single-objective optimization. As seen in this thesis, the problem is plagued by the presence of numerous sub-optima. Though grid search method scans the solution space, these results are based on only the time parameters, as performing grid search based on the angles would be computationally inefficient. So, an effective local optimization technique which can search without getting stuck in these optima, might be important to perform post-optimization search.

Furthermore, the disadvantage of using discrete piecewise control is that the dynamics of the sail are restricted. So, for more advanced studies, the angles can either be interpolated between the nodes or continuous angle representation can be adopted. In such cases, to reduce the dimensionality of the problem, steering strategies can be employed. For example, taking the case of a trajectory to a comet, a local steering law based on maximizing the eccentricity and inclination (or semi-major axis) can be used.

As more direct recommendations, the thesis work can be extended to three dimensions and a more

realistic sail force model (like optical sail force model) can be incorporated. The gravitational attraction from other bodies could also be included as perturbations. As an extension of the previous recommendation, it will be interesting to see the results when including solar photonic assists or gravitational assists in the problem. Finally, since the choice of the sail lightness number seems to affect the trajectory followed by the sailcraft, performing a sensitivity analysis on the results for various sail lightness numbers could provide more insight about the sail performance needed to execute these missions.

A

OPTIMIZATION OF THREE-DIMENSIONAL SOLAR SAILCRAFT TRAJECTORY

In Section 6.1, the reason for considering a two-dimensional transfer is briefly explained. Here, the results of preliminary optimization results for a three-dimensional transfer to the comet Hartley 2 is given. The optimal trajectory obtained from DE is shown in Figure A.1.

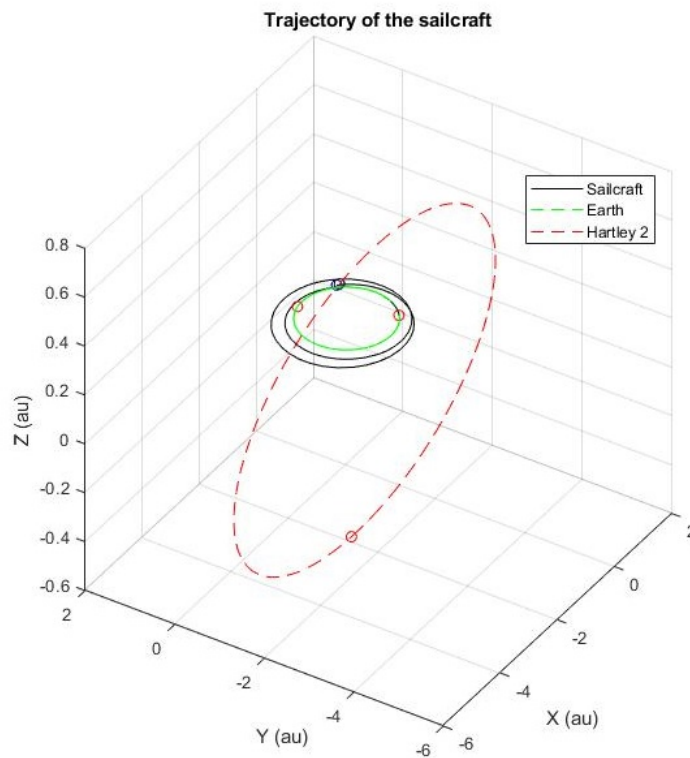


Figure A.1: Optimal three-dimensional outbound trajectory to Comet Hartley 2.

The values of important aspects of the trajectory are provided in Table A.1 and the projection of the optimal trajectory in 2D plane is shown in Figure A.2.

The large values of approach distance and relative velocity indicates the difficulty faced by the DE algorithm in minimizing these parameters. This is because in the 3D trajectory analysis, the number

Departure Date	30 July 2020
TOF to comet	1,168.6 days
Comet Approach Distance	2,041,689.189 km
Relative velocity at comet	10.03 km/s
Δa	300,433,833 km
Δe	0.50

Table A.1: Results of three-dimensional trajectory optimization.

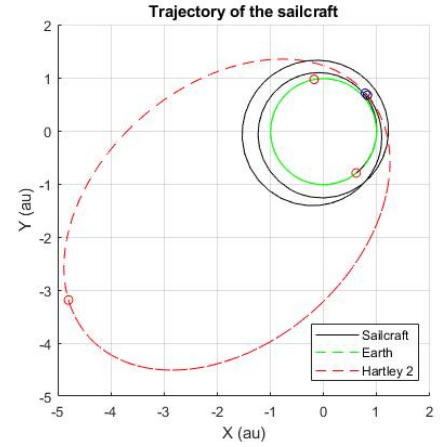


Figure A.2: Projection of the optimal trajectory.

of decision variables increase from 6 to 10. So, DE has to search through a ten-dimensional parameter space to find the optimal trajectory. The task is further complicated by the complex nature of the comet's orbit. As a result, the minimum approach distance and the velocity difference are way off from the desired values.

Considering a third-dimensional trajectory analysis for the entire sample return mission would still increase the dimension of the parameter space to 18, which would be extremely difficult to solve and will cause the optimizer to result in solutions far from the optimum. Due to these reasons, a two-dimensional trajectory analysis was adopted in this thesis. Additionally, from Figure A.1, it can be seen that the optimal trajectory almost remains in the ecliptic plane and intersects the comet when the comet passes through its descending node. This planar nature of the optimal trajectory adds to the justification of considering a two-dimensional trajectory analysis.

B

TRAJECTORY TO 103P/HARTLEY 2 USING A HIGH PERFORMANCE SAIL

As discussed in Section 6.1, for the lightness number $\beta = 0.05$, the trajectory found by the optimizer could not fulfill the conditions set on the sailcraft velocity and orbital elements. This resulted in a flyby trajectory to the comet than the desired rendezvous trajectory. In order to verify if the reason for the above result is due to the slow evolving nature of the sailcraft when $\beta = 0.05$, the trajectory analysis was performed for a higher lightness number β of 0.3. As per the classification of sail performance in [60], $\beta = 0.3$ falls under the category of high performance sails. Such sails have very low sail loading value and thus, do not exist in reality as of now. For comparison, the lightness number of the largest sail (Sunjammer mission) made until now is 0.07.

The optimal trajectory obtained from the DE optimizer is shown below in Figure B.1. The details of the trajectory are mentioned in Table B.1.

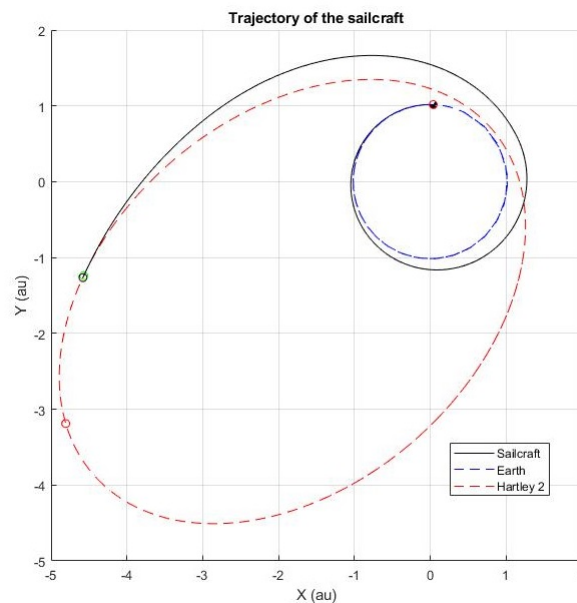


Figure B.1: Rendezvous Trajectory to Comet Hartley 2 using a high performance sail

Departure time	t_0	May 19, 2022
Time-of-flight	TOF	1,095.7 days
Approach distance	Δr	5,745.535 km
Relative velocity	Δv	0.197 km/s
Difference in Semi-major axis	Δa	749.158 km
Difference in Eccentricity	Δe	0.0034

Table B.1: Results of the optimal trajectory for a high performance sailcraft.

From the figure, it can be observed that the trajectory of the sailcraft spirals outwards rapidly than what was observed for the moderate performance sails. The sailcraft is able to rendezvous with the comet after just 1096 days. Apart from the match in position and velocity, the high performance sail is able to replicate the orbital elements to a reasonable extent. This means that the sailcraft can follow the comet in its orbit and obtain samples during the different active phases of the comet. Thus, this analysis confirms that for a higher value of lightness number, i.e. using a high performance sail, the objective to rendezvous the comet is satisfied along with all the position, velocity and orbital element constraints. Having said that, the results of this analysis are currently not possible with the existing solar sail technology and hence, the moderate performance sails ($\beta = 0.05$) were used for analysis done in this thesis.

C

TWO-DIMENSIONAL GRID SEARCH RESULTS FOR THE OUTBOUND TRAJECTORY

The contour of the two-dimensional grid search for the outbound trajectory remains continuous even when finer grid was used as shown in the figures below.

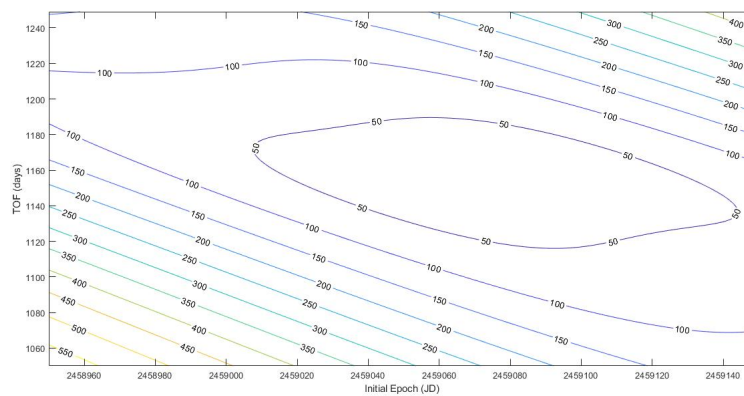


Figure C.1: Grid Search on Outbound Trajectory with grid size of 10 days.

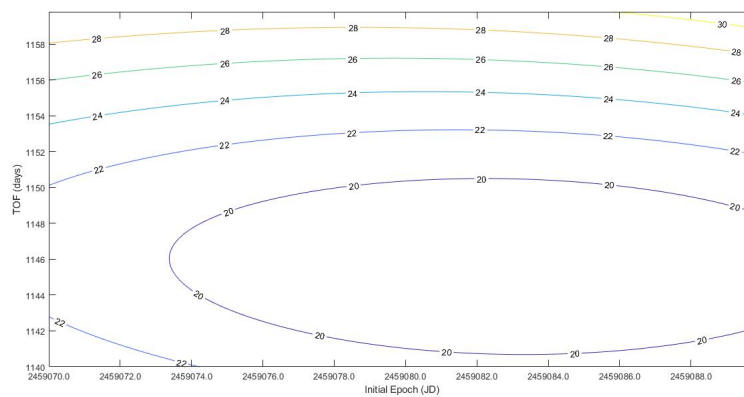


Figure C.2: Grid Search on Outbound Trajectory with grid size of 0.2 day.

BIBLIOGRAPHY

- [1] M. Küppers, H. Keller, and E. Kührt et. al., *Triple F — a comet nucleus sample return mission*, *Experimental Astronomy*, Volume 23, Issue 3, pp 809-847 (2009).
- [2] M. Burchell, M. Prince, and P. Wozniakiewicz et. al., *Sample return missions to minor bodies*, *Astronomy and Geophysics*, Volume 54, Issue 3, pp 3.28–3.32 (2013).
- [3] D. S. Lauretta, S. W. Squyres, and S. Messenger et. al., *The caesar new frontiers mission: Sample science*, 49th Lunar and Planetary Science Conference, The Woodlands, Texas (2018).
- [4] C. R. Neal, C. K. Shearer, M. Wadwha, L. Borg, B. Jolliff, and A. Treiman, *Developing sample return technology using the earth's moon as a testing ground*, The Inner Planets Panel, NRC Decadal Survey for the Planetary Sciences Division, Science Mission Directorate, NASA (2008).
- [5] S. W. Squyres, K. Nakamura-Messenger, and F. Mitchell et. al., *The caesar new frontiers mission: Overview*, 49th Lunar and Planetary Science Conference, The Woodlands, Texas (2018).
- [6] European Space Agency, *Rosetta mission*, http://www.esa.int/Our_Activities/Space_Science/Rosetta, [Online; accessed November 5, 2018].
- [7] C. R. McInnes, *Solar Sailing: Technology, Dynamics and Mission Applications* (Praxis Publishing Limited, Chichester, UK, 1999).
- [8] L. Herbeck, C. Sickinger, M. Eiden, and M. Leipold, *Solar sail hardware developments*, European Conference on Spacecraft Structures, Materials and Mechanical Testing, Toulouse (2002), pg. 1-10.
- [9] M. MacDonald, *Solar sailing: Applications and technology advancement*, *Advances in Spacecraft Technologies* (2011), pg. 35-60.
- [10] L. Friedman, *The rise and fall of Cosmos 1*, <http://www.planetary.org/explore/projects/lightsail-solar-sailing/story-of-lightsail-part-2.html>, [Date of Access: October 9, 2018].
- [11] M. Macdonald, *Advances in Solar Sailing* (Springer-Verlag Berlin Heidelberg, 2014).
- [12] Y. Tsuda et al., *Achievement of IKAROS — Japanese deep space solar sail demonstration mission*, *Acta Astronautica*, Volume 82, Issue 2 (2012).
- [13] eoPortal Directory, *NanoSail-D2*, <https://directory.eoportal.org/web/eoportal/satellite-missions/n/nanosail-d2> (), [Date of Access: October 9, 2018].
- [14] J. P. Eastwood, D. O. Kataria, C. R. McInnes, N. C. Barnes, and P. Mulligan, *Sunjammer*, *Weather*, Vol. 70, Issue 1, Royal Meteorological Society (2015).
- [15] eoPortal Directory, *LightSail Missions of The Planetary Society*, <https://directory.eoportal.org/web/eoportal/satellite-missions/l/lightsail> (), [Date of Access: October 9, 2018].

- [16] U. Geppert, B. Biering, F. Lura, J. Block, M. Straubel, and R. Reinhard, *The 3-step DLR-ESA gossamer road to solar sailing*, Advances in Space Research, Vol. 48, Issue 11 (2011).
- [17] L. McNutt, L. Johnson, D. Clardy, J. Castillo-Rogez, A. Frick, and L. Jones, *Near-Earth Asteroid Scout*, AIAA SPACE Conference and Exposition, San Diego (2014).
- [18] T. Okada et al., *Science and Exploration in the Solar Power Sail OKEANOS Mission to a Jupiter Trojan Asteroid*, 49th Lunar and Planetary Science Conference, Texas (2018).
- [19] J. C. Brandt, *Physics and Chemistry of Comets* (Encyclopedia of the Solar System, Chapter 30, pp 557-574, 2006).
- [20] I. De Pater and J. J. Lissauer, *Planetary Sciences* (Cambridge University Press, 2001).
- [21] S. A. Sandford et al., *The comet coma rendezvous sample return mission concept - the next step beyond stardust*, NASA Ames Research Center (2010).
- [22] F. M. McCubbin et al., *Priority science targets for future sample return missions within the solar system out to the year 2050*, Planetary Science Vision 2050 Workshop, Washington DC, United States (2017), JSC-CN-38641.
- [23] M. Henderson and W. Blume, *Deep impact – a review of the world's pioneering hypervelocity impact mission*, Procedia Engineering, Elsevier (2015).
- [24] M. F. A'Hearn, *Deep impact and the origin and evolution of cometary nuclei*, Space Science Review, Springer (2008).
- [25] T. W. S. Journal, *How probes get 'gravity assists' in their journeys through space*, http://si.wsj.net/public/resources/images/W0-AT286_ROSETT_G_20140806124805.jpg, [Online; accessed October 25, 2018].
- [26] eo Portal Directory, *Rosetta rendezvous mission with comet 67p/churyumov-gerasimenko*, <https://directory.eoportal.org/web/eoportal/satellite-missions/r/rosetta>, [Online; accessed October 20, 2018].
- [27] NASA, *Stardust Launch*, Press Kit (1999).
- [28] P. D. Feldman and M. F. A'Hearn et al., *Measurements of the near-nucleus coma of Comet 67P/Churyumov-Gerasimenko with the Alice far-ultraviolet spectrograph on Rosetta*, Planets and planetary systems, Astronomy and Astrophysics (2015).
- [29] D. E. Brownlee et al., *Stardust: Comet and interstellar dust sample return mission*, Journal of Geophysical Research, Vol. 108, Issue E10, AGU Publications (2003).
- [30] D. Brownlee, *The Stardust Mission: Analyzing Samples from the Edge of the Solar System*, Annual Review of Earth and Planetary Sciences, Vol. 42:179-205 (2014).
- [31] E. L. Berger, T. J. Zega, L. P. Keller, and D. Lauretta, *Evidence for aqueous activity on comet 81P/Wild 2 from sulfide mineral assemblages in Stardust samples and CI chondrites*, Geochimica et Cosmochimica Acta, Vol. 75, Issue 12, Elsevier (2011).
- [32] H. Weaver, M. A'Hearn, G. Fountain, J. Leary, and C. Niebur, *Comet surface sample return - mission study objectives*, <http://www.lpi.usra.edu/opag/meetings/nov2007/presentations/cssr.pdf>, [Online; accessed September 25, 2018].

- [33] B. Dachwald, W. Seboldt, and L. Richter, *Multiple Rendezvous and Sample Return Missions to Near-Earth Objects using Solar Sailcraft*, 5th IAA Conference on Low-Cost Planetary Missions, Noordwijk, The Netherlands (2003).
- [34] JPL, *JPL small-body database search engine*, https://ssd.jpl.nasa.gov/sbdb_query.cgi, [Online; accessed September 25, 2017].
- [35] NASA, *Comet - Science Targets*, <https://solarsystem.nasa.gov/planets/comets/sats>, [Online; accessed September 25, 2017].
- [36] K. F. Wakker, *Fundamentals of Astrodynamics* (Institutional Repository, Delft University of Technology, 2015).
- [37] B. N. Suresh and K. Sivan, *Integrated Design for Space Transportation System* (Springer India, 2015).
- [38] NAIF, *An overview of reference frames and coordinate systems in the spice context*, https://naif.jpl.nasa.gov/pub/naif/toolkit_docs/Tutorials/pdf/individual_docs/17_frames_and_coordinate_systems.pdf, [Online; accessed October 14, 2018].
- [39] L. Carzana., *Laser-Enhanced Solar Sailing: Modeling and Trajectory Optimization for Interplanetary Missions*, Master Thesis Report, TU Delft (2017).
- [40] B. Dachwald, *Low thrust trajectory optimization and interplanetary mission analysis using evolutionary neurocontrol*, Ph.D. Dissertation, Bundeswehr University Munich (2003).
- [41] L. Chen, X. Z. Bai, Y. G. Liang, and K. B. Li, *Orbital Prediction Error Propagation of Space Objects*, Orbital Data Applications for Space Objects, Springer (2017).
- [42] M. J. H. Walker, B. Ireland, and J. Owens, *A set of modified equinoctial orbit elements*, Celestial Mechanics, vol. 36, p. 409-419 (1985).
- [43] J. H. Jo, I. K. Park, N. Choe, and M. Choi, *The Comparison of the Classical Keplerian Orbit Elements, Non-Singular Orbital Elements (Equinoctial Elements), and the Cartesian State Variables in Lagrange Planetary Equations with J2 Perturbation: Part I*, Journal of Astronomy and Space Sciences, Volume 28, Issue 1, The Korean Space Science Society (2011).
- [44] B. Dachwald, *Optimal Solar-Sail Trajectories for Missions to the Outer Solar System*, Journal of Guidance, Control and Dynamics, Vol. 28 (2005).
- [45] G. Mengali and A. A. Quarta, *Optimal Three-Dimensional Interplanetary Rendezvous Using Nonideal Solar Sail*, Journal of Guidance, Control and Dynamics, Vol. 28 (2005).
- [46] R. D. Falck and J. W. Dankanich, *Optimization of low-thrust spiral trajectories by collocation*, 2012 Astrodynamics Specialists Conference, AAS, Minneapolis (2012).
- [47] O. Montenbruck and E. Gill, *Satellite Orbits: Models, Methods and Applications* (Springer-Verlag Berlin Heidelberg, 2000).
- [48] K. Price, R. M. Storn, and J. A. Lampinen, *Differential Evolution - A Practical Approach to Global Optimization* (Natural Computing Series, Springer, 2005).
- [49] A. Ohndorf, *Multiphase Low-Thrust Trajectory Optimization Using Evolutionary Neurocontrol*, Doctoral Thesis, Delft University of Technology (2016).

- [50] P. Di Lizia and G. Radice, *Advanced global optimization tools for mission analysis and design*, Final Report of ESA, Ariadna Id: 03/4101 (2004).
- [51] C. J. Spaans and E. Mooij, *Performance evaluation of global trajectory optimization methods for a solar polar sail mission*, AIAA Guidance, Navigation, and Control Conference, Chicago, Illinois (2009).
- [52] E. Github, *Pagmo and pygmo*, <https://esa.github.io/pagmo2/index.html>, [Online; accessed October 15, 2018].
- [53] E. Hekma, *Debris removal with zoomed grid search optimization*, Master Thesis Report, Delft University of Technology (2017).
- [54] F. J. Ahlers et al., *Differential evolution for continuous function optimization*, <http://www1.icsi.berkeley.edu/~storn/code.html>, [Online; accessed October 15, 2018].
- [55] S. Das and P. N. Suganthan, *Differential evolution: A survey of the state-of-the-art*, IEEE Transactions on Evolutionary Computation, Vol. 15, No. 1 (2011).
- [56] L. Petrović, *Motion planning in high-dimensional spaces*, (2018), arXiv:1806.07457 [cs.RO] .
- [57] B. Dachwald, *Radiation Pressure Force Model for an Ideal Laser-Enhanced Solar Sail*, The Fourth International Symposium on Solar Sailing, Kyoto, Japan (2017).
- [58] M. Zhang, G. Wang, and Y. Sun, *Solar sail trajectory optimization for earth-mars mission*, Proceedings of the 29th Chinese Control Conference, Beijing, China (2010).
- [59] G. W. Hughes, *A realistic, parametric compilation of optimised heliocentric solar sail trajectories*, Ph.D. thesis, University of Glasgow (June 2005).
- [60] B. Dachwald, *Optimization of Interplanetary Solar Sailcraft Trajectories Using Evolutionary Neurocontrol*, Journal of Guidance, Control and Dynamics, Vol. 27 (2004).